

TERAHERTZ SCIENCE AND TECHNOLOGY  
OF LOW-DIMENSIONAL MATERIALS:  
DYNAMICS, CONDUCTIVITY, AND  
PLASMONICS

A Dissertation  
Presented to the Faculty of the Graduate School  
of Cornell University  
in Partial Fulfillment of the Requirements for the Degree of  
Doctor of Philosophy

by  
Jared Hillel Strait  
May 2015

©2015 Jared Hillel Strait

TERAHERTZ SCIENCE AND TECHNOLOGY OF LOW-DIMENSIONAL  
MATERIALS: DYNAMICS, CONDUCTIVITY, AND PLASMONICS

Jared Hillel Strait, Ph. D.

Cornell University 2015

Materials that confine electrons and holes in low dimensions and microstructures have unusual electronic, mechanical, and optical properties. These materials represent an exciting avenue toward high-performance terahertz-frequency devices. This dissertation describes several experiments which probe the conductivity and charge-carrier dynamics of these technologically important material systems, including a focus on plasmonic effects. Using time-domain terahertz spectroscopy, we have determined the time scales and manner of carrier recombination and cooling in graphene, molybdenum disulfide, and germanium nanowires. Using frequency-domain terahertz spectroscopy, we have investigated the AC conductivity of these materials, including the intrinsic mobility of molybdenum disulfide and the plasmonic properties of graphene and germanium nanowires. Finally, we present measurements of terahertz emission from silicon carbide and evaluate the potential of this material as a platform for terahertz optoelectronics. Together, these measurements represent an advance in nanotechnology through terahertz science and an advance in terahertz technology through nanoscience.

## Biographical Sketch

Jared H. Strait grew up in the western Massachusetts town of Williamstown, enjoying the rural environment before eventually attending Williams College. There he studied Physics while running with the cross-country and track teams and instructing skiing with the outing club. In his senior year, Jared developed a method of frequency-locking diode lasers for an atomic spectroscopy experiment in the lab of Professor Protik Majumder, which led him to the graduate program at Cornell University. Upon arriving in Ithaca, Jared joined the group of Farhan Rana and settled in, studying solid-state physics, nanoscience, and optics, occasionally skiing and running, and eventually meeting and marrying his awesome wife, Jennie.

To Jennie.

## Acknowledgments

Thanks to my friends and colleagues Paul, Haining, and Pari. My best learning at Cornell came when with you. Professor Rana, for all of the time, effort, advice, collaboration, and friendship you have given to me, I am forever grateful.

# Contents

<b>1</b>	<b>Introduction</b>	<b>1</b>
<b>2</b>	<b>Terahertz Spectroscopy</b>	<b>5</b>
2.1	The Terahertz Frequency Range . . . . .	5
2.2	FTIR Spectroscopy . . . . .	6
2.3	Time-Domain Terahertz Spectroscopy . . . . .	8
2.3.1	Emission of Broadband THz Pulses . . . . .	9
2.3.2	Electro-optic Sampling and Experimental Setup . . . . .	11
2.4	Optical Parameter Extraction from Transmission Measurements . . . . .	16
2.4.1	Two-Dimensional Sheet Conductivity . . . . .	16
2.4.2	Complex Refractive Index of a Material with Finite Thickness . . . . .	18
2.5	Optical-Pump Terahertz-Probe Spectroscopy . . . . .	19
2.5.1	Experimental Setup . . . . .	21
2.5.2	Conductivity Extraction and Time-Shift . . . . .	25
2.5.3	Optical-Pump THz-Probe Temporal Resolution . . . . .	30
<b>3</b>	<b>Mobility of Multilayer Molybdenum Disulfide</b>	<b>32</b>
3.1	Experiment and Results . . . . .	34
3.1.1	Conductivity Spectra and Momentum Scattering Times . . . . .	35
3.1.2	Carrier Mobility and Deformation Potential . . . . .	38
3.2	The Ultimate Limit of Mobility in Molybdenum Disulfide . . . . .	40
<b>4</b>	<b>Carrier Relaxation in Semiconductors</b>	<b>42</b>
4.1	Carrier Relaxation in Multilayer Molybdenum Disulfide . . . . .	42
4.1.1	Carrier Dynamics on Short Time Scales . . . . .	43
4.1.2	Carrier Dynamics on Long Time Scales . . . . .	45
4.1.3	MoS <sub>2</sub> Recombination Model . . . . .	47
4.1.4	Discussion . . . . .	51
4.2	Carrier Relaxation in Germanium Nanowires . . . . .	53
4.2.1	Experiment . . . . .	54
4.2.2	Discussion . . . . .	56
4.3	Carrier Cooling in Graphene . . . . .	61
4.3.1	Experiment . . . . .	63
4.3.2	Model of Carrier Cooling in Graphene . . . . .	67

4.3.3	Comparison of the Model to Data . . . . .	76
4.3.4	Outlook . . . . .	76
<b>5</b>	<b>Semiconductor Plasmonics</b>	<b>79</b>
5.1	The Terahertz Response of Oriented Germanium Nanowires . . . . .	80
5.1.1	Ge Nanowire Polarization Experiment . . . . .	81
5.2	Confined Plasmons in Graphene Microstructures . . . . .	88
5.2.1	Far-IR Spectroscopy of Graphene Plasmonic Strips . . . . .	89
5.2.2	Basic Plasmon Model . . . . .	91
5.2.3	Analytic Electrodynamics Model . . . . .	92
5.2.4	Graphene Plasmon Interactions . . . . .	95
5.2.5	Finite-Difference Time-Domain Simulation . . . . .	98
5.2.6	Outlook . . . . .	101
<b>6</b>	<b>Terahertz Emission from Silicon Carbide</b>	<b>103</b>
6.1	Introduction . . . . .	103
6.2	Experiment and Results . . . . .	104
6.2.1	Determination of Emission Mechanism . . . . .	105
6.2.2	The Ratio of Nonlinear Susceptibility Components . . . . .	110
6.2.3	Refractive Index and Phase Matching . . . . .	110
6.3	Phase Matching for Efficient THz Generation . . . . .	112

# Chapter 1

## Introduction

The maturity of optical and electronic technology has necessitated the search for further improvement through novel materials and novel device physics. The semiconductor industry has spent billions of dollars developing silicon technology for metal-oxide-semiconductor field-effect transistors, which have been wildly successful. Thirty-two nanometer nMOS technology based on strained silicon and high-k gate dielectrics producing (capacitance de-embedded) cut-off frequencies of  $f_T = 445$  GHz [1] is now old news. The optics industry offers tunable, continuous wave and pulsed laser sources in colors throughout the visible, near-infrared, and mid-infrared wavelength ranges, as well as a complete array of passive and active devices (filters, lenses, polarizers, waveplates, modulators, detectors, etc.) to accompany them. Also available are commercial sources, detectors, interconnects, and multiplexing systems for extremely long-distance and high-bandwidth optical communications. For instance, in 2012 the companies NEC and Corning announced multicore optical fibers allowing data transmission faster than one petabit ( $10^{15}$ ) per second [2]. Further development of these mature technologies is a slow, expensive, and incremental process.

But despite the incredible capabilities of current technology, there is room for improvement. Smaller, faster, and lower-power devices and communications are al-

ways desirable in an increasingly connected and mobile society with large-scale data requirements [3]. In addition, there are regions of the electromagnetic spectrum that remain unconquered by commercial optical and electronics technology. One such region is the extreme ultraviolet frequency range, for which there is an effort in developing sources for 13 nm wavelength photolithography systems [4]. Another relatively unexploited region of the electromagnetic spectrum is the terahertz (THz,  $10^{12}$  sec<sup>-1</sup>) frequency range [5, 6], which is important for spectroscopy, imaging, ultra high-speed electronics, and even satellite communications [7]. But terahertz technology lags terahertz applications. The work presented in this dissertation focuses on improving terahertz technology as well as applying current terahertz technology to questions in materials science and device physics. But our motivation is not to advance electronic and optical devices in the form of incremental improvements to commercial technology. Rather, we seek advancements through the combination of novel materials, novel device physics, and novel applications. We look for materials with unusual properties that do not merely extend the capabilities of existing technology, which is formidable, but rather provide paths to completely new technology, with applications perhaps not yet imagined.

One class of materials that has received much interest in the scientific community is that of low-dimensional materials. Metals, semiconductors, and insulators that are effectively two-dimensional, one-dimensional, and zero-dimensional have unusual electronic, optical, chemical, and mechanical properties [8]. For instance, the density of electronic states in low-dimensional materials has a sharper onset at the band edge [9], leading to improvements in the efficiency of optoelectronic devices [10, 11]. Also, two- and one-dimensional materials are transparent, flexible, and remarkably strong [12], with applications as one-atom-thick windows and barriers [13] as well as transparent, flexible electronics and optoelectronics. Local oscillations of the electron

density in metals and semiconductors, called surface plasmons, can be engineered by the confinement of electrons in micro- and nanostructures [14, 15]. These types of properties in novel materials are the basis of our search for novel devices, for terahertz technology and otherwise.

This dissertation describes several experiments based in terahertz science of low-dimensional materials. These experiments reveal properties which are fundamental to the development of novel electronic and optoelectronic devices, such as mobility, charge-carrier relaxation dynamics, and plasmonic resonances. We aim to develop novel terahertz technology through nanoscience, and to develop nanoscience through terahertz spectroscopy.

We specifically address the following topics:

- Molybdenum Disulfide ( $\text{MoS}_2$ ) is a layered transition-metal dichalcogenide. Thin structures of  $\text{MoS}_2$  have received interest as a two-dimensional semiconducting platform for transparent, flexible electronics and optoelectronics. But in the search for high-performance devices, little is understood about the ultimate intrinsic limitations on the mobility of this material. In Chapter 3 we present measurements of the high-frequency mobility of thick  $\text{MoS}_2$ , closely related to the thin structures used in devices, and we observe intrinsic mobilities an order of magnitude higher than any previous report.
- The dynamics of charge carriers on sub-picosecond to nanosecond time scales is crucial for the performance of electronic and optoelectronic devices. In Chapter 4, we present terahertz measurements to understand the physics of carrier relaxation for three important technological materials:  $\text{MoS}_2$ , graphene, and germanium nanowires. We demonstrate that the relaxation in  $\text{MoS}_2$  and Ge nanowires is limited by defects, and we show that carrier cooling in graphene is extremely inefficient at low temperatures due to a lack of phase space for

optical phonon scattering.

- Plasmonics, the field of manipulating charge density waves, has typically been a metal-based technology with promise for extreme sub-wavelength optics and infrared/THz active and passive devices. In Chapter 5, we use THz spectroscopy to demonstrate plasmonic effects in semiconductors, which have a tunable carrier density and thus a tunable plasma resonance frequency. We show that plasmonic effects dominate the conductivity of oriented Ge nanowires, and that graphene plasmonic devices, which are particularly exciting for THz applications, can be modeled with classical electromagnetic theory.
- Silicon carbide (SiC) is a material renowned for its hardness, durability, and large band gap for high power electronics. In Chapter 6, we report the generation of THz radiation from optically pumped SiC. We determine the origin of this radiation and evaluate the potential for SiC as a platform for THz optoelectronics.

Completion of these experiments required the fabrication of samples and devices, and the construction and operation of terahertz spectroscopy systems, described in Chapter 2, with cryogenic sample capability.

# Chapter 2

## Terahertz Spectroscopy

### 2.1 The Terahertz Frequency Range

The terahertz frequency range of the electromagnetic spectrum lies between the microwave and the mid-infrared. The precise bounds are up for debate, but the THz range typically refers to frequencies of 0.1–10 THz (i.e. free-space wavelengths of 30–3000  $\mu\text{m}$ ). The associated time scales of 0.1–10 ps are the domain of many physical processes in condensed matter and liquids, such as electronic relaxation, phonon scattering, molecular rotational modes, and plasma oscillations. For example, water vapor that is present in the atmosphere has many absorptive modes in the THz range [16]. Also, as we discuss in Chapter 3, electron-hole momentum relaxation times for the layered material  $\text{MoS}_2$  occur on 0.1–2 ps time scales. THz science is important for studying these processes. There also exist interesting practical applications such as for ultra-high-speed logic and imaging. Since the free-space wavelength at 1 THz is 300  $\mu\text{m}$ , long range imaging using this radiation is considerably higher resolution than with radio waves, and it also penetrates thin, dry obscuring materials such as cardboard or clothing.

Unfortunately, there is a lack of practical sources and detectors for THz radiation,

known as the “terahertz gap”. Useful power generating sources for the THz range are too large, too weak, or require cryogenic temperatures. There exist THz lasers based on molecular transitions, but they are expensive, bulky, and cover only discrete frequencies. THz quantum cascade lasers are a promising semiconductor option for which the frequency can be engineered, but they still require low temperatures and/or strong magnetic fields [17]. Free electron lasers provide high power and excellent tuning throughout the THz range, but they require huge installations the size of a small building [18, 19]. Other options which are commercially available are based on nonlinear optical parametric oscillators pumped with ultrafast lasers [20] or backward wave oscillators, but these are expensive, have powers only up to 1 mW, and too large for many applications outside of a lab. Terahertz emitters based on traveling wave tubes, normally a microwave technology, appear promising but the high frequencies require smaller structures with challenging microfabrication and are not yet available [21]. The time-domain terahertz systems that we use for spectroscopy (see Section 2.3) produce only microwatt average powers and are practical only for lab use. Beyond being an interesting engineering challenge, conquering the terahertz gap is an important scientific endeavor.

## 2.2 FTIR Spectroscopy

Fourier transform infrared (FTIR) spectroscopy is a classic method of measuring linear light-matter interaction over the entire infrared range, from terahertz to near-infrared frequencies [22]. The technique is based on a Michelson interferometer [23] with a translating mirror for one of the interferometer arms. The beams which are recombined after the beamsplitter will interfere constructively, destructively, or somewhere in between, depending on the relative path lengths of the interferometer arms. Varying the mirror position determines an optical path delay ( $\delta$ ), resulting in wave

interference. The total detected intensity,  $I(\delta)$ , will be a function of the optical path delay as [24]

$$\begin{aligned} I(\delta) &= 2 \int_0^\infty I(k) \cos^2(\pi k \delta) dk \\ &= \int_0^\infty I(k) [1 + \cos(2\pi k \delta)] dk \end{aligned} \quad (2.1)$$

where the detection spectrum as a function of (non-angular) wavenumber,  $I(k)$ , is the product of the emitter, beamsplitter, detector, environment, and (possibly) sample spectra.  $I(\delta)$  is known as an interferogram. As seen from Equation 2.1,  $I(k)$  is directly related to the inverse cosine Fourier transform of  $I(\delta)$ .

FTIR spectroscopy may be used to measure the spectrum of an emission source (with a calibrated detector), the spectrum of a detector (with a calibrated source), or the transmission spectrum of a sample. For the measurements presented in this document, we focus on transmission spectroscopy (see Section 5.2). Although less intuitive in operation than a grating spectrometer, which allows only one frequency of light to pass through the spectrometer at a time, FTIR spectrometers are prized for their ability to collect high frequency-resolution spectra over the broadband range, with a high throughput, in a short period of time. Furthermore, they are typically internally calibrated by the use of a co-propagating HeNe laser with a known wavelength to accurately determine the optical path difference.

For our transmission measurements, we use a nitrogen-purged Thermo Scientific Nicolet 8700 FTIR spectrometer. To cover the entire infrared frequency range, we have a variety of emitter, detector, and beamsplitter combinations. For our measurements on graphene plasmonic structures, presented in Section 5.2, we used a silicon carbide glowbar as the source, an intrinsic silicon beamsplitter, and a 4.2 K bolometer detector from Infrared Laboratories. This combination allows for sensitive

transmission measurements in the 1.5–20 THz (50–600  $\text{cm}^{-1}$ ) range.

## 2.3 Time-Domain Terahertz Spectroscopy

We use time-domain terahertz spectroscopy for three reasons: (a) for good signal-to-noise ratio in the 0.2–3 THz range, (b) as a simple, direct measurement of the complex THz refractive index, and (c) as a basis for optical-pump THz-probe spectroscopy, which allows access to the temporal evolution of a sample’s THz conductivity spectrum with sub-picosecond resolution.

Although the bolometers used with FTIR systems have good sensitivity down to 0.5 THz or lower frequencies, their primary limitation on spectroscopy in the sub-3 THz range is the lack of a bright, broadband THz source. The broadband infrared radiation sources typically used in an FTIR are glow bars, most frequently made of silicon carbide. SiC is a robust resistor, capable of withstanding temperatures up to  $\sim 1600$  K. But like all blackbody emitters, its emissivity is subject to Plank’s Law, which decreases as the square of the frequency at long wavelengths. As a result, the signal-to-noise ratio of our FTIR transmission measurements is  $\sim 1/\sqrt{\text{Hz}}$  around 2 THz, and measurements below 1 THz are impractical.

In contrast, THz time-domain spectrometers have an excellent signal-to-noise ratio in the 0.2–3 THz range due to a combination of the gated-pulse detection called electro-optic sampling, as well as emission and detection processes that take advantage of the several-THz frequency bandwidth of an ultrafast laser. Electro-optic sampling measures the complete time-domain waveform of an emitted broadband THz pulse and so can discern both amplitude changes and phase shifts upon transmission through a sample. This information leads to the extraction of the complex index of refraction (or alternatively, the conductivity) of the sample in a single measurement without resorting to techniques such as Kramers-Kronig analysis or Fabry-Pérot

interference for phase-shift information.

### 2.3.1 Emission of Broadband THz Pulses

In a time-domain THz spectrometer, ultrafast optical pulses generate broadband THz-frequency electromagnetic waves. The emitted THz electric field pulses are typically only a single or a few oscillation cycles, and so they are broadband in comparison with their center frequencies. There are various physical emission mechanisms for THz radiation. The most frequently used are nonlinear difference-frequency generation [25], ultrafast surface-charge separation [26], and excitation of a biased photoconductive switch [27, 28]. All of these methods translate the broadband nature of the ultrafast optical pulse to the broadband nature of the THz pulse.

Nonlinear difference-frequency generation is the most common source of broadband THz pulses for a THz time-domain spectrometer. Since the nonlinear down-conversion process becomes more efficient with larger optical pump pulse electric fields, it is more practical for use with a regenerative amplified Ti:Sapphire laser system, with 35 femtosecond pulses and milliJoule energies. The idea is that the various frequency components of the broadband optical pulse mix within a material that has a second-order nonlinearity. This optical mixing occurs through the nonlinear polarization of the material,  $P(\omega)$ , which is described in terms of the system response function  $\chi^{(2)}$  as [29]

$$\vec{P}(\omega) = \epsilon_0 \chi^{(2)}(\omega = \omega_1 - \omega_2) \vec{E}(\omega_1) \vec{E}^*(\omega_2) \quad (2.2)$$

where  $E(\omega)$  is the optical pump pulse electric field and  $\epsilon_0$  is the permittivity of free space. In general, as we discuss further in Chapter 6,  $\vec{P}(\omega)$  is a vector which depends on the polarization of the optical pump pulse through  $\chi^{(2)}$ , which is a tensor. An

oscillating polarization will emit radiation according to [29]

$$\vec{E}(t)^{\text{THz}} \propto \frac{\partial^2 \vec{P}(t)}{\partial t^2}. \quad (2.3)$$

Since  $E(\omega)$  typically has a bandwidth  $>10$  THz, the emitted electric field will be broadband and in principle have significantly sub-picosecond oscillation components covering from 0.1– $>3$  THz. But often phase matching and optical phonon absorption within the nonlinear material are limiting factors to the bandwidth of the emitted radiation. For example, ZnTe has excellent phase matching properties with 780 nm ultrafast pulses, and is thus popular for THz generation via difference frequency generation. But optical phonons limit ZnTe emission to a  $\sim 3$  THz bandwidth.

In most of our experiments with a time-domain THz spectrometer, we use biased photoconductive switches [27, 28] as the emission mechanism. The reason for this is their relative efficiency when using pump pulses with sub-nanoJoule energies. This allows us to generate practical THz pulses using only  $\sim 10$  mW of average power from our non-amplified, ultrafast Ti:Sapphire laser, reserving the majority of the laser power for an optical-pump THz-probe measurement, if desired (see Section 2.5). A broad introduction to photoconductive switches is available in Ref. [29]. The principle is simple: A femtosecond laser pulse excites carriers in a semiconductor between two biased metal strips. The electric field between the strips causes the carriers to accelerate on a sub-picosecond time scale. The carriers then emit radiation according to [29]

$$E(t)^{\text{THz}} \propto \frac{\partial J(t)}{\partial t} \quad (2.4)$$

where  $J(t)$  is the current within the semiconductor. Since the carriers are all excited within a short ( $<100$  fs) time scale and accelerate within a few hundred picoseconds, the emitted THz radiation is broadband, with frequency components extending

from 0.1–3 THz or greater. Many different geometries of metal strips/antennas have been used, as have various semiconducting materials. We have used a simple design modeled directly from Ref. [28], which employs two simple metal strips, spaced 80  $\mu\text{m}$  apart, deposited on semi-insulating (SI) GaAs. We apply a voltage between the strips, typically 50–100 V, and we excite carriers near one of the strips. Due to the high mobility of the SI-GaAs, there is a large current surge within the emitter, and the process of Equation 2.4 is efficient. Furthermore, since the GaAs recombination time is on the order of several hundred picoseconds, all of the excited carriers have recombined by the time the next optical pulse arrives, 12 ns later for our 81 MHz Ti:Sapphire oscillator. For more details regarding the design and packaging of our photoconductive emitters, see Ref. [30].

### 2.3.2 Electro-optic Sampling and Experimental Setup

Electro-optic sampling is a technique for measuring a complex, time-domain THz waveform using ultrafast pulses [27, 28, 31]. Figure 2.1 shows a schematic of a THz time-domain spectrometer using electro-optic sampling for detection. An ultrafast laser generates pulses which are split into two beams, one to drive the emitter (which may be, e.g., a nonlinear crystal or biased photoconductive switch) and one to drive the receiver. One of the beam paths contains a linear stage (LS), which is aligned in a retroreflective manner to control the relative delay between the emission pulses and detection pulses without misalignment. The generated THz electric field is collected, collimated, and focussed with Silicon hyper-hemisphere lenses and metal off-axis parabolic mirrors, and finally, detected at the receiver.

There are a few operational principles for the electro-optic THz receiver, with the two most common being polarization rotation in a nonlinear crystal via the Pockels Effect [29, 30, 31, 32] and gated photoconductive switching [27, 28, 30]. We have

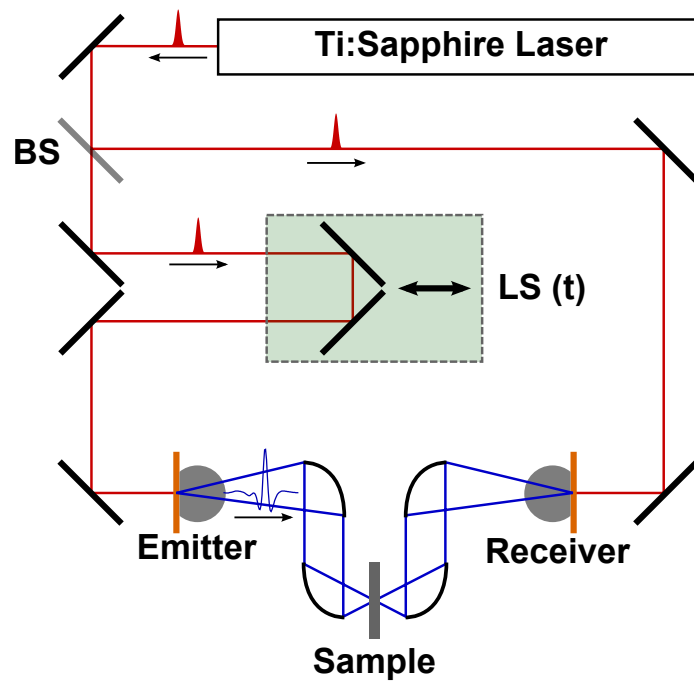


Figure 2.1: Schematic of a terahertz time-domain spectrometer. BS = beamsplitter, LS = linear delay stage. The Ti:Sapphire laser emission is split into two beams, one of which drives the THz emitter, and one of which serves as the electro-optic sampling pulse at the detector. The THz emission beam is collimated and focussed with  $90^\circ$  off-axis parabolic mirrors. Not shown: Additional mirrors at various points to ensure that the beam path lengths are equal such that the pulses arrive at the detector around the same time.

used both methods in our measurements. The key for both of these methods is that they provide a signal *gated* by an ultrashort optical pulse and *proportional* to the amplitude and sign of the THz electric field. Take, for example, gated photoconductive switching, as shown in Figure 2.2. In this design, we deposit metal strips with a few-micron gap onto a semiconducting substrate with a short carrier lifetime, and we measure the current flowing from one strip to the other with a lock-in amplifier [30]. When the optical sampling pulse is absent, the semiconductor is insulating, and no current flows. When the optical sampling pulse arrives, it excites electron-hole pairs in the semiconductor, causing the channel between the strips to become conducting [27]. Thus, the sampling pulse “turns on” the switch, but due to the short carrier lifetime of the semiconductor, the switch remains “on” for only a couple hundred femtoseconds. When the THz electric field arrives, it will produce a current proportional to the electric field polarized across the gap between strips according to Ohm’s Law. But since the gap is only conducting for a short period of time after the sampling pulse arrives, the photoconductive receiver is effectively “gated” by the optical sampling pulse. By varying the time delay between the THz and sampling pulses, and measuring the current at each point, one collects a signal proportional to the complete electric field transient in time.

See the example given in Figure 2.2. The blue trace is an example few-cycle THz electric field pulse, and three possible time delays between the THz and optical sampling pulses are shown. When the linear stage is set such that the sampling pulse arrives at the detector at the same time as the first minimum of the THz pulse, as demonstrated by time delay (A), then the lock-in amplifier will detect a current. At time delay (B), the sampling pulse overlaps the peak THz electric field, and the lock-in amplifier will detect a larger current of opposite sign. Finally, at time delay (C), the sampling pulse arrives at a node in the THz field, producing no current. By scanning

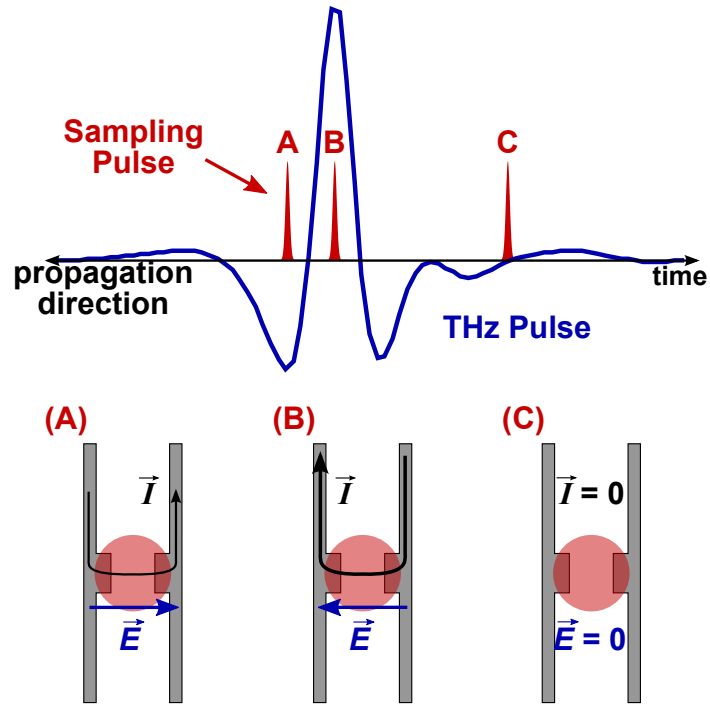


Figure 2.2: Electro-optic sampling of a broadband THz electric field pulse using a photoconductive receiver. For sampling pulses arriving at the detector at different times relative to the THz e-field, the current in the detector strips will be measurably different. Sampling times (A) and (B) represent sampling of e-fields with different amplitude and opposite sign, resulting in corresponding detector current. Sampling time (C) represents sampling of a node in the THz e-field, resulting in zero detector current.

the linear stage and sampling each point of the THz field in this way, we effectively collect the cross-correlation of the THz electric field with the receiver response, given

$$J_d(t) = \int_{-\infty}^t \sigma_d(t-t')E^{\text{THz}}(t')dt' \quad (2.5)$$

where  $J_d(t)$  is the current measured by the lock-in amplifier as a function of the sampling time,  $t$ . We typically assume that the detector response, given by the time-dependent conductivity  $\sigma_d(t)$ , is very short compared to the time-dependence of the THz electric field  $E^{\text{THz}}(t)$ . So in that case,  $J(t) \propto E^{\text{THz}}(t)$ . In reality, the sampling pulse has some finite width ( $\sim 90$  fs), and the carrier lifetime is somewhat longer ( $\sim 250$  fs). This broadens the finer features of the detected signal, limiting the detection bandwidth to  $\sim 3$  THz in our case. The bandwidth of electro-optic sampling via the Pockels effect in a nonlinear crystal is in principle limited only to the optical sampling pulse width since the material polarization is essentially instantaneous. However, phase matching and phonon absorption can limit the bandwidth in practical materials.

## 2.4 Optical Parameter Extraction from Transmission Measurements

In a terahertz transmission measurement, the goal is to extract the linear optical parameters of a sample. Often, the relevant parameter is the refractive index, which can be complex. Alternatively, one may use the optical conductivity or dielectric (or diamagnetic) susceptibility, depending on suitability and convenience. In any case, the linear response of the sample consists of a frequency-dependent absorption and phase shift. Both of these changes are directly measured in a THz time-domain spectrometer, and one can extract the complex refractive index from the raw electric fields transmitted through the sample and reference, which together contain the absorption and phase shift information. A simple FTIR measurement reveals only the THz power transmission, which does not include phase information.

### 2.4.1 Two-Dimensional Sheet Conductivity

Refractive index is an inappropriate concept for graphene and other two-dimensional materials. After all, the velocity of light propagating through a 2-D material is meaningless. Rather, the dielectric permittivity and/or the conductivity are appropriate optical parameters to describe an absorption and phase shift. In this vein, we model graphene and other 2-D materials as an infinitely thin sheet conductivity at a dielectric interface. The effect of the 2-D conductivity ( $\sigma$ ) on the transmission of electric ( $E$ ) and magnetic ( $H$ ) fields through this interface is then merely a term in the boundary conditions given by Maxwell's equations[33]:

$$E_i + E_r = E_t \quad \text{and} \quad H_i - H_r = H_t + \sigma E_t \quad (2.6)$$

The indices “i”, “r”, and “t” refer to the incident, reflected, and transmitted waves at the interface, respectively, and  $\sigma$  is the 2D sheet conductivity. Let  $n_1$  and  $n_2$  be the refractive indices of the media on either side of the 2D sheet, such that  $H_i = n_1 E_i / \eta_0$ ,  $H_r = n_1 E_r / \eta_0$ , and  $H_t = n_2 E_t / \eta_0$ , where  $\eta_0$  is the impedance of free space. Then the electric field amplitude transmission through the interface is

$$t = \frac{E_t}{E_i} = \frac{2n_1}{n_1 + n_2 + \eta_0 \sigma} \quad (2.7)$$

In a THz transmission measurement, for which the frequency-dependent 2D conductivity ( $\sigma(\omega)$ ) is of interest, one measures the THz waves transmitted through the interface both with,  $E_\sigma(\omega)$ , and without,  $E_0(\omega)$ , the conductive sheet. Then the normalized transmittance is

$$t(\omega) = \frac{E_\sigma(\omega)}{E_0(\omega)} = \frac{1}{1 + \frac{\eta_0 \sigma(\omega)}{n_1 + n_2}} \quad (2.8)$$

from which  $\sigma(\omega)$  can be determined. Notice that  $n_1$  and  $n_2$ , and any potential frequency dependence therein remain in this normalized expression.

For an FTIR measurement, the relevant normalized expression is in terms of the transmitted power ( $|E_\sigma/E_0|^2$ ). In this case, when  $\eta_0 \sigma(\omega)/(n_1 + n_2) \ll 1$ , the normalized power transmission is related to only the real part of  $\sigma(\omega)$ . Thus, the normalized transmission spectrum describes the absorption of radiation in the material.

For a THz time-domain measurement, we must deconvolve the reference electric field to extract the material transmission. This is most easily accomplished in the frequency domain:

$$t(\omega) = \frac{\mathcal{F}[E_\sigma(t)](\omega)}{\mathcal{F}[E_0(t)](\omega)} \quad (2.9)$$

where  $\mathcal{F}$  is the Fourier transform operator.

### 2.4.2 Complex Refractive Index of a Material with Finite Thickness

A material with finite thickness is no longer simply a boundary condition on the transmitted THz radiation. The radiation accumulates phase as it propagates through the sample and can reflect at each edge, so modeling the sample as an etalon is appropriate. We use the exact solution for the transmission of light through an etalon with a refractive index  $n(\omega)$  and thickness  $d$ , surrounded by air ( $n_{\text{air}} = 1$ ),

$$\frac{E_t(\omega)}{E_0(\omega)} = \frac{4n(\omega)e^{i\frac{\omega d}{c}(n(\omega)-1)}}{(n(\omega) + 1)^2 - (n(\omega) - 1)^2e^{-2i\frac{\omega d}{c}n(\omega)}} \quad (2.10)$$

Here,  $E_t(\omega)$  is the measured electric field transmitted through the sample, and  $E_0(\omega)$  is the measured electric field with the sample removed, defined analogously to Equation 2.9. Extracting the index of refraction requires a computational search for complex values of  $n(\omega)$  that solve Equation 2.10 at each frequency.

Equation 2.10 can be simplified in the limit  $\omega d/c \ll 1$  (i.e. the long-wavelength limit):

$$\begin{aligned} t(\omega) &\approx \frac{4n(\omega)[1 + i\frac{\omega d}{c}(n(\omega) - 1)]}{4n(\omega) - 2i\frac{\omega d}{c}n(\omega)(n(\omega) - 1)^2} \\ &\approx \left[1 - i\frac{\omega d}{2c}(n(\omega)^2 - 1)\right]^{-1} \end{aligned} \quad (2.11)$$

For the measured THz refractive index of MoS<sub>2</sub>,  $n(\omega) \approx 3.0$ , and the thickness of our sample,  $d \approx 4 \mu\text{m}$ , the approximation in the above expression is extremely good, as illustrated in Figure 2.3.

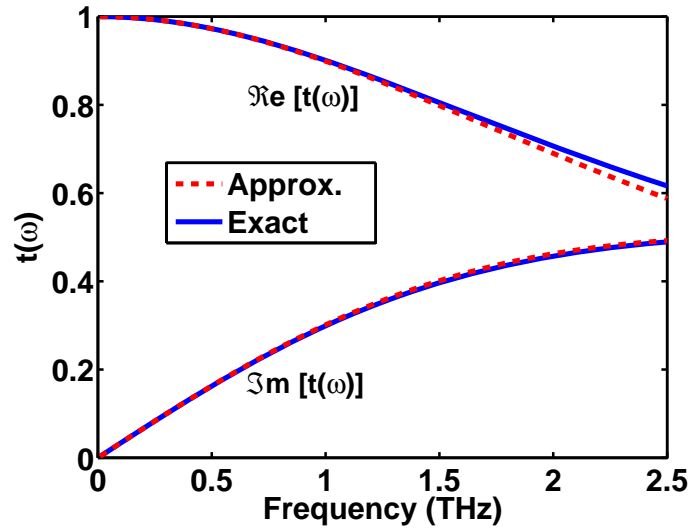


Figure 2.3: The real and imaginary parts of the transmission for Equations 2.10 and 2.11 using  $n(\omega) = 3$  and  $d = 4 \mu\text{m}$ .

## 2.5 Optical-Pump Terahertz-Probe Spectroscopy

Optical-pump THz-probe spectroscopy is a variant of the venerable optical pump-probe techniques that have been a mainstay of ultrafast science since the advent of modelocked lasers[34, 35, 36]. This approach is a powerful way to directly measure ultrafast relaxation processes in materials rather than indirectly accessing them through steady-state measurements. The idea is to take advantage of the time-domain nature of the THz time-domain spectrometer to study the temporal evolution of the sample's THz response. This is accomplished by incorporating another beam into the setup, the pump, the pulses of which excite the sample at some point before, during, or after the arrival of the THz pulse. By varying the time delay between the optical pump pulses and the THz probe electric field pulses, the THz pulse transmission follows the evolution of the non-equilibrium state excited by the pump. Due to the large probe photon energies in all-optical pump-probe measurements ( $\sim 0.5\text{--}3 \text{ eV}$ ), they are primarily sensitive to interband electronic effects such as Pauli blocking from band filling dynamics[34, 35, 36].

In contrast, the THz probe, with typical energies of 1–15 meV, is sensitive primarily to the intraband conductivity of the sample, that is, the free-carrier response[37, 38, 39, 40, 41, 42]. In addition, since the probe pulse is broadband, there is the potential to measure frequency-dependent free-carrier dynamics, which we take advantage of in our study of Ge nanowires and MoS<sub>2</sub>. However, despite the probe being a broadband pulse which could be several picoseconds in duration, the temporal resolution of the dynamics is still sub-picosecond, as we discuss in Subsection 2.5.3. The flexibility of the optical-pump THz-probe approach, as well as the general importance of free-carrier dynamics to both fundamental and applied science, has promoted the application of optical-pump THz-probe to a wide variety of material systems[43, 44, 45].

Even in the absence of temporal dynamics, the optical-pump THz-probe technique is a powerful tool for measuring the mobility of semiconductors. The mobility is related to the frequency-dependent intraband conductivity,  $\sigma(\omega)$ , of materials. A static transmission experiment can sometimes be useful to extract  $\sigma(\omega)$  in 2-D (see Equation 2.8) and 3-D (see Equation 2.11 with the substitution  $n^2(\omega) = n^2 + i\sigma(\omega)/(\omega\epsilon_0)$ , where  $\epsilon_0$  is the permittivity of free space). But for undoped or lightly doped samples in 3-D, the effect of the refractive index on the transmission can overwhelm the effect of  $\sigma(\omega)$ . For instance, the large value of  $n$  and the small value of residual doping in our MoS<sub>2</sub> samples had the result that the unpumped, static transmission measurements could not reliably determine the frequency dependence of the conductivity and thereby the mobility. In contrast, since the change in THz transmission,  $\Delta E(\omega)$ , between pumped and unpumped samples is directly proportional to the change in the conductivity  $\Delta\sigma(\omega)$ , optical-pump THz-probe spectroscopy is a highly-sensitive method to extract the frequency-dependent conductivity.

### 2.5.1 Experimental Setup

In the optical-pump THz-probe scheme, depicted in Figure 2.4, 780 nm center wavelength (1.58 eV), sub-100 fs optical pulses excite electron and hole distributions in the sample, after which the distributions cool and recombine. The field of the THz pulse transmitted through the pumped sample,  $E_p(t, u)$ , is sensitive to the evolving conductivity and, therefore, depends on the pump-probe delay  $u$ . In our experiments, the incident optical and THz pulses are mechanically chopped at different frequencies and the transmitted THz pulse is measured at the sum frequency. We therefore measure the change in the transmitted THz pulse,  $\Delta E(t, u) = E_p(t, u) - E_0(t)$ , in the presence ( $E_p$ ) and absence ( $E_0$ ) of optical pumping.  $\Delta E(t, u)$  contains information of both the amplitude and phase changes of  $E_0(t)$  upon pumping. In all further discussions, the symbol  $\Delta$  signifies the change in a quantity due to optical pumping.

Figure 2.4 shows a schematic of a typical optical-pump terahertz-probe setup we use in our lab. The position of linear stage LS1 determines the THz sampling time,  $t$ , and the position of linear stage LS2 determines the pump-probe delay,  $u$ . More specifically,  $u$  is defined as the time delay between the optical pump pulse and the THz sampling pulse. Notice that we split the optical pump beam from the THz emission beam with beamsplitter BS2 before the THz sampling linear stage LS1. In this configuration, varying LS1 (during a scan of THz sampling time  $t$ ) scans the THz pulses relative to the sampling pulses, but it leaves constant the relative delay between the pump and THz sampling pulses. Figure 2.5 depicts this scenario. As we discuss in Subsection 2.5.2, this arrangement is important for deconvolving the reference electric field from the optical-pump THz-probe signal for small pump-probe delays.

With our unamplified Ti:Sapphire pulsed laser system, we require THz radiation emitters and detectors which use little pulse energy. This restriction essentially pre-

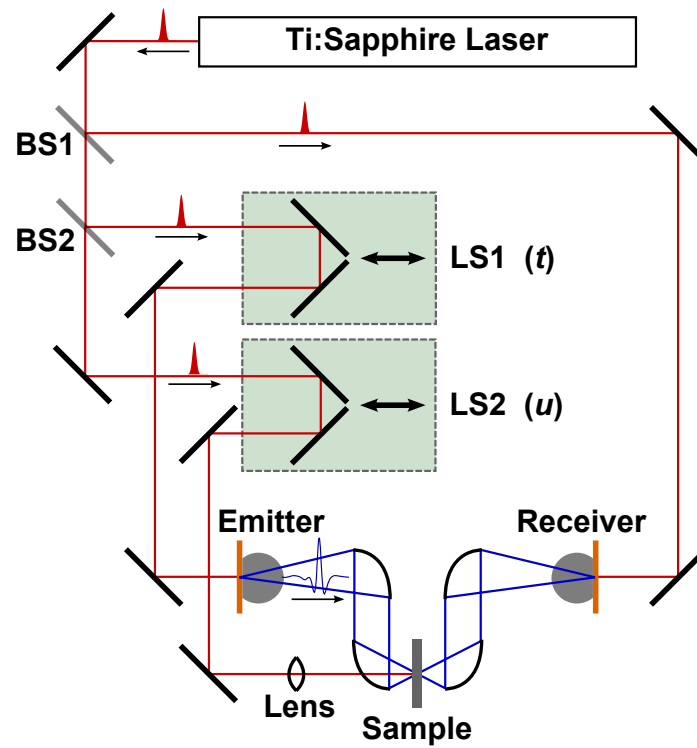


Figure 2.4: Schematic of an optical-pump THz-probe experiment. The Ti:Sapphire laser emission is split into three beams, two of which have delay stages. Not shown: Additional mirrors at various points to ensure that the beam path lengths are equal.

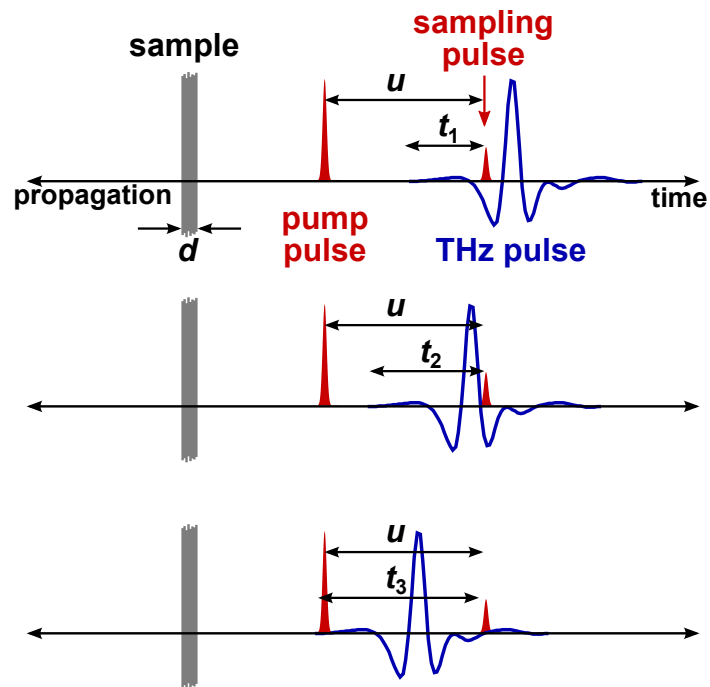


Figure 2.5: Cartoon depicting three possible relative delays between the pump pulse, THz pulse, and sampling pulse. The variable  $u$  refers to the time delay between the pump and sampling pulses, and the variables  $t_x$  refer to the time delay between the sampling pulse and the start of the THz pulse. These three scenarios show three different positions of linear stage LS1, for a fixed position of LS2. Scanning LS1 in this way implements the time-shift procedure discussed in Subsection 2.5.2.

cludes THz generation from nonlinear optical rectification in our setup, so we instead use photoconductive emitters. Our ultrafast laser produces  $\sim 1.5$  W average power, of which the photoconductive emitter and detector each consume  $< 50$  mW, leaving  $\sim 1.4$  W remaining for the optical pump beam. Accounting for additional loss among optical elements in the setup, we typically have 10–15 nJ optical pump pulses at 785 nm center frequency.

Practically, incorporating the pump beam requires a few considerations, as hinted at in Figure 2.4. First, spot size of the optical pump beam on the sample is important. Generally, the largest overall optical-pump THz-probe signal occurs when the pump beam is around the same size as the probe beam. But when the pump and THz spot sizes are similar, the pump will not excite a uniform carrier density across THz spot. The result is that the higher frequencies within the THz probe bandwidth are preferentially modulated by the pump since they are focussed more tightly to the center. This issue adds an artificial frequency dependence to the conductivity spectrum, and it is apparent in our measurements of Ge nanowires (see Figure 5.3). To ameliorate this problem in cases where extracting the frequency-dependent conductivity is important, we simply defocus the pump spot such that it is considerably larger than the THz spot, at the cost of some pump fluence. Typically the full width at half maximum (FWHM) of the THz focus spot in our sample is around 0.5–0.6 mm, while it is  $\geq 1$  mm for the pump at the same location, resulting in maximum pump fluences of  $\sim 1$ – $1.5$   $\mu\text{J}/\text{cm}^2$  on the sample.

Another important consideration is the angle of incidence of the pump and THz beams on the sample, which is ideally normal for both. If the pump is not at normal incidence, then different parts of the pump wavefront will excite the sample at different times, effectively reducing the pump-probe temporal resolution. For example, if the pump angle of incidence is  $45^\circ$ , then with a THz spot size of 0.5 mm, there will

be temporal smearing of  $(0.5 \text{ mm})/(c\sqrt{2}) = 1.18 \text{ ps}$ . In order to facilitate normal incidence in our setup, the pump excites the sample through a hole in the nearest off-axis parabolic mirror.

### 2.5.2 Conductivity Extraction and Time-Shift

THz frequency radiation is sensitive to the frequency-dependent THz conductivity,  $\sigma(\omega)$  of a sample, which contains information about the carrier density and the mobility. By incorporating the optical pump pulse into a THz time-domain spectrometer, the ultimate goal in an optical-pump THz-probe experiment is to extract this conductivity as a function of time after the pump pulse,  $\sigma(\omega, u)$ . Alternatively, if the sample is somewhat conductive in equilibrium, we may be interested in the difference between the pumped and equilibrium conductivities,  $\Delta\sigma(\omega, u) = \sigma(\omega, u) - \sigma_0$ , again as a function of pump-probe delay.

There are a variety of approaches to extract the THz conductivity in an optical-pump THz-probe experiment. The choice of approach generally boils down to the type of material under study and what assumptions about the specific sample are appropriate. The three most important aspects of a sample that determine the approach to analysis are: (i) the thickness of the sample to the THz electric field (i.e. thickness and refractive index), (ii) its optical depth (i.e. the strength of pump absorption), and (iii) the nature (including duration) of the current response to the THz electric field. As discussed in Subsections 2.4.1 and 2.4.2, it is necessary to treat 2-D and 3-D materials differently, and the treatment of 3-D materials can be simplified in the long-wavelength limit. Of the three materials we have studied via optical-pump THz-probe spectroscopy, the epitaxial graphene and thin-films of Ge nanowires were thin enough to be treated as 2-D, while the  $4 \mu\text{m}$  thick  $\text{MoS}_2$  sample was considered 3-D in the long-wavelength limit. Also, the optical depth of the material is important

because if the sample is thick enough, the pump will be entirely absorbed within only a part of the sample, and so the pump excitation will be non-uniform throughout its depth[46]. All of the materials we have measured can be considered optically thin. Finally, if the current response is long-lasting compared to the duration of the THz pulse, it will complicate the extraction of  $\Delta\sigma(\omega, u)$ , as elegantly explained by Nienhuys *et al.*[47]. This is the case in our low-temperature measurements of MoS<sub>2</sub>. Since these samples require different analyses, we will present them along with the results.

But regardless of the form of analysis, all optical-pump THz-probe experiments must deconvolve the reference electric field,  $E_0$  from the  $\Delta E$  signal. Beard *et al.*[46] has a nice illustration of the problem: Suppose one wants to measure the change of the entire THz electric field due to the presence of a pump pulse. If, for example, the relative delays of the pulses are such that the pump arrives at the sample during the middle of the THz oscillation, then only the final half of the THz pulse will be modified by the photoexcited conductivity. If one were to fix the relative delays of the pump and THz pulses, and then scan the sampling pulse to measure the change of the THz field, then there would only be a change *after* the pump pulse arrives. This is a result of the fact that each sampled point of the THz field has a different delay relative to the pump; some of the field occurs before, some during, and some after the pump. In this case, it is impossible to deconvolve the reference electric field from the measured optical-pump THz-probe signal without additional processing.

Mathematically, this scenario is represented as follows. We assume that the current density  $J(t, u)$  in the sample for pump-probe delay  $u$  in the presence of the field  $E(t, u)$  of a THz pulse and a time-dependent DC conductivity  $\sigma_{\text{DC}}(t + u)$  is[47],

$$J(t, u) = [E(t, u)\sigma_{\text{DC}}(t + u)] \otimes j(t) \quad (2.12)$$

Here,  $j(t)$  is the normalized current impulse response ( $\int_{-\infty}^{\infty} dt j(t) = 1$ ) and  $\otimes$  is the

convolution operator with respect to  $t$ . This is the most general way of writing the current response if the current density obeys the operator equation,

$$\hat{L}J(t, u) \propto E(t, u)\sigma_{\text{DC}}(t + u) \quad (2.13)$$

where,  $\hat{L}$  is a linear-time-invariant (LTI) differential operator. However, the electric field  $E(t)$  cannot be easily deconvolved from Equation 2.12 to retrieve the desired sample response, which is the DC conductivity times the frequency (or time) dependence. So we make a coordinate substitution (i.e. a *time shift* operation on the pump-probe delay),  $u \rightarrow u - t$ . This time shift operation is easily implemented during data collection by scanning the pump-probe delay ( $u$ ) simultaneously with the THz sampling time ( $t$ )[37, 47, 48], such that  $u - t$  is fixed, as depicted in Figure 2.5. Equation 2.12 then gives:

$$\tilde{J}(t, u) = J(t, u - t) = E(t, u - t) \otimes [\sigma_{\text{DC}}(u - t)j(t)] = \tilde{E}(t, u) \otimes \tilde{\sigma}(t, u) \quad (2.14)$$

The change  $\Delta\tilde{J}(t, u)$  in the current density in the presence and absence of pumping is  $\tilde{J}_p(t, u) - J_0(t)$ . Here, the subscripts p and 0 indicate the value with and without optical pumping, respectively. Therefore, one obtains

$$\begin{aligned} \Delta\tilde{J}(t, u) &= \tilde{\sigma}_p(t, u) \otimes \tilde{E}_p(t, u) - \sigma_0(t) \otimes E_0(t) \\ &= (\Delta\tilde{\sigma}(t, u) + \sigma_0(t)) \otimes (\Delta\tilde{E}(t, u) + E_0(t)) - \sigma_0(t) \otimes E_0(t) \\ &= \Delta\tilde{\sigma}(t, u) \otimes E_0(t) + \sigma_0(t) \otimes \Delta\tilde{E}(t, u) + \Delta\tilde{\sigma}(t, u) \otimes \Delta\tilde{E}(t, u) \end{aligned} \quad (2.15)$$

By applying a Fourier transform with respect to  $t$  to each term, we have,

$$\Delta\tilde{J}(\omega, u) = \Delta\tilde{\sigma}(\omega, u)E_0(\omega) + \sigma_0(\omega)\Delta\tilde{E}(\omega, u) + \Delta\tilde{\sigma}(\omega, u)\Delta\tilde{E}(\omega, u) \quad (2.16)$$

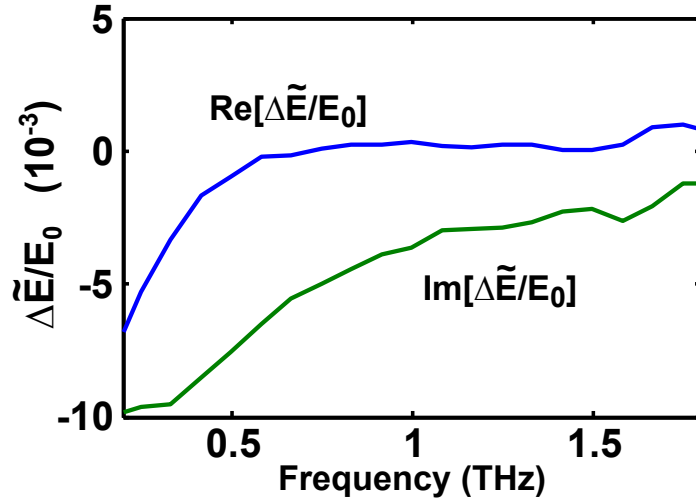


Figure 2.6: The real and imaginary parts of the ratio  $\Delta\tilde{E}(\omega, u)/E_0(\omega)$  for  $u = 5$  ps and maximum pump fluence at 45 K in our optical-pump THz-probe measurement of multilayer MoS<sub>2</sub>.

The time shift operation of Equation 2.14 thus allows for the simple deconvolution of  $E_0$  in the frequency domain using Equation 2.16 provided the final two terms on the right hand side of Equation 2.16 are negligibly small compared to the first term. We empirically confirm that this is the case for all of our optical-pump THz-probe measurements. For example, in Figure 2.6, we show a representative measured ratio of  $\Delta\tilde{E}(\omega, u)/E_0(\omega)$  for our measurements of MoS<sub>2</sub>, which is at most on the order of  $10^{-2}$  for the highest pump fluence used in our experiments. For all other temperatures, pump fluences, and pump-probe delays, this ratio is either similar or smaller. Since  $\Delta\tilde{E}(\omega, u) \ll E_0(\omega)$  at all frequencies, we can safely neglect  $\Delta\tilde{\sigma}(\omega, u)\Delta\tilde{E}(\omega, u)$  compared to  $\Delta\tilde{\sigma}(\omega, u)E_0(\omega)$  in Equation 2.16. For the cases of epitaxial graphene and Ge nanowires, the ratio of  $\Delta\tilde{E}(\omega, u)/E_0(\omega)$  is similar.

Continuing the example of MoS<sub>2</sub>, as we will see in Subsection 3.1.1, the ratio  $|\Delta\tilde{J}(\omega, u)/\Delta\tilde{E}(\omega, u)| \geq 2/(\eta_0 d) \approx 1300 \text{ S m}^{-1}$ . In contrast, the measured value of the unpumped DC conductivity  $\sigma_0(\omega = 0)$  is smaller than  $20 \text{ S m}^{-1}$  and, therefore,  $|\sigma_0(\omega)| \ll |\Delta\tilde{J}(\omega, u)/\Delta\tilde{E}(\omega, u)|$  at all frequencies. Consequently, we can also neglect

$\sigma_0(\omega)\Delta\tilde{E}(\omega, u)$  compared to  $\Delta\tilde{\sigma}(\omega, u)E_0(\omega)$  in Equation 2.16. Similarly for our epitaxial graphene and Ge nanowires experiments, we empirically verify that we are justified in our neglect of the  $\sigma_0(\omega)\Delta\tilde{E}(\omega, u)$  term. So we have

$$\Delta\tilde{J}(\omega, u) \approx \Delta\tilde{\sigma}(\omega, u)E_0(\omega) \quad (2.17)$$

where,  $\Delta\tilde{\sigma}(\omega, u)$  equals  $\mathcal{F}[\Delta\sigma_{\text{DC}}(u-t)j(t)]$ . Here,  $\mathcal{F}$  is the Fourier transform operator with respect to  $t$ .  $\Delta\tilde{\sigma}(\omega, u)$  can be obtained easily using the above Equation.

In general,  $\Delta\tilde{\sigma}(\omega, u)$  does not equal  $\Delta\sigma(\omega, u) = \Delta\sigma_{\text{DC}}(u)j(\omega)$ [47]. However, if the DC conductivity is changing slowly compared to the duration of the current impulse response  $j(t)$  then  $\Delta\tilde{\sigma}(\omega, u) \approx \Delta\sigma(\omega, u)$ . Since the carrier density, and therefore the DC conductivity, varies slowly for  $u \geq 5$  ps in all of our measurements, we have extracted  $\Delta\sigma(\omega, u)$  using this simple relation for  $u \geq 5$  ps. But extracting  $\Delta\sigma(\omega, u)$  from  $\Delta\tilde{\sigma}(\omega, u)$  for cases when the DC conductivity varies rapidly compared to the current impulse response requires a set of transformations[47]:

$$\begin{aligned} \Delta\tilde{\sigma}(t, u) &= \mathcal{F}^{-1}[\Delta\tilde{\sigma}(\omega, u)] \\ \Delta\sigma(t, u) &= \Delta\tilde{\sigma}(t, u+t) \\ \Delta\sigma(\omega, u) &= \mathcal{F}[\Delta\sigma(t, u)] \end{aligned} \quad (2.18)$$

These transformations essentially undo the time-shift operation of Equation 2.14, and they can add considerable noise. Accordingly we have employed them only to extract the DC conductivity changes in MoS<sub>2</sub> at low temperatures (for which the current response is greater than 0.25 ps) and for small pump-probe delays,  $-2 < u < 5$  ps.

### 2.5.3 Optical-Pump THz-Probe Temporal Resolution

The ultimate limit of the temporal resolution of the optical-pump THz-probe system is often misunderstood. After all, the duration of the cross-correlation between the pump and probe pulses usually determines the temporal resolution in an ultrafast experiment. Since the THz pulse is a couple of picoseconds in duration, how is it that optical-pump THz-probe achieves sub-picosecond resolution? Due to the electro-optic sampling method, as well as the data analysis described above, the temporal resolution is fundamentally limited by the bandwidth of the detection spectrum. One can make an assumption of a delta function optical pump pulse, as well as a very short conductivity response time (i.e. fast carrier scattering), but in the end the pump-probe signal is carried on the THz pulse. It is impossible to measure a change in the THz pulse faster than the detector can respond, so ultimately that will limit the pump-probe delay resolution.

In the complete analysis, including the transformations of Equations 2.18, this limitation is explicit in the nature of the Fourier transforms. For example, inverse Fourier transforming pump-probe data with a 2 THz bandwidth will give a  $1/(2 \times 2 \text{ THz}) = 0.25 \text{ ps}$  resolution in the pump-probe delay, which is a fundamental limit. Padding the Fourier transform beyond 2 THz results in a finer array of pump-probe delay points, but it will not add any information. In the simpler analysis, for which we assume  $\Delta\tilde{\sigma}(\omega, u) = \Delta\sigma(\omega, u)$ , and which is valid for short material response times (i.e. fast scattering), this limitation on the pump-probe delay resolution is implicit. Despite sampling many pump-probe delays with an arbitrarily fine sampling resolution, there will not be a change in the THz electric field faster than the detector can respond.

Other factors beside the detector response time can limit the pump-probe delay resolution. If the propagation path from the surface of the sample to the detector is frequency-dependent, it could potentially limit the overall detection spectrum, inde-

pendent of the detector spectrum. For example, phonon absorption might limit the THz transmission of the sample to 2 THz, limiting the pump-probe delay resolution to 0.25 ps even if the detector response is much faster. An important subtlety is that although the emission spectrum might limit the overall bandwidth of the measured signal, it will not limit the pump-probe delay resolution. The pump-THz interaction is essentially non-linear, and so in principle it can alter the THz electric field to produce frequencies above the emission spectral band. As long as the detector is able to measure that faster response, the pump-probe delay resolution won't be limited by the emission spectrum.

In practice, the key to determining the pump-probe delay resolution is to observe the optical-pump THz-probe conductivity bandwidth measured with a good signal-to-noise ratio. For example, in the case of our measurements of MoS<sub>2</sub>, we have a THz emission/detection spectral bandwidth through the sample of >2.5 THz. But the bandwidth of the extracted conductivity is only ~1.8 THz with a good signal-to-noise ratio. So the pump-probe delay resolution of this experiment is limited by the detection bandwidth to  $(2 \times 1.8 \text{ THz})^{-1} = 0.28 \text{ ps}$ .

# Chapter 3

## Mobility of Multilayer Molybdenum Disulfide

Layered two-dimensional transition metal dichalcogenides have recently enjoyed a resurgence of interest from the scientific community both from a new science perspective and also for novel applications[49, 50, 51, 52, 53, 54, 55, 56, 57, 58]. In contrast to graphene, metal dichalcogenides have non-zero bandgaps and are also efficient light emitters, making them attractive for electronics and optoelectronics[49, 50, 51, 52, 53, 54, 55, 56, 57, 58]. The ability to synthesize atomically thin semiconducting crystals and their heterostructures and transfer them to arbitrary substrates has opened the possibility of transparent, flexible electronics and optoelectronics based on these material systems[58, 59, 60, 61, 62, 63, 64, 65]. The best reported carrier mobilities in metal dichalcogenides, typically in the few hundred  $\text{cm}^2\text{V}^{-1}\text{s}^{-1}$  range for  $\text{MoS}_2$ [66, 67], are not as large as in graphene. But the reported mobilities are large in comparison to those of organic materials often used for flexible electronics[49]. Physical mechanisms limiting the mobility of monolayer and multilayer  $\text{MoS}_2$  field effect transistors have been the subject of several experimental[68, 66, 69, 67, 70, 71, 72] and theoretical[73, 74] investigations. Charged impurity scattering, electron-phonon

interaction, and screening by the surrounding dielectric environment are all believed to affect the mobility. Due to the challenge of isolating these effects, the intrinsic mobility of MoS<sub>2</sub>, and the ultimate performance of electronic devices, remains unclear. Similarly, carrier intraband and interband scattering and relaxation rates, which determine the performance of almost all proposed and demonstrated electronic and optoelectronic metal dichalcogenide devices, remain poorly understood.

In this chapter, we present optical-pump THz-probe measurements of the time- and frequency-dependent conductivity of multilayer MoS<sub>2</sub>. Previously reported electrical measurements[66, 69, 67, 70] have probed the MoS<sub>2</sub> DC carrier transport, and all-optical measurements[75, 72] have probed the exciton temporal dynamics. In contrast, optical-pump THz-probe spectroscopy can measure the time development of the complex intraband conductivity in the 0.2-2.0 THz frequency range with a temporal resolution better than a few hundred femtoseconds. The frequency dependence of the measured intraband conductivity leads to the direct extraction of the carrier momentum scattering rate, from which the carrier mobility can be determined in a contact-free way. In addition, the temporal development of the intraband conductivity reveals carrier interband and intraband relaxation dynamics.

Our results show that the momentum scattering times in multilayer MoS<sub>2</sub> vary from  $\sim 90$  fs at 300 K to  $\sim 1.46$  ps at 30 K, corresponding to carrier mobilities of  $\sim 257$  and  $\sim 4200$  cm<sup>2</sup>V<sup>-1</sup>s<sup>-1</sup>, respectively. The temperature dependence of the momentum scattering rate reveals that the mobility is limited by acoustic phonon scattering and the measured scattering times agree well with the theoretical predictions[73, 74]. The measured mobility values are almost an order of magnitude larger than the previously reported values in multilayer MoS<sub>2</sub> devices[68, 69, 67]. Our results indicate that the mobilities in reported MoS<sub>2</sub> electronic devices[68, 66, 69, 70, 71] are likely limited by extrinsic mechanisms (defects, impurities, grain boundaries, etc.) and point to the

ultimate performance of metal dichalcogenide electronic devices.

Much of the material presented in this Section appears in Ref. [76] and was a collaboration between myself, Parinita Nene, and Farhan Rana.

### 3.1 Experiment and Results

The multilayer MoS<sub>2</sub> sample used in this study was cleaved from a large piece of natural MoS<sub>2</sub> (SPI Supplies). We adhered the resulting flake to completely cover a 2 mm clear aperture and mounted the sample in a cryostat (Oxford MicrostatHe, rectangular tail). By measuring the broadband optical transmission interference fringes and using existing index of refraction data[77], we determined that the average thickness of the flake was 4  $\mu\text{m}$ , with variations of  $\pm 0.5 \mu\text{m}$  across the aperture. We optically excited electron-hole pairs in the MoS<sub>2</sub> using sub-100 fs pulses from a Ti:Sapphire oscillator with a center frequency of 785 nm, pulse repetition rate of 81 MHz, and maximum fluence of 1.2  $\mu\text{J cm}^{-2}$ . As depicted in Figure 4.1, and discussed further in Section 4.1, these pulses excite electron and hole distributions at the six  $\Lambda$  points and the  $\Gamma$  point, respectively, as well as from defect states, after which the distributions cool and recombine. We used synchronized, few-cycle THz pulses, generated and detected with photoconductive switches in a THz time-domain spectrometer (see Chapter 2), to probe the excited carrier distribution. We mechanically chopped the optical pump and THz probe beams at 400 and 333 Hz, respectively, and we demodulated the detected photocurrent, proportional to the change in the THz electric field  $\Delta E(t, u)$ , with a lock-in amplifier at the sum frequency.

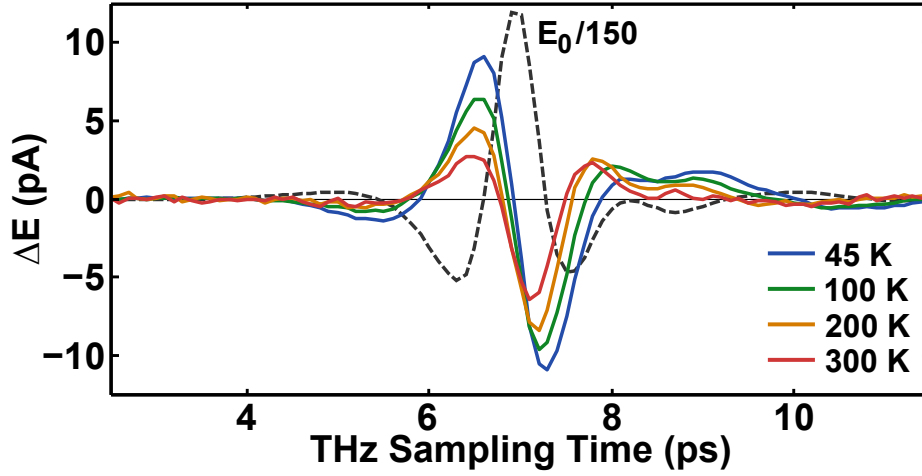


Figure 3.1: (Solid) Measured  $\Delta E(t, u)$  in units of detector current for a fixed pump-probe delay  $u = 5$  ps.  $\Delta E(t, u = -5$  ps) is subtracted for clarity. (Dashed) The scaled reference THz pulse  $E_0(t)$

### 3.1.1 Conductivity Spectra and Momentum Scattering Times

Figure 3.1 shows the measured  $\Delta E(t, u)$  for a fixed pump-probe delay of  $u = 5$  ps at different temperatures. We also display  $E_0(t)$ , which was essentially temperature-independent.  $\Delta E(t, u)$  contains information of both the amplitude and phase changes of  $E_0(t)$  upon pumping. Comparison of  $\Delta E(t, u)$  and  $E_0(t)$  shows a trend of increasing phase shifts with decreasing temperatures due to photoexcited carriers. Thus, both the amplitude and the phase of the transmitted THz pulse are needed to determine the sample response.

The sample response can be determined from the measured change in the transmitted THz pulse,  $\Delta E(t, u)$ , as follows. We start with Equation 2.11 for the transmission of THz radiation through a three-dimensional sample. In the case of a conductive medium, with conductivity  $\sigma(\omega)$ , the complex refractive index is,  $n^2(\omega) = n^2 + i\sigma(\omega)/\omega\epsilon_0$ . Here,  $n$  is the frequency-independent refractive index and  $\epsilon_0$  is the permittivity of free space. The inverse Fourier transform of the relation in Equation

2.11 gives

$$\frac{\partial E_t(t)}{\partial t} = -\frac{2}{\epsilon_0(n^2 - 1)\eta_0 d} [E_t(t) - E_i(t)] - \frac{1}{\epsilon_0(n^2 - 1)} J(t) \quad (3.1)$$

Where  $d$  is the thickness of the MoS<sub>2</sub> flake,  $E_i(t)$  is the initial THz electric field, and  $E_t(t)$  is the field transmitted through the sample. Subtracting versions of the above equation in the presence and absence of optical pumping one obtains,

$$\Delta J(t, u) = -\frac{2}{\eta_0 d} \Delta E(t, u) - \epsilon_0(n^2 - 1) \frac{\partial \Delta E(t, u)}{\partial t} \quad (3.2)$$

Since we collect the data to implement the time shift operation as described in Chapter 2, we obtain the time-shifted change in THz electric field,  $\Delta \tilde{E}(t, u) = \Delta E(t, u - t)$ . So applying the substitution  $u \rightarrow u - t$  to Equation 3.2, we have

$$\Delta \tilde{J}(t, u) = -\frac{2}{\eta_0 d} \Delta \tilde{E}(t, u) - \epsilon_0(n^2 - 1) \frac{\partial \Delta \tilde{E}(t, u)}{\partial t} \quad (3.3)$$

The change of the free-carrier current density,  $\Delta \tilde{J}(t, u) = \Delta J(t, u - t)$ , in the sample can be written approximately as (see Subsection 2.5.2),

$$\Delta \tilde{J}(t, u) \approx E_0(t) \otimes [\Delta \sigma_{\text{DC}}(u - t) j(t)] \quad (3.4)$$

Here,  $\Delta \sigma_{\text{DC}}(t)$  is the change in the DC conductivity and  $j(t)$  is the normalized current impulse response ( $\int_{-\infty}^{\infty} dt j(t) = 1$ ). In the Fourier domain, we define  $\Delta \sigma(\omega, u)$  as  $\Delta \sigma_{\text{DC}}(u) j(\omega)$ . We extract  $\Delta \sigma(\omega, u)$  from  $\Delta \tilde{J}(t, u)$  as described in Subsection 2.5.2.

Figure 3.2 shows the real and imaginary parts of the photoexcited conductivity  $\Delta \sigma(\omega, u)$  measured at four different temperatures in MoS<sub>2</sub>. We find that the measured conductivity spectra closely follow the Drude form,  $\Delta \sigma_{\text{DC}}(u)/(1 - i\omega\tau_{\text{D}})$ , which is the simplest conductivity model in the relaxation time approximation. Therefore, the

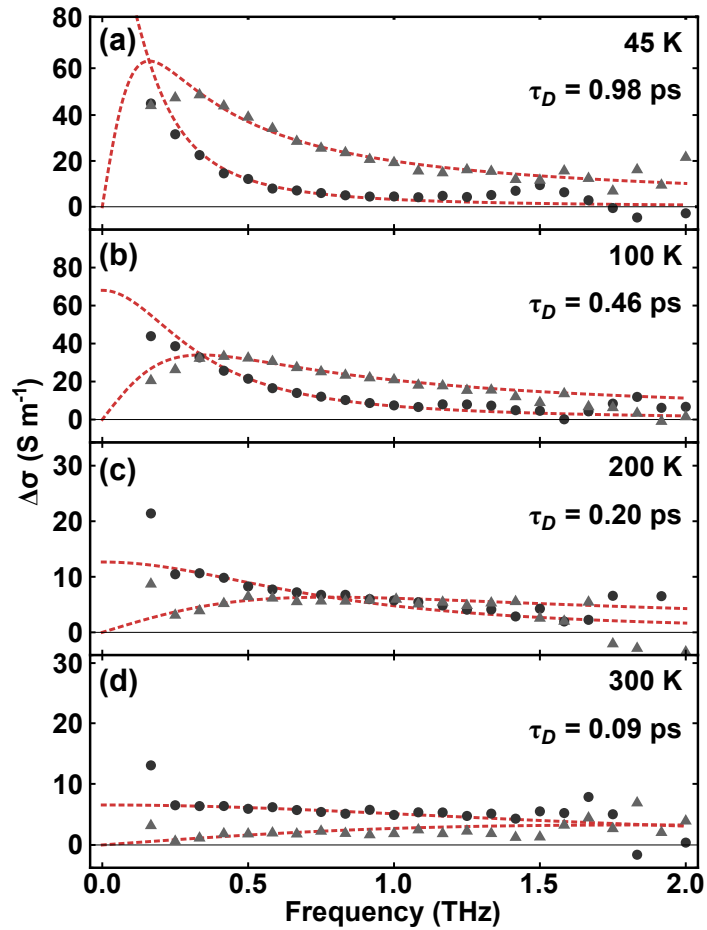


Figure 3.2: THz conductivity. The real (circles) and imaginary (triangles) parts of the measured THz conductivity  $\Delta\sigma(\omega, u)$  plotted versus frequency for various temperatures. In each case, the probe delay is  $u = 5$  ps, and the pump fluence is  $\sim 1.2 \mu\text{J cm}^{-2}$ . (Dashed lines) Drude model fits to the measured conductivity spectra used to extract  $\tau_D$ .

current impulse response  $j(\omega)$  is  $(1 - i\omega\tau_D)^{-1}$ . We fit the real and imaginary parts of the data simultaneously with a weighted least-squares regression and extract the photoexcited DC conductivity  $\Delta\sigma_{DC}(u)$  and the carrier momentum scattering time  $\tau_D$ . Weights were the data variance at each frequency point over twenty scans. The high quality of fits to the data obtained at all temperatures, as shown in Figure 3.2, is strong evidence of the fact that the change in THz transmission we measure indeed originates from the intraband conductivity of the photoexcited carriers. Also, at all temperatures we find no significant variation in the extracted value of  $\tau_D$  for any value of  $u$  in the range  $5 \text{ ps} \leq u \leq 12 \text{ ns}$ . Since one expects very hot carriers to have average momentum scattering times different from that of cold carriers[78], this observation suggests that the carrier distributions after photoexcitation cool down on time scales shorter than a few picoseconds. We further discuss carrier cooling times in Section 4.1.

### 3.1.2 Carrier Mobility and Deformation Potential

Carrier in-plane ( $\perp$  to c-axis) mobility is related to the momentum scattering time by  $\mu = e\tau_D/m_c^*$ , where  $m_c^*$  is the in-plane conductivity effective mass. Multilayer MoS<sub>2</sub> has six electron pockets in the Brillouin zone, each with an anisotropic effective mass tensor[79, 80]. The one hole pocket has an isotropic effective mass tensor. Using DFT values for the electron and hole effective mass tensors[79], we find the conductivity effective masses for both electrons and holes to be  $\sim 0.61m_0$ . In Figure 3.3(a), we plot the electron mobilities corresponding to the measured momentum scattering times at different temperatures ( $T = 30, 45, 100, 200, 300 \text{ K}$ ). We find a mobility of  $257 \text{ cm}^2\text{V}^{-1}\text{s}^{-1}$  at 300 K, increasing to  $4200 \text{ cm}^2\text{V}^{-1}\text{s}^{-1}$  at 30 K. For 300 K, the measured mobility is consistent with recent electronic transport measurements in multilayer MoS<sub>2</sub>[66, 69, 67, 70, 68]. But the mobilities we find below 200 K in this contact-free

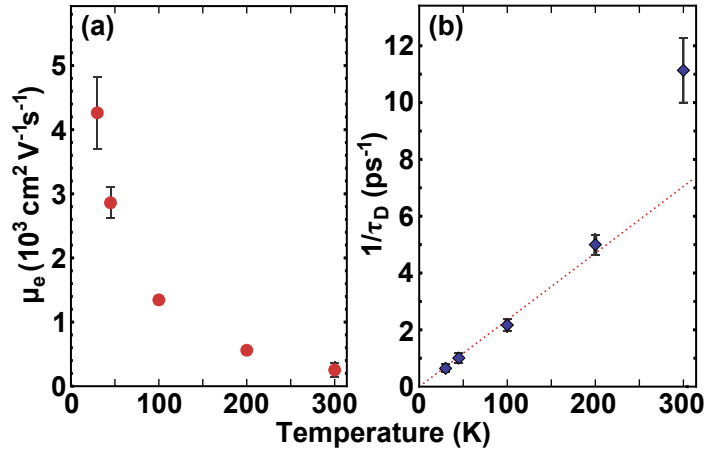


Figure 3.3: Mobility and scattering rate. (a) Electron mobility versus temperature, determined from the measured momentum scattering rate. (b) Measured momentum scattering rate versus temperature with a linear fit for  $T \leq 200$  K. The  $1/\tau_D \propto T$  dependence at low temperatures suggests acoustic phonon scattering as the dominant scattering mechanism. Measured mobility reaches  $\sim 4200 \text{ cm}^2 \text{ V}^{-1} \text{ s}^{-1}$  at 30 K.

measurement are significantly higher than the values previously reported for  $\text{MoS}_2$ .

In Figure 3.3(b), we plot the carrier momentum scattering rate,  $1/\tau_D$ , versus temperature. The scattering rate for  $T \leq 200$  K increases linearly with temperature. This linear temperature dependence is expected for quasi-elastic acoustic phonon scattering in 2D and layered materials in the equipartition regime[68, 81, 73, 74]. Other scattering mechanisms, such as impurity scattering, have a different temperature dependence for layered materials[74]. The larger scattering rate observed at the highest temperature (300 K) likely indicates an optical phonon scattering contribution[73, 69]. In the deformation-potential approximation, the energy-independent acoustic-phonon-limited momentum scattering rate in 2D and layered materials is related to the temperature by[73, 74],

$$\frac{1}{\tau_D} = \frac{m_d^* \Xi^2 k_B T}{\hbar^3 \rho v_s^2} \quad (3.5)$$

where  $\Xi$  is the deformation potential,  $\rho$  is the 2D mass density,  $v_s$  is the LA phonon velocity, and  $m_d^*$  is the carrier density of states effective mass. From the data in Figure 3.3(b), we find  $d\tau_D^{-1}/dT = 22.6 \pm 1.5 \text{ ns}^{-1} \text{ K}^{-1}$  for  $T \leq 200$  K. Using  $v_s =$

$6.7 \times 10^3 \text{ m s}^{-1}$ [73],  $\rho = 3 \times 10^{-6} \text{ kg m}^{-2}$ ,  $m_d^* = 0.62m_0$  (ab-initio values for  $m_d^*$  are almost identical for electrons and holes[79]), we find  $\Xi = 4.2 \text{ eV}$ . This value compares well with previously experimentally and theoretically determined values, generally in the 2-10 eV range, for the deformation potentials in single-layer and multilayer MoS<sub>2</sub>[73, 79, 82, 83, 84].

## 3.2 The Ultimate Limit of Mobility in Molybdenum Disulfide

In this Chapter, we presented measurements of the mobility of photoexcited carriers in multilayer MoS<sub>2</sub> using THz time-domain spectroscopy. The observed temperature dependence of the mobility for  $T \leq 200 \text{ K}$  indicates acoustic phonon scattering as the dominant mobility-limiting mechanism. The measured carrier momentum scattering rates are comparable to theoretical predictions based on phonon-scattering-limited transport[73, 74]. In contrast, previously reported DC electrical measurements have suggested impurity or defect scattering as the dominant mobility-limiting mechanism in multilayer MoS<sub>2</sub>[68, 69, 71, 67]. Given the prevalence of defects and impurities in MoS<sub>2</sub>[57, 64], it is intriguing that we observe mobilities limited by acoustic phonon scattering.

The observed high mobilities at low temperatures in our experiments could be related to the fact that our measurements were performed at very high frequencies. It is well known theoretically and experimentally that AC conductivity in disordered materials increases with the AC frequency[85, 86, 87, 88, 89, 90]. This phenomenon appears in the microscopic models of hopping conduction[85, 86, 87] as well as in the classical models of the AC conductivity in inhomogeneous materials[88, 89, 90]. Since we did not see signatures of AC hopping conduction in our sample at any temperature,

we believe models that describe the AC conductivity in inhomogeneous materials are more relevant to our observations[88, 89, 90]. Accordingly, we believe that the MoS<sub>2</sub> atomic layers in our sample consist of interspersed high and low mobility regions (due to grain boundaries, crystal defects, impurities, etc.[57]) and the conductivity of the layers is determined by the resistive and capacitive couplings of these regions[88, 89, 90]. Even a small fraction of low mobility regions can significantly affect the DC conductivity in lower dimensions. The high mobility regions have a conductivity given by the Drude form. The AC conductivity of the sample is then expected to increase with the frequency until the low mobility regions are capacitively shorted out and the conductivity of the sample is then limited by the Drude conductivity of the high mobility regions. Although this model qualitatively explains the observation of the long momentum scattering times in our experiments, investigation of the frequency dependence of the sample conductivity in the low frequency region ( $< 0.2$  THz) is needed to fully understand the nature of the transport and determine which model, if any, best describes MoS<sub>2</sub>.

# Chapter 4

## Carrier Relaxation in Semiconductors

### 4.1 Carrier Relaxation in Multilayer Molybdenum Disulfide

The time-domain nature of the optical-pump THz-probe measurement of MoS<sub>2</sub>, described in Chapter 3, allows us to naturally access information about carrier dynamics in the material. By varying the time delay between the optical pump and THz probe, we track the temporal development of the intraband conductivity, which reveals carrier intraband and interband relaxation dynamics. Carrier scattering and relaxation rates, which determine the performance of many proposed and demonstrated electronic and optoelectronic metal dichalcogenide devices, remain poorly understood. Our measurements reveal picosecond cooling times varying from  $\sim 0.7$  ps at 300 K to  $\sim 1.2$  ps at 45 K. Subsequent density-dependent recombination of carriers occurs over 10's of nanoseconds at low temperature. We present a recombination model based on carrier capture into defect states which reproduces the measured nonlinearity of this

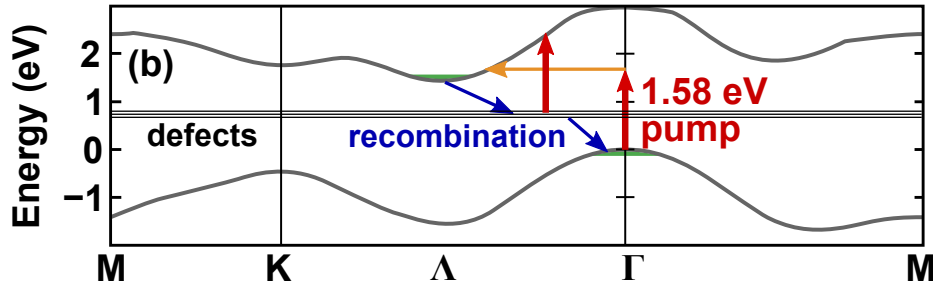


Figure 4.1: In-plane bandstructure of multilayer MoS<sub>2</sub> depicting carrier photoexcitation and recombination.

recombination versus carrier density as well as the observed temporal dynamics.

Much of the material presented in this Section appears in Ref. [76] and was a collaboration between myself, Parinita Nene, and Farhan Rana.

Figure 4.1 depicts the experimental scenario. Optical pump pulses excite electron and hole distributions at the six  $\Lambda$  points and the  $\Gamma$  point in MoS<sub>2</sub>, respectively, as well as from defect states, after which the distributions cool and recombine. As we discuss below, this recombination occurs via a defect-assisted process. Experimental details are presented in Section 3.1.

### 4.1.1 Carrier Dynamics on Short Time Scales

Knowing the normalized current impulse response,  $j(\omega)$ , and the frequency-dependent photoexcited conductivity,  $\Delta\sigma(\omega, u)$ , we determine the photoexcited DC conductivity,  $\Delta\sigma_{\text{DC}}(u)$ . The temporal resolution in our experiments is set by the measurement bandwidth of  $\Delta\sigma(\omega, u)$ ,  $\sim 1.8$  THz, and is approximately  $(2 \times 1.8 \text{ THz})^{-1} = 0.28$  ps (see Section 2.5.3). Since the in-plane conductivity effective masses for electrons and holes are approximately the same in multilayer MoS<sub>2</sub>[79], one can write the DC conductivity as  $\sigma_{\text{DC}} = Ne^2\tau_{\text{D}}/m_c^*$ , where  $N$  is the total mobile carrier density and equals the sum of the mobile electron density,  $n$ , and the mobile hole density,  $p$ . The change in the carrier density  $\Delta N$  can be determined from the measurement of  $\Delta\sigma_{\text{DC}}$ .

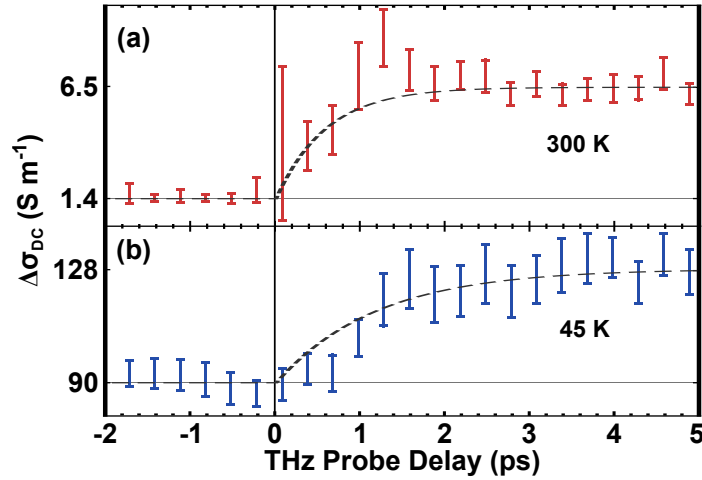


Figure 4.2: Intraband relaxation. The change in DC conductivity,  $\Delta\sigma_{\text{DC}}(u)$ , versus pump-probe delay on short time scales ( $-2 \leq u \leq 5$  ps). We show data for two representative temperatures ((a) 300 K and (b) 45 K), each with a pump fluence of  $\sim 1.2 \mu\text{J cm}^{-2}$ . Immediately after the pump pulse, the conductivity increases, reaching its maximum value within 5 ps at all temperatures. The rise time is slower at 45 K than at 300 K.

Figure 4.2 shows the measured change in the conductivity  $\Delta\sigma_{\text{DC}}(u)$  on short time scales ( $-2 \leq u \leq 5$  ps) for two different representative temperatures. The pump fluence in each case is  $\sim 1.2 \mu\text{J}/\text{cm}^2$ . Immediately after photoexcitation ( $u = 0$ ), the conductivity increases, reaching its maximum value within 5 ps at all temperatures. The error-range displayed for each data point represents a 95% confidence interval for the fitting parameter  $\Delta\sigma_{\text{DC}}(u)$ . The dashed lines superimposed on the data represent fittings using exponential curves with 0.7 ps and 1.2 ps time constants at 300 K and 45 K, respectively. Our data suggests that the conductivity reaches its peak value faster at higher temperatures. As we discuss below, we attribute these short-time-scale dynamics to picosecond cooling of the electron and hole distributions.

As depicted in Figure 4.1, the 1.58 eV pump photons excite electrons from the valence band maximum at the  $\Gamma$  point to the conduction band minima at the  $\Lambda$  point by a phonon-assisted (or impurity-assisted) indirect absorption process. Since the indirect bandgap in multilayer  $\text{MoS}_2$  is around 1.29 eV[51, 82], the photoexcited

electrons and holes are at an elevated temperature compared to the lattice immediately after photoexcitation and thermalization[78, 91]. If the photon energy in excess of the indirect bandgap contributes to the kinetic energy of the carriers, we estimate the carrier temperature immediately after photoexcitation to be around 1100 K. At this high temperature, the electron and hole distributions would be spread out in energy, with fast momentum scattering rates and reduced mobility due to optical phonons[73, 92]. As the carrier distributions relax towards the band extrema and cool via optical phonon emission, the carrier momentum scattering rates decrease and the conductivity increases. The rise in the conductivity following photoexcitation observed in our experiments is therefore indicative of carrier cooling. The slower cooling observed at lower lattice temperatures can be attributed to a number of factors. For example, the carrier cooling rates due to optical phonon emission are proportional to  $n_B + 1$ , where  $n_B$ , the Bose occupation factor for phonons, is approximately 20% larger at 300 K compared to 45 K. In addition, the heat capacity of optical phonons is around three orders of magnitude larger at 300 K compared to 45 K and, therefore, carrier cooling bottleneck due to the generation of hot phonons is much reduced at higher lattice temperatures[91].

### 4.1.2 Carrier Dynamics on Long Time Scales

Figure 4.3(a) shows the change in the mobile carrier density  $\Delta N(u)$  at 45 K for various pump fluences, determined from measured  $\Delta\sigma_{\text{DC}}(u)$  on long time scales ( $-20 \leq u \leq 400$  ps). As expected, the carrier density decays after reaching a peak value in the first few picoseconds after photoexcitation. We attribute this relaxation to carrier trapping and recombination by defects. The carrier density decay rate is relatively fast in the first  $\sim 100$  ps after photoexcitation, after which the decay occurs on much longer time scales. The maximum probe delay allowed by our setup, 400 ps, is unable

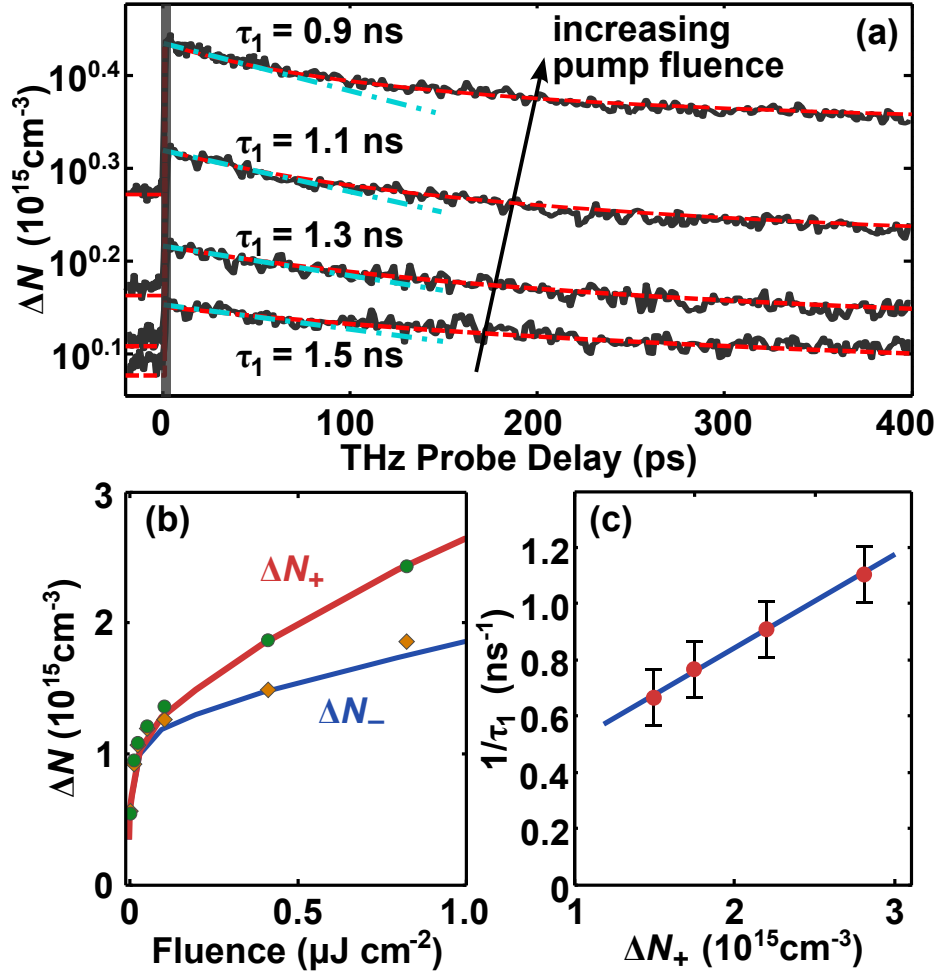


Figure 4.3: Density-dependent recombination. (a) (Solid) The measured change in the carrier density  $\Delta N(u)$  plotted on a log scale as a function of probe delay. Shown are transients for four pump fluences ( $0.2$ ,  $0.4$ ,  $0.8$ , and  $1.2 \mu\text{J cm}^{-2}$ ) at  $45 \text{ K}$ . (Blue dot-dash) Initial exponential relaxation corresponding to the estimated  $\tau_1$ . (Red dash) Full transient simulations using Equations 4.5. (b) Measured  $\Delta N_+ = \Delta N(u = 0^+)$  (circles) and  $\Delta N_- = \Delta N(u = 0^-)$  (diamonds) versus pump fluence at  $45 \text{ K}$ . (Solid) Curves obtained from simulations of Equations 4.5. (c) The measured inverse decay time  $1/\tau_1$  at  $45 \text{ K}$  versus  $\Delta N_+$ . The slope of the line estimates the electron capture rate  $An_d$ .

to resolve these long time scales. But the non-zero carrier densities observed at negative probe delays show that the photoexcited carrier density does not completely decay in the time interval, around 12.3 ns, between two successive optical pulses. The carrier densities immediately before and after photoexcitation, as a function of pump fluence, reveal the carrier density dependence of the long term ( $>100$  ps) recombination rates. Figure 4.3(b) shows the change in carrier density immediately before,  $\Delta N_- = \Delta N(u = 0^-)$ , and after,  $\Delta N_+ = \Delta N(u = 0^+)$ , photoexcitation. Both  $\Delta N_-$  and  $\Delta N_+$  increase with the pump fluence in a nonlinear fashion, so carrier-density-independent recombination times can be ruled out. We also estimate the initial recombination rate,  $1/\tau_1$ , versus pump fluence from the slope of the blue dash-dot lines in Figure 4.3(a). Figure 4.3(c) shows that  $1/\tau_1$  increases approximately linearly with  $\Delta N_+$ . Any physical model that describes the observed carrier dynamics must account for the transition from the fast decay rates in the first  $\sim 100$  ps to the slow decay rates thereafter. In addition, the model must account for the severe nonlinearity of  $\Delta N_-$  and  $\Delta N_+$  versus pump fluence.

### 4.1.3 MoS<sub>2</sub> Recombination Model

Here, we present a model of carrier relaxation based on trapping and recombination by optically-active defect states. This model explains all features of the observed carrier dynamics at 45 K. The natural MoS<sub>2</sub> used in our work is known to have defects such as vacancies, grain boundaries, and impurities[57, 64]. Many of these defects are optically active in the near-IR wavelength region and appear in the optical absorption spectra[93, 94, 95]. We assume that the initial fast decay of the photoexcited carrier density is due to the capture of electrons by defect states in the band gap[96] (see Figure 4.1). As these defect states become full of electrons, the decay rate decreases (due to Pauli blocking) and becomes limited by the capture of photoexcited holes

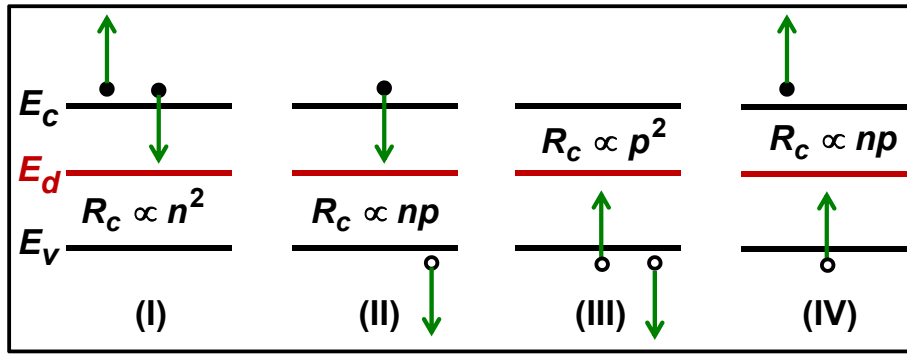


Figure 4.4: The four basic Auger processes for the capture of electrons and holes at defect states are illustrated. The energies of the conduction band bottom, valence band top, and the defect levels are  $E_c$ ,  $E_v$ , and  $E_{rmd}$ , respectively. In each case, the approximate carrier density dependence of the capture rates are indicated[97].

from the valence band. The optical pump pulse excites electrons to the conduction band from both the valence band and also the defect states, and we assume that the defect states become empty immediately after the pump pulse[94, 95]. Our final assumption is that the defect states are assumed to be occupied by electrons in thermal equilibrium in our n-doped sample.

There are essentially two main mechanisms for the capture/emission of electrons and holes at/from localized crystal defects[97]: (1) Phonon-assisted processes, and (2) Auger processes. Phonon-assisted processes can be single-phonon processes or multi-phonon processes, including phonon-cascade processes[98]. In phonon-assisted processes the capture rates (units:  $\text{cm}^{-3}\text{s}^{-1}$ ), tend to go linearly with the carrier density (i.e. the capture times are independent of the carrier density). The capture times observed in our experiments are carrier density dependent (inverse electron capture times increase linearly with the electron density), as shown in Figure 4.3. In contrast to phonon processes, the capture times in Auger processes are carrier density dependent. Figure 4.4 shows the four basic Auger processes for the capture of electrons ((I) and (II)) and holes ((III) and (IV)) at defects. The corresponding emission processes are the simply the inverse of the capture processes.

The rate equations for each Auger process (and its inverse) can be written using Figure 4.4. For example, the electron density rate equation for process (I) and its inverse is,

$$\frac{dn}{dt} = -An_d n^2(1 - f_d) + An_d n n^* f_d \quad (4.1)$$

Here,  $n$  is the electron density,  $A$  is the rate constant for electron capture by the defect state,  $n_d$  is the defect density, and  $f_d$  is the occupation of the defect state. The first term describes the capture process and the second term describes the emission process. The value of the constant  $n^*$  can be determined by using the fact that in thermal equilibrium  $dn/dt = 0$ :

$$n^* = n_0 \frac{1 - f_{d0}}{f_{d0}} \quad (4.2)$$

where  $n_0$  is the equilibrium electron density and  $f_{d0}$  is the equilibrium defect occupation. If in equilibrium  $f_{d0} \approx 1$ , as is expected for defects deeper than a few  $k_B T$  in an n-doped material, then  $n^*$  can be assumed to be negligibly small and electron generation from the defect states can be ignored in the above equation. Process (I) and process (II) can have comparable magnitudes[97]. So, ignoring emission processes, the rate equation for the electron density becomes,

$$\frac{dn}{dt} = -An_d n^2(1 - f_d) - Cn_d n p(1 - f_d) \quad (4.3)$$

where  $p$  is the hole density, while  $A$  and  $C$  are the rate constants for electron capture by the defect state corresponding to processes (I) and (II) in Figure 4.4, respectively.

In our experiments, since our MoS<sub>2</sub> sample is n-doped, the first term of the right hand side is more important for small pump fluence values (when the hole density is small) compared to the second term. For large pump fluence values, both the electron and the hole densities can become comparable and the second term on the right hand

side may not be ignored. However, at large pump fluences the effect of the second term is indistinguishable from the first term in our pump-probe experiments (since both terms would result in the inverse electron capture time to increase linearly with the photoexcited carrier density). Since the pump fluences used in our experiments are relatively small (and the maximum photoexcited carrier density is in the low  $10^{15}$   $\text{cm}^{-3}$ ), we have chosen to ignore the second term, corresponding to process (II), in the above Equation for simplicity. Similarly, ignoring emission processes, the rate equation for the hole density becomes,

$$\frac{dp}{dt} = -Bn_{\text{d}}npf_{\text{d}} - Dn_{\text{d}}p^2f_{\text{d}} \quad (4.4)$$

Here,  $p$  is the hole density.  $D$  and  $B$  are the rate constants for hole capture by the defect state corresponding to processes (III) and (IV) in Figure 4.4, respectively. Again, since our  $\text{MoS}_2$  sample is n-doped and the pump fluences used in our experiments are small, we have chosen to ignore the second term, corresponding to process (IV), in the above Equation for simplicity.

Together, the rate equations for the decay of the electron and hole densities in our model for recombination in  $\text{MoS}_2$  are,

$$\begin{aligned} \frac{dn}{dt} &= -An_{\text{d}}n^2(1 - f_{\text{d}}) \\ \frac{dp}{dt} &= -Bn_{\text{d}}npf_{\text{d}} \\ \frac{df_{\text{d}}}{dt} &= An^2(1 - f_{\text{d}}) - Bnpf_{\text{d}} \end{aligned} \quad (4.5)$$

The value  $n$  is the sum of the equilibrium electron density,  $n_0$ , and the excess photoexcited electron density. We varied the values of the fitting parameters  $A$ ,  $B$ ,  $n_{\text{t}}$ , and  $n_0$  in simulations to fit the data in Figures 4.3(a) and 4.3(b). The simulations involved time-stepping the rate equations over many ( $1-5 \times 10^3$ ) pump pulse cycles

until a steady state was achieved. The difference  $\Delta N_+ - \Delta N_- \approx 0.52 \times 10^{15} \text{ cm}^{-3}$  per  $\mu\text{J cm}^{-2}$  determined the mobile carrier density created by the pump pulse in our simulations.

The data in Figure 4.3 can inform the search for appropriate values of the fitting parameters. Immediately after photoexcitation, since  $n$  varies as  $\Delta N_+/2$ , the slope of the line in Figure 4.3(c) estimates the product  $An_d$ . Since the long term decay of the photoexcited density is limited by the capture of holes in defects, the values of  $\Delta N_-$  estimate the product  $Bn_d$ . Finally, the density of defect states governs how quickly they fill with electrons, therefore  $n_d$  is determined from the time at which the initial fast decay transitions to the slower decay, as measured in Figure 4.3(a). The values of fitting parameters that best fit the data are:  $A = 2.6 \times 10^{-21} \text{ cm}^6 \text{ s}^{-1}$ ,  $B = 2.1 \times 10^{-23} \text{ cm}^6 \text{ s}^{-1}$ ,  $n_d = 5.0 \times 10^{14} \text{ cm}^{-3}$ , and  $n_0 = 2.7 \times 10^{14} \text{ cm}^{-3}$ . This value of  $n_0$  corresponds to a DC conductivity of  $12 \text{ S m}^{-1}$ , which compares well with the value of conductivity obtained from THz transmission measurements of the unpumped sample,  $\sigma_0 = 10 - 20 \text{ S m}^{-1}$ . The model presented here closely agrees with the data for 45 K, accurately reproducing the values of  $\Delta N_-$ , the relaxation curves, and the nonlinearity of  $\Delta N$  versus pump fluence.

#### 4.1.4 Discussion

Carrier relaxation and recombination dynamics directly affect the performance of almost all electronic and optoelectronic devices. We have observed several time scales in the dynamics associated with carrier relaxation and recombination in MoS<sub>2</sub>. The initial intraband relaxation (or carrier cooling) occurs within 5 ps. Carrier interband recombination appears to result from carrier trapping in optically active defect states, with recombination lasting over tens of nanoseconds at low temperature due to slow hole capture in the defect states. It is important to mention that simple bimolecular

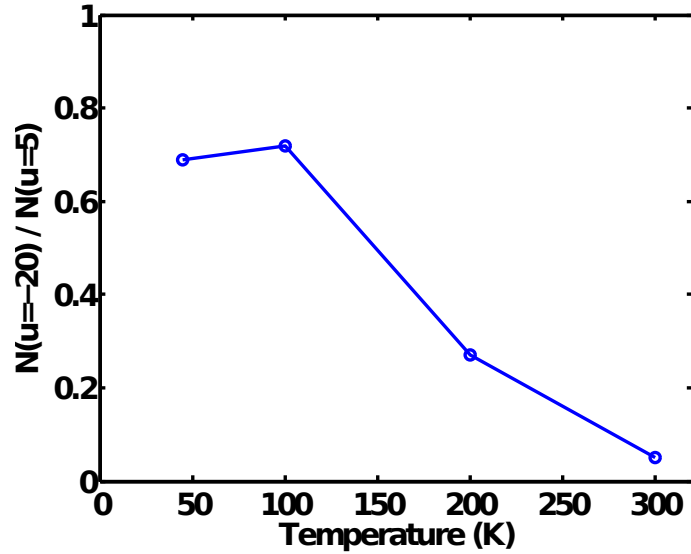


Figure 4.5: The ratio of carrier density extracted for  $u = 5$  ps to  $u = -20$  ps. 70% of photoexcited carriers remain after 12 ns at low temperature, but at room temperature only 5% remain.

recombination (proportional to  $n^2$ ) and direct interband Auger recombination (proportional to  $n^3$ ) are not sufficiently nonlinear to account for the density dependence seen in Figure 4.3(b). Although our data shows that the recombination times in multilayer MoS<sub>2</sub> are long, they are short in comparison with other indirect band gap semiconductors, such as high-quality Si or Ge, which have recombination times in excess of one microsecond at room temperature[99]. We note here that our measurements might not have detected charge trapping dynamics occurring on much longer time scales ( $\gg 10$  ns) recently observed in MoS<sub>2</sub> photoconductive devices[100].

The model we presented accounts for the features observed in the data at 45 K, but we did not include temperature dependence. Figure 4.5 shows the ratio of photoexcited carriers remaining after 12 nanoseconds have elapsed, as a function of temperature. There is a clear decreasing trend as temperature increases above 100 K, showing that recombination occurs more quickly at higher temperatures. So a more complete model of carrier relaxation would most likely include a temperature dependence of the recombination parameters  $A$  and  $B$ .

## 4.2 Carrier Relaxation in Germanium Nanowires

During the last ten years or so, semiconductor nanowires have gathered much interest in the electronics and optoelectronics communities. Nanowires have been applied to an array of applications that highlight their versatility as building blocks of integrated electronics (transistors) and photonics (waveguides, lasers, photodetectors, solar cells) [101, 102, 103, 104, 105, 106]. Germanium nanowires are of particular interest due to the attractive material properties of Germanium, including large electron and hole mobilities and large optical absorption in the visible/near-IR. These properties could make Germanium nanowires the choice for next generation electrical and photonic devices, such as transistors, CMOS compatible photodetectors, and solar cells. Understanding the fast electrical and optical response as well as ultrafast dynamics of carriers in nanowires is important for most of the applications mentioned here. In this Section, we present results on the measurement of the terahertz (THz) response as well as ultrafast carrier dynamics in photoexcited Germanium nanowires using optical-pump THz-probe spectroscopy. In Chapter 5, we discuss how charge confinement determines the polarization-dependent THz response of the material.

Ultrafast carrier dynamics in group III-V, II-VI, and group IV semiconductor nanowires have been studied with optical-pump optical-probe spectroscopy measurements [107, 108], which are sensitive primarily to the carrier occupation of specific regions in the energy bands. Optical-pump THz-probe spectroscopy, in which the probe photon energy is  $\sim 5$  meV, is sensitive to not only the total carrier density but also to the distribution of these carriers in energy within the bands. The latter is true since the energy distribution of carriers affects the THz optical conductivity through

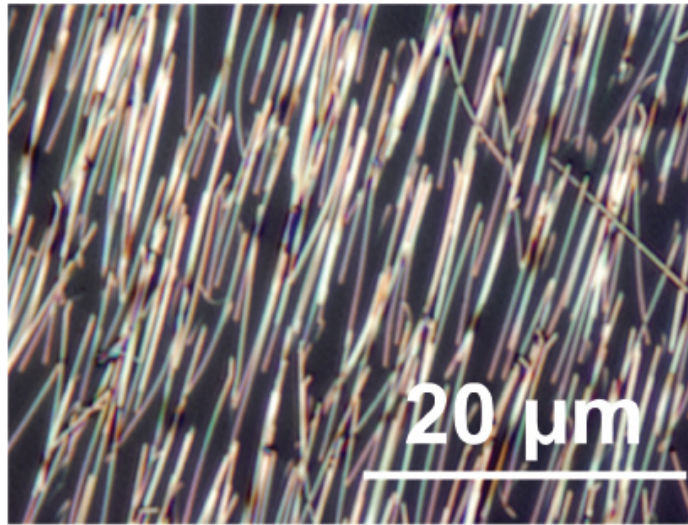


Figure 4.6: Dark-field optical micrograph of oriented 80 nm diameter Germanium nanowires placed flat on a quartz substrate (100X, NA 0.9 objective). Note: Nanowires appear wider than 80 nm due to diffraction.

the mobility [78, 109]. Optical-pump THz-probe spectroscopy can therefore be used to simultaneously study both intraband relaxation and interband recombination dynamics of photoexcited electrons and holes on ultrafast time scales. Our results show intraband carrier relaxation rates (attributed to intravalley and intervalley phonon scattering) in the 1.5-2 ps range and carrier density-dependent recombination rates (attributed to nanowire surface defects) in the 75-125 ps range at room temperature in 80 nm diameter wires.

Much of the material presented in this Section appears in Ref. [110] and was a collaboration between myself, Paul A. George, Mark Levendorf, Martin Blood-Forsythe, Jiwoong Park, and Farhan Rana.

### 4.2.1 Experiment

Germanium nanowires used in this work were  $\sim 80$  nm in diameter and  $\sim 10$   $\mu\text{m}$  in length (see Figure 4.6). They were grown via CVD in a hot-walled quartz tube furnace using Germane as the source gas and gold nanoparticles for the catalyst [111].

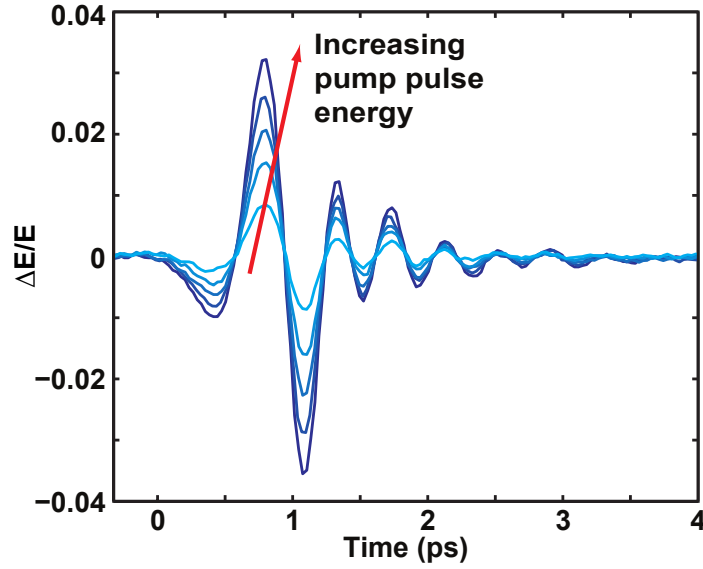


Figure 4.7: The measured differential amplitudes of THz pulses transmitted through photoexcited Germanium nanowires for pump pulse energies of 10.2, 8.2, 6.1, 4.1, and 2.0 nJ are shown for a fixed pump-probe delay. For this data, we choose the THz field polarized parallel to the nanowires, and we scaled the differential amplitudes by the peak amplitude of the transmitted THz pulse in the absence of photoexcitation.

Germanium nanowires produced with this method are known to grow predominantly in the  $\langle 111 \rangle$  direction [112]. Alignment of nanowires was achieved on quartz crystal substrates using a contact printing method previously reported by Fan *et al.*[113]. Nanowires used in this experiment were not intentionally doped, and expected initial carrier density is less than  $10^{17}$   $1/\text{cm}^3$ . We performed optical-pump THz-probe measurements of the carrier dynamics in the Ge nanowire films using a THz time-domain spectrometer, as described in Chapter 2. This configuration of spectrometer used electro-optic detection of the THz pulse via the Pockels Effect in a ZnTe crystal [114]. We also employ a wire-grid polarizer between the sample and the THz detector. Pump pulse energies were in the range of 1–12 nJ. Measurements in this work were performed at 300 K.

Figure 4.7 shows the measured differential amplitudes of THz pulses transmitted through photoexcited Germanium nanowires for pump pulse energies of 10.2, 8.2, 6.1,

4.1, and 2.0 nJ with a fixed pump-THz sampling delay (see Section 2.5). The THz field is polarized parallel to the nanowires. Since we employ double-chopping, the measured differential signal is affected only by the THz response of the photoexcited carriers within the nanowires. Figure 4.7 displays no measurable carrier density dependence in the frequency dispersion of the THz response since the measured pulse shape remains unchanged for different pump pulse energies (i.e. only the pulse amplitude changes). As discussed in Section 5.1, the carrier-density-independent dispersion is a result of very small plasmon resonance frequencies for parallel polarized THz radiation. These results show that the dynamics of photoexcited carriers can be studied by measuring the differential amplitude of the peak of the transmitted THz pulse as a function of the pump-probe delay [38] (see Section 2.5.2).

### 4.2.2 Discussion

Figure 4.8 shows the measured differential amplitude of the peak of the THz probe pulse as a function of the pump-probe delay for different optical pump energies. The THz transmission decreases in the first  $\sim 5$  ps following the optical excitation and then recovers on a 75–125 ps time scale. These two time scales in the measured transient can be explained by the intraband and interband carrier dynamics, respectively. The optical pulse creates electron-hole pairs near the  $\Gamma$ -point in the Germanium reciprocal lattice (see Figure 4.9). Electrons quickly scatter from the  $\Gamma$ -point to the X-point within 100 fs due to strong intervalley phonon scattering, after which they scatter to the lowest L-valley within a few picoseconds [115]. Photoexcited holes in the three valence bands are also expected to thermalize within 0.5 ps [115] and cool due to optical phonon emission within a few picoseconds [116]. Higher electron mobility in the L-valley and the high hole mobility at the top of the light hole band, increases the THz optical conductivity. So as the photoexcited carriers relax, the transmission

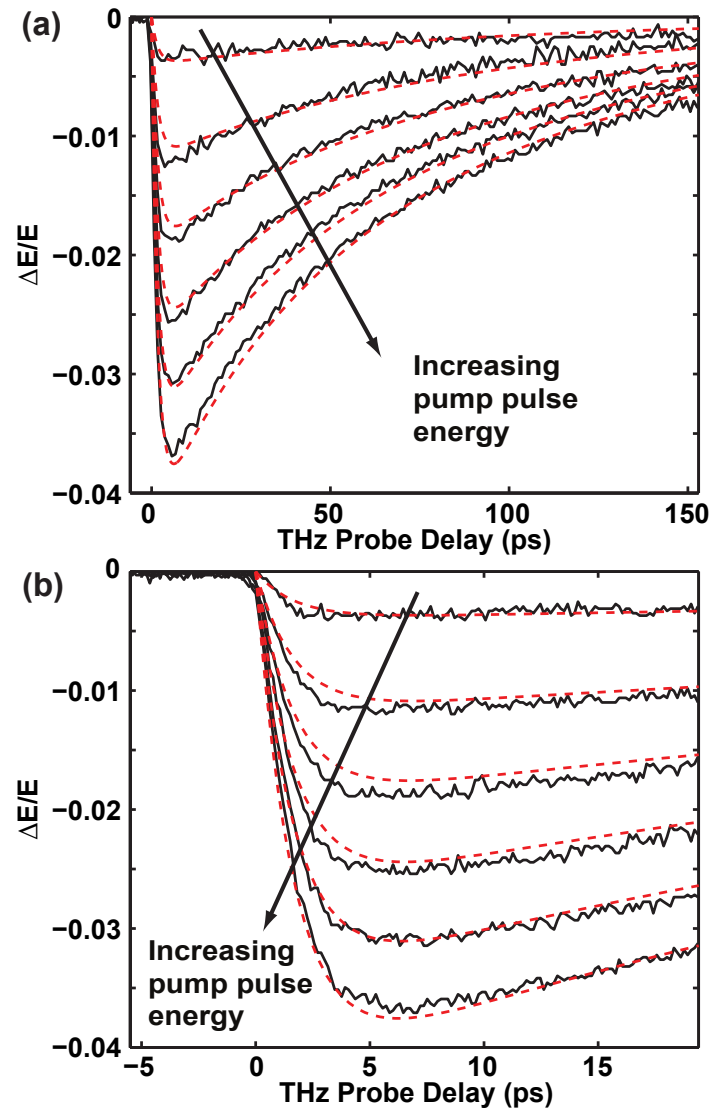


Figure 4.8: (a) Measured (solid lines) normalized differential amplitude  $\Delta E/E$  of the peak of the THz probe pulse is shown as a function of the pump-probe delay for optical pump energies of 12 nJ, 9.8 nJ, 7.6 nJ, 5.4 nJ, 3.3 nJ, and 1.1 nJ. We also show a computed fit (dashed lines) based on Equations 4.6 and 4.7. THz probe transmission recovers on a 75-125 ps time scale. (b) Close-up of the differential transmission transient.

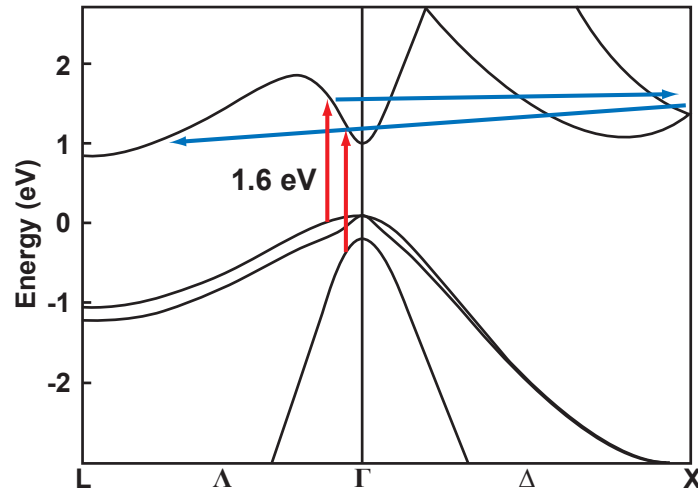


Figure 4.9: Ultrafast dynamics of photoexcited carriers in a Germanium nanowire energy band are depicted [115]. Electrons are photoexcited near the  $\Gamma$  point and quickly scatter to the X-point. In the next few picoseconds, electrons scatter to the L-valley, where they remain until they recombine. Holes remain at the  $\Gamma$  point.

of the incident THz radiation decreases. The transmission of the THz radiation then recovers on a slower time scale as the hole and the electron densities decrease due to recombination.

Using a simple model based on rate equations discussed below, we have fit the measured transients, and these fits are also shown in Figure 4.8. A characteristic time scale of 1.7 ps is extracted for the initial transmission decrease. Since the experiment is sensitive to the total conductivity of both electrons and holes, this value of 1.7 ps corresponds to an average intraband relaxation time associated with hole cooling and electron scattering from the X-point to the L-point. The measured relaxation time is consistent with the calculated rates and previously reported measurement results [107, 117, 116].

In bulk Germanium, carrier recombination rates are highly dependent on the doping density. Recombination times as long as hundreds of microseconds for undoped Germanium [99] and as short as hundreds of picoseconds for doped Germanium [117] have been reported. Our measurements show that electrons and holes in 80 nm

Germanium nanowires recombine with carrier density-dependent recombination times between 75-125 ps. This shorter time scale, compared to that in bulk Germanium, indicates that surface defect states may be responsible for faster recombination in agreement with recent electrical and optical pump-probe measurements [107, 118].

As seen in the micrograph of Figure 4.6, the nanowire film is essentially one nanowire (80 nm) thick. So to analyze the THz transmission, we use the formula for a two-dimensional thin conducting film in Equation 2.8, discussed in detail for Ge nanowires in Section . Following Equation 2.8, since the conductivity of the film is small, the differential THz transmission is approximately proportional to the carrier density. In order to describe the complete differential THz transmission transient shown in Figure 4.8, we model the time dependence of the photoexcited carrier densities in the Germanium nanowires with rate equations. Since the differential transmission measured in our experiments depends on the total conductivity of both electrons and holes, and, as mentioned earlier, the time scales associated with the intraband relaxation dynamics of both electrons and holes are expected to be nearly the same, we model both the electron and the hole dynamics with the same rate equations. We assume that the photoexcited electron and hole density at higher energies,  $N'$ , relaxes with a characteristic time  $\tau_r$ . The density of the cool electrons and holes at the L- and  $\Gamma$ -valleys, respectively, is  $N$ . We assume that only the high mobility cool electron and hole populations interact with the THz radiation until they recombine [115]. Recombination in bulk Germanium with low doping is generally attributed to the Shockley-Reed-Hall (SRH) mechanism of defect assisted recombination. Auger recombination becomes dominant for doping densities above  $10^{18} \text{ cm}^{-3}$  [99]. Surface defect recombination in nanowires is also expected to have carrier density dependence similar to that of the bulk SRH mechanism. We assume that the recombination rate is described by a second-order polynomial in the electron and hole density  $N$ . The

rate equations for the carrier density is,

$$\frac{dN'}{dt} = -\frac{N'}{\tau_r} \quad (4.6)$$

$$\frac{dN}{dt} = \frac{N'}{\tau_r} - (A N + B N^2) \quad (4.7)$$

The initial photoexcited density  $N'(t = 0)$  is estimated to be  $4.5 \times 10^{18}$  1/cm<sup>3</sup> for a 12 nJ pump pulse and is assumed to scale linearly with the pump pulse energy. The DC conductivity  $\sigma_o$  equals  $(\mu_e + \mu_h)eN$ , where  $\mu_e$  and  $\mu_h$  are the electron and hole mobilities. Agreement between the rate equation model and the data is shown in Figure 4.8, where the extracted values of the various parameters for best fit are as follows:  $\tau_r = 1.7$  ps,  $A = 8.8 \times 10^9$  1/sec, and  $B = 2 \times 10^{-9}$  cm<sup>3</sup>/sec. This model agrees with the data for all pulse energies. The necessity of the  $B$  parameter indicates carrier density-dependent recombination rates in Germanium nanowires, which is consistent with density-dependent SRH surface and Auger recombination [119].

These results provide a useful data point with which to assess Germanium nanowires for use as electronic and optoelectronic devices [101, 102, 103, 104, 105, 106]. In comparison to Aluminum catalyzed Si nanowires with similar diameter, the Ge nanowires used in this study have a smaller lifetime, by a factor of  $\sim 3$  [120]. This would suggest that the Si nanowires would be better for devices relying, for example, on minority carrier transport. On the other hand, the Ge nanowires would be better suited for fast-switching devices relying on a short-lived carrier density. In any case, it is clear that the growth process and diameter are important for determining the recombination parameters since recombination is likely determined by defect scattering.

### 4.3 Carrier Cooling in Graphene

In recent years, graphene has gathered much interest for electrical and optical applications due to its unusual band structure and properties [121, 122]. Graphene has been involved in an array of applications that highlight its versatility and novelty as a platform for electronic, plasmonic, optical/IR, and terahertz devices [123, 124, 125, 126, 127, 128]. Realization of many of the graphene based devices relies on a good understanding of the nonequilibrium carrier and phonon processes and their associated time scales. In particular, the dynamics associated with the cooling and recombination of photoexcited carriers are of interest in demonstrated and proposed graphene optoelectronic and terahertz devices [125, 126, 127].

Relaxation dynamics of photoexcited carriers in graphene have recently been studied using ultrafast optical/IR pump-probe spectroscopy by several groups including the authors [129, 130, 131, 132, 133, 134, 135, 136]. These measurements, which typically measure the relaxation of the high energy tail of the carrier distribution, have shown that the photoexcited carriers thermalize within few tens of femtoseconds to generate a hot carrier distribution. This hot distribution then cools rapidly via optical phonon emission on a time scale of hundreds of femtoseconds. Within one picosecond, the carrier and the optical phonon temperatures equilibrate, and carrier cooling slows. At this point, cooling is limited by the exchange of energy between the carriers and the optical phonons and the subsequent anharmonic decay of optical phonons into acoustic phonons. The questions that still remain unanswered pertain to the nature of the relaxation dynamics over much longer time scales and to the role played by carrier generation and recombination processes in the observed relaxation

dynamics. The answer to these questions is interesting both from the perspective of practical devices and also from a theoretical point of view. For example, theoretical groups have recently pointed out that the cooling of hot carriers in doped graphene is very slow when a majority of the carrier distribution is below the optical phonon energy. In this case, carrier cooling can occur only via acoustic phonon emission [137, 138]. Compared to other semiconductors, graphene stands out due to its rather large optical phonon energies ( $\sim 0.196$  eV and  $0.162$  eV). Therefore, the optical phonon energy bottleneck in carrier cooling is expected to play an important role in many graphene-based electronic and optical devices [125, 127, 128]. In this Section, we report observations of this bottleneck in the cooling of photoexcited carriers.

Ultrafast terahertz spectroscopy is a useful tool to study the relaxation dynamics of the low energy carriers near the Dirac point. Previous studies of graphene using optical-pump terahertz-probe spectroscopy, carried out at room temperature by the authors [109] and others [139], attributed the observed relaxation transient occurring over a 1–10 ps time scale to carrier recombination. However, recent theoretical results reported by the authors and others show that the interband recombination and generation mechanisms in graphene, such as Auger scattering and impact ionization [140, 141], optical phonon scattering [142], and plasmon scattering [143], can have characteristic times much shorter than one picosecond. In particular, plasmon scattering can be extremely fast, with time scales on the order of a few hundred femtoseconds [143]. In this paper, we present results from optical-pump terahertz-probe spectroscopy of photoexcited carriers in graphene at different temperatures. We vary the temperature in order to better understand the role played by several scattering processes in the observed relaxation transients. Our results show that the tails of the relaxation transients, as measured by the differential probe transmission, become remarkably slow at low temperatures. They extend well beyond several hundred

picoseconds at temperatures below 50 K.

We also present a theoretical model to explain the measured data. Our model includes intraband carrier scattering from optical and acoustic phonons as well as interband carrier recombination and generation from optical phonons, plasmons, Auger scattering, and impact ionization. Our model shows that the photoexcited electrons and holes equilibrate with each other within one picosecond due to the very fast recombination and generation processes. This fast equilibration causes the electron and hole Fermi levels to merge. The experimentally observed relaxation transients beyond a few picoseconds are then due entirely to the cooling of the carriers. We attribute the very slow tails of the relaxation transients observed at low temperatures to the bulk of the carrier energy distributions moving close enough to the Dirac point such that both intraband and interband scattering of carriers via optical phonon emission become inefficient. For completely undoped samples, with symmetric electron and holes distributions, this occurs when the bulk of the electron and hole distributions move below half the optical phonon energy. Our results compliment the earlier theoretical predictions [137, 138], and our model agrees very well with our measurements at all temperatures.

Much of the material presented in this Section appears in Ref. [144] and was a collaboration between myself, Haining Wang, Shriram Shivaraman, Virgil Shields, Michael Spencer, and Farhan Rana.

### 4.3.1 Experiment

Graphene samples used in this work were grown epitaxially via thermal decomposition of the SI-SiC (000 $\bar{1}$ ) surface [145]. Despite the several-layer thicknesses of these large area samples, layers are electrically decoupled such that they behave as a collection of individual graphene sheets [145]. The samples were characterized with Raman

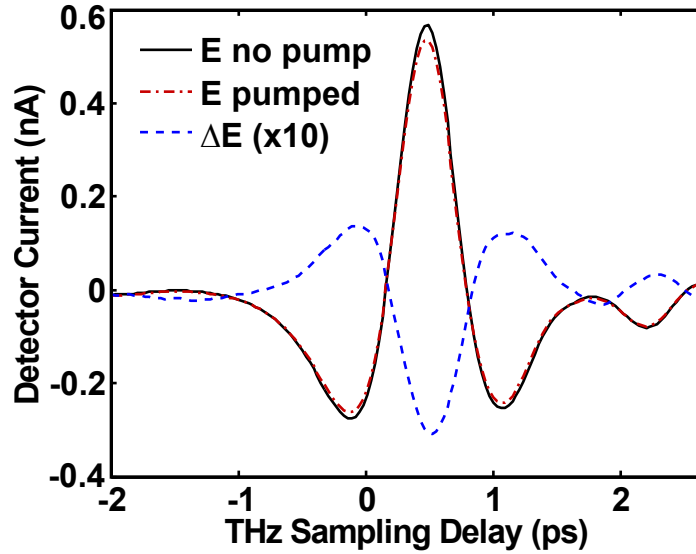


Figure 4.10: The electric fields of terahertz pulses transmitted through epitaxial graphene at  $T_{\text{sub}} = 18$  K are plotted with and without optical pumping. Also shown is  $\Delta E = (E \text{ pumped}) - (E \text{ no pump})$ . A small phase shift of less than 50 fs between the two pulses indicates that the Drude scattering time,  $\tau_D$ , is small.

and optical transmission spectroscopy to estimate the number of graphene layers. In experiments, the samples were placed in a Helium cryostat. We used the optical-pump THz-probe apparatus described in Section 2.5.1, with maximum pump pulse energies of  $\sim 11.4$  nJ and with a spot size on the sample of  $\sim 1.0$  mm<sup>2</sup>. The maximum estimated photoexcited carrier density was  $\sim 5 \times 10^{10}$  1/cm<sup>2</sup>, based on the absorption of graphene at 780 nm. In this measurement, the optical pump was incident on the sample at an angle (see Section 2.5.3), so the temporal resolution of our pump-probe measurement was limited to  $\sim 1$  ps.

The frequency dependence of the graphene conductivity has a Drude-like frequency dependence [146]. Changes in a terahertz probe pulse from photoexcited carriers in the graphene can be complex, requiring the complete measurements and analysis discussed in Section 2.5.2. However, in cases where the carrier momentum scattering time  $\tau_D$  is much shorter than the time scale associated with all other dynamics of interest, then the transmitted terahertz pulse is essentially the input terahertz

pulse with an amplitude modulation given by the instantaneous carrier distribution [47, 109]. Figure 4.10 shows the field amplitude of a terahertz pulse transmitted through a 14 mono-layer (ML) graphene sample with ( $E_p$ ) and without ( $E_0$ ) optical pumping. Their difference,  $\Delta E$ , is also shown. The maximum observed phase shift is less than 50 fs, indicating that the electronic scattering time  $\tau$  is indeed very short in our samples. We are therefore justified in tracking only the peak amplitude of the terahertz probe pulse as a function of the pump-probe delay.

The normalized differential transmission amplitude  $\Delta E/E$  of the terahertz probe pulse, as a function of the probe delay time, is shown in Figure 4.11 for different substrate temperatures on the same 14 ML graphene sample. The following observations can be made from this data. Immediately after photoexcitation,  $\Delta E/E$  decreases on a time scale of  $\sim 1$  ps, although this observation is limited by the resolution of the experimental apparatus. After  $\sim 1$  ps,  $\Delta E/E$  recovers over time scales that strongly depend on the substrate temperature  $T_{\text{sub}}$ . Decreasing the substrate temperature causes the recovery times to increase from tens of picoseconds at room temperature to hundreds of picoseconds at low temperatures. At low substrate temperatures, we observe two distinct time scales: a fast recovery phase lasting to about 50 ps and a much slower phase lasting to hundreds of picoseconds. Measurement of the transients over time scales longer than 300 ps were not possible with our setup. Also, the peak magnitude  $|\Delta E/E|$  is larger at lower substrate temperatures, increasing by as much as an order of magnitude at  $T_{\text{sub}} = 18$  K compared to  $T_{\text{sub}} = 300$  K.

In order to explore whether heat transfer either among the graphene layers or between the graphene layers and the substrate could be responsible for any of the features observed in our experiments [51], we performed measurements on epitaxially grown graphene samples with different numbers of graphene layers. We observed no significant changes in the observed time scales between the samples. Figure 4.12

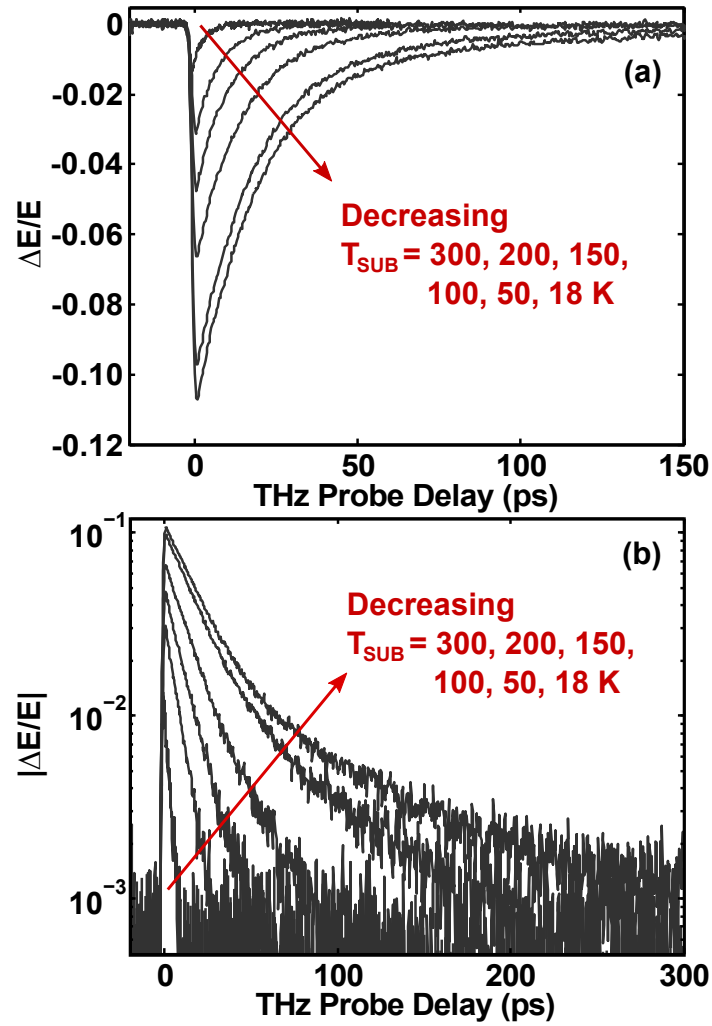


Figure 4.11: (a) Measured differential terahertz probe transmission  $\Delta E/E$  is plotted as a function of the probe delay for a  $\sim 14$  layer epitaxial graphene sample at six different substrate temperatures ( $T_{\text{sub}}=300, 200, 150, 100, 50,$  and  $18$  K). The estimated photoexcited carrier density is  $5 \times 10^{10}$   $1/\text{cm}^2$ . Lower substrate temperatures result in larger peak  $|\Delta E/E|$  values and slower relaxation rates. (b) The same data as in (a) shown on a log scale.

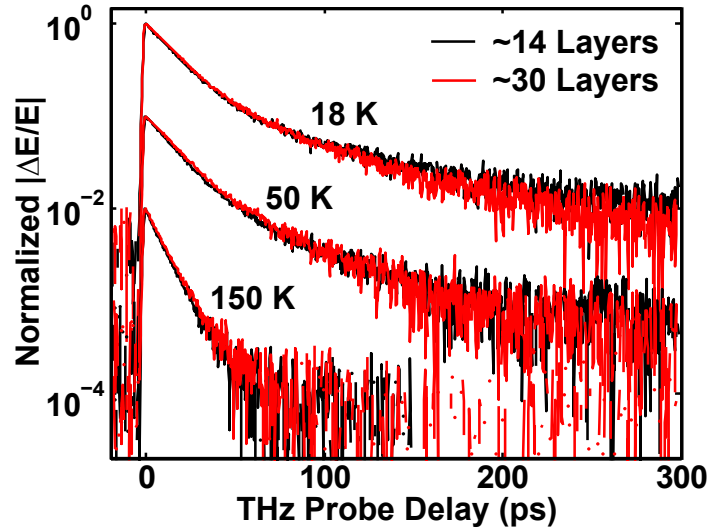


Figure 4.12: Measured  $\Delta E/E$  transients for  $\sim 14$  ML and  $\sim 30$  ML epitaxial graphene samples are plotted for different substrate temperatures.  $\Delta E/E$  transients for the 14 ML and 30 ML samples are normalized to the same peak magnitude and shifted along the vertical axis at each substrate temperature for clarity. Although the sample thicknesses differ by a factor of 2, the measured relaxation time scales are nearly identical.

shows the results obtained for samples having 14 and 30 mono layers (ML) of graphene at different substrate temperatures. For clarity in comparison,  $\Delta E/E$  values shown in Figure 4.12 have been normalized so that the peak values for the 14 ML and 30 ML samples are equal. The time scales associated with the transients are virtually identical despite the large difference in the number of graphene layers between the two samples. These observations are consistent with a model where, as discussed below, the coupling between graphene and the substrate is minimal within the measured timescales.

### 4.3.2 Model of Carrier Cooling in Graphene

In this section, we discuss our model for carrier cooling in graphene, which is in good agreement with the measured data and consistent with the understanding of dynamics presented in the literature. In the Section 4.3.4 we discuss possible shortcomings of

this model and how more recent developments in literature have built on its insights.

We assume that immediately after photoexcitation, the photoexcited electrons and holes thermalize among themselves as well as with the existing carriers through carrier-carrier scattering on a time scale of tens of femtoseconds [147, 129]. After thermalization, the carriers have Fermi-Dirac energy distributions with well-defined Fermi-levels ( $E_{\text{fe}}$  and  $E_{\text{fh}}$  for electrons and holes respectively) and a common temperature  $T_{\text{eh}}$ . We estimate the initial values of  $E_{\text{fe}}$ ,  $E_{\text{fh}}$ , and  $T_{\text{eh}}$  for our simulations by solving a system of equations for the conservation of number and energy of particles post-thermalization:

$$\begin{aligned} n_{\text{e}}(E_{\text{fe}}, T_{\text{eh}}) &= n_{+} + n_{\text{e},0} \\ n_{\text{h}}(E_{\text{fh}}, T_{\text{eh}}) &= n_{+} + n_{\text{h},0} \\ \epsilon(E_{\text{fe}}, E_{\text{fh}}, T_{\text{eh}}) &= \hbar\omega_{\text{p}}n_{+} + \epsilon_0 \end{aligned} \tag{4.8}$$

Here,  $n_{\text{e}}$ ,  $n_{\text{h}}$ ,  $n_{\text{e},0}$ ,  $n_{\text{h},0}$ , and  $n_{+}$  are the electron density, hole density, electron density pre-photoexcitation, hole density pre-photoexcitation, and photoexcited electron density, respectively. The values of  $n_{\text{e},0}$  and  $n_{\text{h},0}$  depend on the equilibrium Fermi energy and substrate temperature. Also,  $\epsilon_0$  and  $\epsilon$  are the total electron-hole energy densities pre-photoexcitation and post-thermalization, respectively.  $\hbar\omega_{\text{p}} = 1.6$  eV is the pump photon energy.

We simulate the subsequent evolution of the electron, hole, and phonon distributions using coupled rate equations for the electron density  $n_{\text{e}}$ , hole density  $n_{\text{h}}$ , electron/hole temperature  $T_{\text{eh}}$ , optical phonon occupation numbers  $n_{\Gamma}$  and  $n_K$  at the  $\Gamma$  and  $K$ -points of the Brillouin zone, and the acoustic phonon temperature  $T_{\text{a}}$ . The intraband and interband electron and hole scattering via optical phonons is described according to the models presented by Wang *et al.* [131] and Rana *et al.* [142]. The

interband electron and hole scattering via Auger and impact ionization is described using the model of Rana *et al.* [140]. The intraband electron and hole scattering via longitudinal acoustic phonons is described according to the model presented by Suzuura and Ando [148] using a value of 19 eV for the deformation potential. The interband electron and hole scattering via plasmons is described using the model of Rana *et al.* [143]. The anharmonic decay of optical phonons into acoustic phonons is described phenomenologically with the time constant  $\tau_{\text{opt}}$ , which has typical values in the 0.5-2.5 ps range [131, 136, 149, 150]. The loss of heat from the graphene acoustic phonons into the substrate is also described phenomenologically with the time constant  $\tau_{\text{sub}}$ , which has values in the 25-200 ps range [51].

The first of these rate equations relates the rate of carrier temperature change,  $dT_{\text{eh}}/dt$ , to the rate of change of the carrier energy density,  $dU_e/dt + dU_h/dt$ , and carrier densities,  $dn_e/dt$  and  $dn_h/dt$ . Including these terms, we write

$$\frac{dT_{\text{eh}}}{dt} = \frac{1}{C_e + C_h} \left( \frac{dU_e}{dt} + \frac{dU_h}{dt} - \chi_e \frac{dn_e}{dt} - \chi_h \frac{dn_h}{dt} \right) \quad (4.9)$$

Here,  $C_e$  and  $C_h$  are the electron and hole heat capacities, and  $\chi_e$  is given in terms of integrals of the Fermi-Dirac distribution  $f(\cdot)$  as

$$\chi_e = \frac{\int_0^\infty dE E^2 f(E_{\text{fe}}, T_{\text{eh}})(1 - f(E_{\text{fe}}, T_{\text{eh}}))}{\int_0^\infty dE E f(E_{\text{fe}}, T_{\text{eh}})(1 - f(E_{\text{fe}}, T_{\text{eh}}))} \quad (4.10)$$

The expression for  $\chi_h$  is obtained by substituting  $-E_{\text{fh}}$  for  $E_{\text{fe}}$  in the above equation. Equations 4.9 and 4.10 show that recombination (generation) due to carrier-carrier interactions (Auger scattering, impact ionization, and plasmon emission and absorption), in which the total energy of the electrons and holes does not change, always results in an increase (decrease) in the temperature of the carriers. Also note that for all the recombination and generation models we consider, when  $E_{\text{fh}} > E_{\text{fe}}$ , the

generation rate exceeds the recombination rate. When  $E_{\text{fh}} < E_{\text{fe}}$ , the opposite is true [142, 140, 143].

In accordance with the model presented by Wang *et al.* [131], we express the rate of change of the carrier energy density in terms of the optical and acoustic phonon emission rates[142]. The  $\Gamma$  and K subscripts refer to optical phonons at the  $\Gamma$  ( $\hbar\omega_{\Gamma} = 0.196$  eV) and K ( $\hbar\omega_{\text{K}} = 0.162$  eV) modes, respectively. We include interband optical phonon scattering rates ( $R_{\Gamma}$  and  $R_{\text{K}}$ , unit:  $\text{s}^{-1}\text{cm}^{-2}$ ) [142], intraband optical phonon scattering rates ( $R_{\Gamma\text{e}}$ ,  $R_{\Gamma\text{h}}$ ,  $R_{\text{Ke}}$ , and  $R_{\text{Kh}}$  for electrons and holes, unit:  $\text{s}^{-1}\text{cm}^{-2}$ ) [142], and rates of energy loss to acoustic phonon scattering ( $S_{\text{e}} + S_{\text{h}}$ , unit:  $\text{eVs}^{-1}\text{cm}^{-2}$ ) [148]. For the electron rate of change of energy density, we have

$$\frac{dU_{\text{e}}}{dt} = -(\hbar\omega_{\Gamma}R_{\Gamma\text{e}} + \hbar\omega_{\text{K}}R_{\text{Ke}} + S_{\text{e}}) \quad (4.11)$$

The expression for  $dU_{\text{h}}/dt$  is the same as Equation 4.11 with h subscripts replacing e subscripts.

In our simulations, we include rate equations for the phonon density at the  $\Gamma$  and K modes ( $n_{\Gamma}$  and  $n_{\text{K}}$ , respectively) as a result of electron scattering as well as anharmonic decay into acoustic phonons. The rate of optical phonon decay into two acoustic phonons is related to the acoustic phonon density at the modes with half of the energy of the respective optical phonon mode. For example, the  $\Gamma$  phonons decay into two acoustic phonons with energy  $\hbar\omega_{\Gamma}/2$ , so the rate of change of  $\Gamma$  phonons due this process is  $n_{\Gamma}(1 + n_{\Gamma\text{a}})^2/\tau_{\text{opt}}$ . Here,  $n_{\Gamma\text{a}}$  (unit:  $\text{cm}^{-2}$ ) is the acoustic phonon occupation of the LO mode with energy  $\hbar\omega_{\Gamma}/2$ . Including anharmonic recombination

as well as generation, the rate equations for  $\Gamma$  and K phonon densities are

$$\frac{dn_{\Gamma}}{dt} = \frac{R_{\Gamma e} + R_{\Gamma h}}{M_{\Gamma\text{tra}}} + \frac{R_{\Gamma}}{M_{\Gamma\text{ter}}} - \frac{n_{\Gamma}(1 + n_{\Gamma a})^2 - n_{\Gamma a}^2(1 + n_{\Gamma})}{\tau_{\text{opt}}} \quad (4.12)$$

$$\frac{dn_{\text{K}}}{dt} = \frac{R_{\text{Ke}} + R_{\text{Kh}}}{M_{\text{Ktra}}} + \frac{R_{\text{K}}}{M_{\text{Kter}}} - \frac{n_{\text{K}}(1 + n_{\text{Ka}})^2 - n_{\text{Ka}}^2(1 + n_{\text{K}})}{\tau_{\text{opt}}} \quad (4.13)$$

where  $M_{X\text{tra}}$  and  $M_{X\text{ter}}$  are the number density of optical phonon modes available for intraband and interband scattering of electrons, respectively [131, 142].

For the acoustic phonon temperature,  $T_{\text{a}}$ , we use a rate equation that includes the aforementioned carrier scattering and anharmonic decay of optical phonons, as well as equilibration with the substrate temperature on the phenomenological timescale  $\tau_{\text{sub}}$ , written

$$\begin{aligned} \frac{dT_{\text{a}}}{dt} = & \frac{S_{\text{e}} + S_{\text{h}}}{C_{\text{a}}} + \hbar\omega_{\Gamma}(M_{\Gamma\text{tra}} + M_{\Gamma\text{ter}}) \frac{n_{\Gamma}(1 + n_{\Gamma a})^2 - n_{\Gamma a}^2(1 + n_{\Gamma})}{C_{\text{a}}\tau_{\text{opt}}} \\ & + \hbar\omega_{\text{K}}(M_{\text{Ktra}} + M_{\text{Kter}}) \frac{n_{\text{K}}(1 + n_{\text{Ka}})^2 - n_{\text{Ka}}^2(1 + n_{\text{K}})}{C_{\text{a}}\tau_{\text{opt}}} - \frac{T_{\text{a}} - T_{\text{sub}}}{\tau_{\text{sub}}} \end{aligned} \quad (4.14)$$

where  $C_{\text{a}}$  is the acoustic phonon heat capacity [142].

Finally, we include rate equations for the electron and hole densities, which include recombination from interband optical phonon scattering and a phenomenological recombination term incorporating Auger scattering and plasmon emission, which we estimate to have a time scale of  $\tau_{\text{r}} \approx 1$  ps [140, 143]:

$$\frac{dn_{\text{e}}}{dt} = -(R_{\Gamma} + R_{\text{K}}) - \frac{n_{\text{e}} - n_{\text{e},0}}{\tau_{\text{r}}} \quad (4.15)$$

$$\frac{dn_{\text{h}}}{dt} = -(R_{\Gamma} + R_{\text{K}}) - \frac{n_{\text{h}} - n_{\text{h},0}}{\tau_{\text{r}}} \quad (4.16)$$

Equations 4.15 and 4.16, along with Equations 4.9, 4.12, 4.13, and 4.14 form the set of coupled rate equations we use for our simulations of the evolution of the carrier

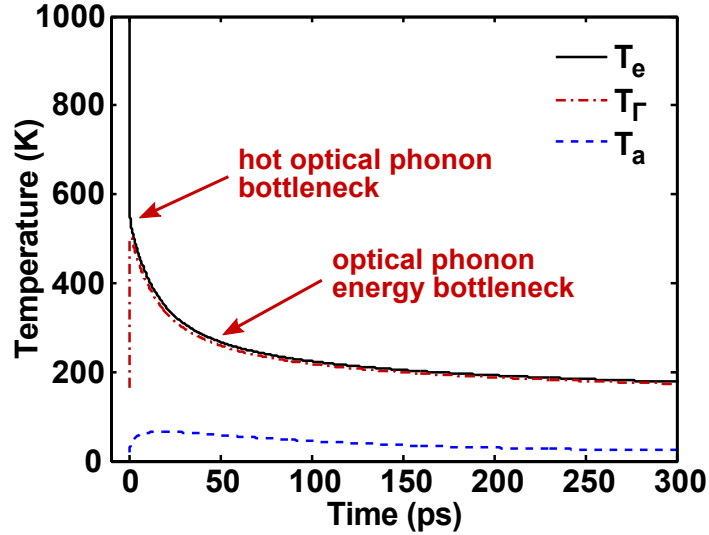


Figure 4.13: Simulation results of the electronic temperature,  $T_{\text{eh}}$ , the optical phonon temperature,  $T_{\Gamma} (\approx T_{\text{K}})$ , and the acoustic phonon temperature,  $T_{\text{a}}$ , as a function of time after photoexcitation.  $T_{\text{sub}} = 18$  K.

and phonon distributions following photoexcitation and thermalization.

We plot representative results from the simulations in Figures 4.13 and 4.14. Figure 4.13 shows the carrier temperature  $T_{\text{eh}}$ , optical phonon temperatures  $T_{\Gamma} (\approx T_{\text{K}})$ , and the acoustic phonon temperature  $T_{\text{a}}$  plotted as a function of time. Figure 4.14(a) shows the electron and hole Fermi levels,  $E_{\text{fe}}$  and  $E_{\text{fh}}$ , and Figure 4.14(b) shows the electron and hole densities,  $n_{\text{e}}$  and  $n_{\text{h}}$ . For the simulations, we used the values  $n_{+} = 5 \times 10^{10}$   $1/\text{cm}^2$ ,  $T_{\text{sub}} = 18\text{K}$ ,  $\tau_{\text{D}} = 28$  fs,  $\tau_{\text{opt}} = 1.6$  ps,  $\tau_{\text{sub}} = 100$  ps, and we assumed that the sample was slightly  $n$ -doped with doping density  $N_{\text{d}} = 1 \times 10^{11}$   $1/\text{cm}^2$ .

The story of carrier relaxation in graphene, told by our simulations, is as follows. Immediately after thermalization, the carrier temperature is large ( $\sim 2300$  K in Figure 4.13) and  $E_{\text{fh}} \gg E_{\text{fe}}$ . In the initial relaxation phase lasting 0.5–1.0 ps, the carriers lose energy via optical phonon emission, and their distribution cools down relatively quickly. In this phase,  $E_{\text{fh}}$  exceeds  $E_{\text{fe}}$ , so the carrier generation rate exceeds the carrier recombination rate, and the electron/hole densities increase. As discussed

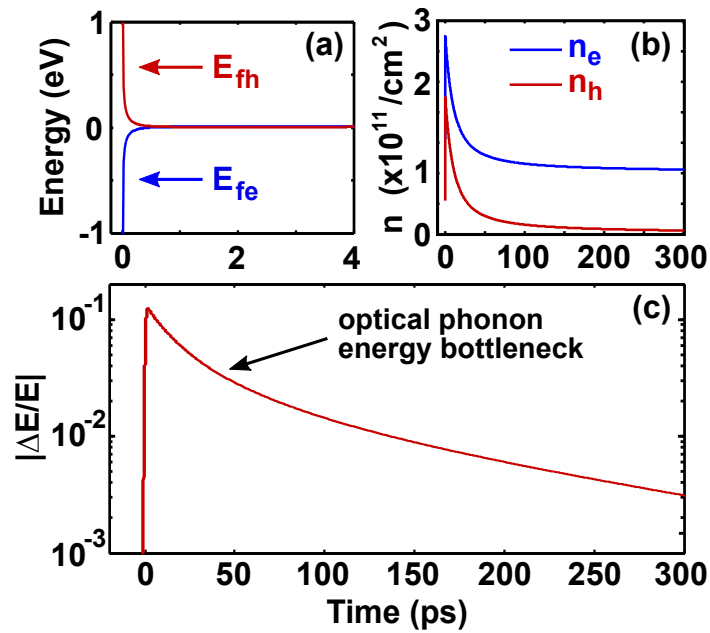


Figure 4.14: (a) Representative simulation results of the Fermi levels,  $E_{fe}$  and  $E_{fh}$ , for electrons and holes, respectively, as a function of time after photoexcitation. (b) Representative simulation results for the electron and hole densities,  $n_e$  and  $n_h$ , as a function of time. (c) Representative simulation results of the differential terahertz transmission  $|\Delta E/E|$  transient. Dashed lines indicate the approximate rate of relaxation at short and long time scales.

earlier regarding Equation 4.9, carrier generation via carrier-carrier interactions also contributes to a decrease of the carrier temperature. Within  $\sim 1$  ps picosecond, the electron and hole populations equilibrate and their Fermi levels merge. Beyond  $\sim 1$  ps, the electron and hole distributions can be approximately described by a common Fermi level; but strictly speaking now  $E_{fe} > E_{fh}$  by a small amount on the order of 5–10 meV, so recombination exceeds generation and the electron/hole densities decrease with time. In the same time frame of 0.5-1.0 ps, optical phonon emission leads to an increase in the optical phonon temperatures until the carrier and the optical phonon temperatures become nearly identical. After this point, hot optical phonons become the main bottleneck for further carrier cooling and carrier cooling slows dramatically [131], as indicated in Figure 4.13.

As the electron and hole distributions cool further, at some point the bulk of these distributions moves close enough to the Dirac point such that both the intraband and the interband scattering of carriers via optical phonon emission become inefficient in cooling the carriers. For the values considered in the simulations presented in Figures 4.13 and 4.14, this occurs when the carrier temperature falls below  $\sim 250$  K. Since longitudinal acoustic phonon scattering is also inefficient in cooling the carriers [148, 137, 138], the carrier cooling rate slows down further. This optical photon energy bottleneck is indicated in Figure 4.13. Note that the larger heat capacity of the acoustic phonons results in the maximum change in the acoustic phonon temperature being smaller than the maximum change in the optical phonon temperature.

The transmission of a terahertz pulse through  $N$  graphene layers on a SiC substrate normalized to the transmission through the SiC substrate is given by the expression [146],

$$\frac{T}{T_{\text{SiC}}} = \frac{1}{1 + N\sigma(\omega)\eta_0/(1 + n_{\text{SiC}})} \quad (4.17)$$

This is Equation 2.8, with the assumption that the  $N$  graphene layers are decoupled,

and the total conductivity is simply the sum of the individual layers. Here,  $n_{\text{SiC}}$  is the refractive index of the SiC substrate and  $\sigma(\omega)$  is the intraband conductivity of graphene given by [146],

$$\sigma(\omega) = i \frac{e^2/\pi\hbar^2}{\omega + i/\tau} \int_0^\infty (f(E_{fe}, T_{eh}) + f(-E_{fh}, T_{eh})) dE \quad (4.18)$$

Figure 4.14(c) shows the calculated relative differential transmission  $\Delta E/E$  of the terahertz probe pulse as a function of the probe delay. In the first  $\sim 1$  ps of the simulation, the graphene conductivity increases and the terahertz transmission decreases. This increase of conductivity is due to two factors. First, as the temperature of the carriers decreases, the graphene conductivity as given by Equation 4.18 increases. This results from graphene conductivity depending on both the total number of carriers and also on the carrier distribution in energy. For the same number of carriers, the conductivity is larger if the carrier temperature is smaller. Second, carrier generation also contributes to an increase in the number of carriers and, therefore, an increase in the conductivity. Beyond  $\sim 1$  ps, the conductivity decreases and the terahertz transmission increases. This decrease in conductivity is due to the decrease in the carrier densities as the carriers cool down. The relaxation of the  $\Delta E/E$  transient exhibits two distinct time scales: a first fast relaxation phase lasting to about 50 ps during which both intraband and interband optical phonon emission is efficient in cooling the carrier distributions, and the second slow phase lasting longer than hundreds of picoseconds during which optical phonon emission is inefficient in cooling the carriers.

	$T_{\text{sub}}=300$ K	$T_{\text{sub}}=150$ K	$T_{\text{sub}}=18$ K
$N_{\text{d}}$ (1/cm <sup>2</sup> )	$2.5 \times 10^{11}$	$1.4 \times 10^{11}$	$1.0 \times 10^{11}$
$\tau_{\text{D}}$ (fs)	5	13.7	28.3
$\tau_{\text{opt}}$ (ps)	0.8	1.1	1.6

### 4.3.3 Comparison of the Model to Data

Figure 4.15 shows the comparison between the theoretical model (solid lines) and the measurements (circles) of the differential terahertz transmission  $\Delta E/E$  for three different substrate temperatures,  $T_{\text{sub}} = 300, 150, 18$  K. The only three fitting parameters used in the simulations were the graphene doping density  $n_0$ , the carrier momentum scattering time  $\tau_{\text{D}}$ , and the optical phonon decay time  $\tau_{\text{opt}}$ . Table 4.3.3 gives the fitting values used for different substrate temperatures. We varied the time constant  $\tau_{\text{sub}}$ , which describes the loss of heat from the graphene layers into the substrate, between 25 ps and 100 ps [51]; however, we found its value to have no significant effect on the simulation results for  $\Delta E/E$ . The comparison between the simulations and the measurements is good. The model qualitatively reproduces the two distinct time scales observed experimentally in the transmission recovery transients at low substrate temperatures. The substrate temperature dependencies of the fitting parameters  $\tau_{\text{D}}$  and  $\tau_{\text{opt}}$  (Table 4.3.3) are in reasonable agreement with the expectations [151, 136, 149]. However, the mechanism responsible for the temperature dependence of the doping density  $n_0$ , although small, is unclear.

### 4.3.4 Outlook

The model we presented in Section 4.3.2 accurately reproduces the optical phonon energy bottleneck to carrier cooling in graphene. At low temperatures, cooling beyond  $\sim 1$  ps quickly becomes inefficient as the carrier distribution falls below the graphene optical phonon energies. Then on long ( $> 50$  ps) time scales, cooling by acoustic

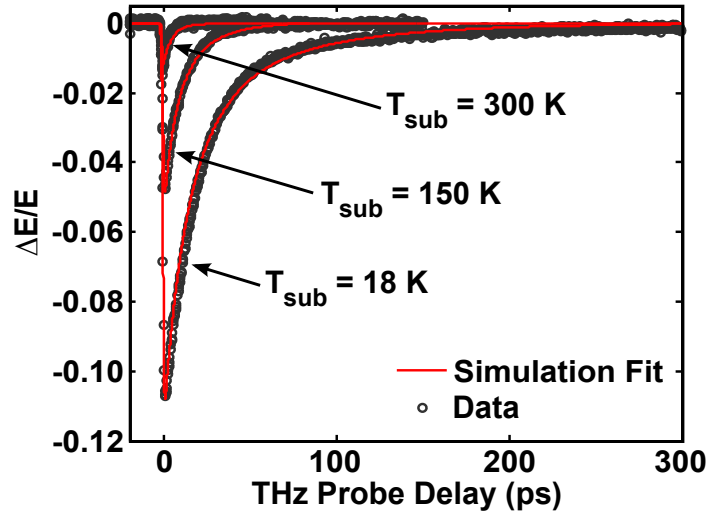


Figure 4.15: Measured  $\Delta E/E$  transients are plotted along with the simulation fits for different substrate temperatures.

phonons becomes dominant. But our simulations indicate that due to phase-space restrictions, the cooling via acoustic phonon emission is very slow ( $>1$  ns time scale) since only low-energy acoustic phonons satisfy energy-momentum conservation. This bottleneck is severe, and while apparently simple, is unusual in semiconductors and metals since in most cases the optical phonon energy is much smaller (e.g.  $\approx 36$  meV in GaAs), and the Fermi surface is much larger [152]. As a result of these unusual physics, the photoresponse in a graphene photodetector is dominated by hot carrier transport [127, 153].

One shortcoming of our model, however, is that it does not consider disorder. In fact, our simulations *overestimate* the degree to which the cooling in graphene slows down once optical phonon emission is quenched. In order for the simulations to match the optical-pump THz-probe transient at long time scales beyond 100 ps, it was necessary to adjust the doping parameter in what is likely an unphysical manner. For example, the measured cooling transient at 18 K slowed to a few-hundred picosecond time scale, while the simulations typically indicate the  $>1$  ns time scale of acoustic phonon scattering. One recent theory called “supercollision” cooling attempts to

resolve this discrepancy by considering the effects of disorder in the graphene lattice. In 2012, Song and Levitov [154] proposed the theory that defects could relax the momentum and energy constraints that limit acoustic phonon scattering, effectively increasing the rate of cooling at low temperatures and long time scales. This process could account for the reduced cooling time scales for graphene seen in measurements for certain doping ranges [155, 156].

# Chapter 5

## Semiconductor Plasmonics

Plasmonics, the field of manipulating charge density waves, has typically been a metal-based technology with promise for extreme sub-wavelength optics and infrared/THz active and passive devices [14, 15]. Metals are popular because they have large carrier densities, leading to large currents and strong light-matter interaction. Further, by confining charges into metallic nanostructures, the electric fields produced by the charge build-up at the edges of the particles cause a current resonance. This plasmonic resonance can increase the particle scattering cross-section for electromagnetic radiation spanning from microwaves to visible, depending on the size of the particle. This technology provides an engineering platform for filters, switches, active, and passive devices. But a common issue with metallic plasmonics is the large loss of the plasmonic wave in the metal. Due to the large number of excited states at the Fermi level, metals typically exhibit fast carrier momentum relaxation, which damps any plasma waves. In addition, metals have fixed carrier densities, and as a consequence, fixed operating frequencies once a device has been fabricated. In contrast, high-quality semiconductors have slow carrier momentum relaxation, and their carrier densities may be tuned through electrostatic gating. Thus, semiconductors provide an intriguing alternative to metals for tunable, high-performance plasmonic devices.

In this Chapter we present terahertz measurements of two semiconducting materials which provide charge confinement: germanium nanowires and graphene. We show that the THz conductivity of these materials is dominated by plasmonic effects, and we model and evaluate their performance for THz optoelectronics.

## 5.1 The Terahertz Response of Oriented Germanium Nanowires

In Section 4.2, we presented optical-pump THz-probe measurements of oriented Ge nanowires, 80  $\mu\text{m}$  in diameter. Using the time-domain nature of our THz spectrometer, we measured the intraband relaxation rate from the X- to the L-valley to be 1.7 ps, and we found carrier density-dependent recombination rates in the 75–125 ps range at room temperature. But in addition to the carrier relaxation dynamics, optical-pump THz-probe spectroscopy can reveal the fast electrical response of the nanowires at THz frequencies [41], as we have discussed in Section 2.5. With the techniques described in that section, we measure carrier momentum scattering times in the 60-90 fs range. Additionally, we find the THz response of oriented nanowires to be strongly dependent on the polarization of the THz field. The largest differential THz transmission signal through photoexcited nanowires occurs when the THz field is polarized parallel to the nanowires, while no appreciable response is detected when the THz field is polarized perpendicular to the nanowires. The shape anisotropy of the nanowires, which exist entirely at subwavelength scales, leads to a strong polarization dependent macroscopic THz response. As we will see, this response is best understood with the language of plasmonics. Our results indicate the practical possibility of realizing optically or electrically controlled active THz devices based on semiconductor nanowires.

Much of the material presented in this Section appears in Ref. [110] and was a collaboration between myself, Paul A. George, Mark Levendorf, Martin Blood-Forsythe, Jiwoong Park, and Farhan Rana.

### 5.1.1 Ge Nanowire Polarization Experiment

As described in Section 4.2.1, we performed optical-pump THz-probe measurements of a film of oriented Ge nanowires, lying flat on a quartz substrate (see Figure 4.6). The nanowires were 80 nm in diameter, and approximately 10  $\mu\text{m}$  in length. Both of these dimensions are at least an order of magnitude smaller than the shortest wavelength THz probe used in this measurement ( $c/(3 \text{ THz}) \approx 100 \mu\text{m}$ ). The primary modification to the experimental setup is the addition of a free-standing wire-grid polarizer (Microtech Instruments, Inc.). The THz pulse emitted from a photoconductive switch is well linearly polarized (perpendicular to the metal strip lines). But rotating the polarization is challenging, as is rotating the sample itself due to the sensitivity of the alignment. So in order to probe the THz response at different polarizations, we oriented the film such that the nanowires were aligned at a  $45^\circ$  angle from the incoming THz probe. Then we used the polarizer to sample the transmitted THz electric field. Figure 5.1 visually demonstrates this setup.

The THz frequency response of a finite length nanowire can be described by the Drude model, modified to consider the depolarization fields [9] due to the induced charges on the surface of the nanowire [41, 157, 158]. The inclusion of the depolarization field leads to a surface-plasmon-like resonance in the frequency-dependent current response of the nanowire. The current  $I(\omega)$  in a nanowire of cross-sectional area  $A$  can be written as,

$$I(\omega) = A \frac{\sigma_0}{1 - i\omega\tau_D} (E_{\text{ext}}(\omega) + E_d(\omega)) \quad (5.1)$$

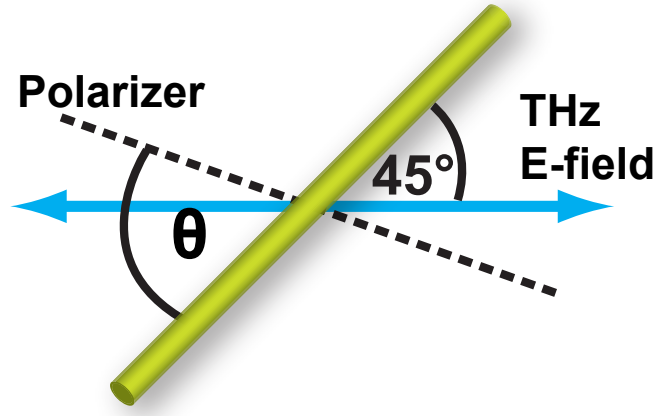


Figure 5.1: The incident THz polarization is fixed at  $45^\circ$  with respect to the nanowire axis. A polarizer is rotated at an angle  $\theta$  with respect to the nanowire axis to select THz polarization post-transmission.

where  $\sigma_o$  is the DC conductivity of the nanowire material,  $\tau$  is the carrier momentum scattering time (assumed to be the same for both electrons and holes [159]),  $E_{\text{ext}}(\omega)$  is the applied field and  $E_d(\omega)$  is the depolarization field. The above expression can also be expressed as,  $I(\omega) = A\sigma_{\text{eff}}(\omega)E_{\text{ext}}(\omega)$ , where the effective conductivity  $\sigma_{\text{eff}}(\omega)$  is

$$\sigma_{\text{eff}}(\omega) = \frac{\sigma_o}{1 - i\omega\tau_D(1 - \Omega_p^2/\omega^2)} \quad (5.2)$$

Here,  $\Omega_p$  is the frequency of the surface plasmon resonance.  $\Omega_p$  is related to the bulk plasma frequency  $\omega_p$  by a constant factor  $g$  that depends on the polarization of the applied field with respect to the nanowire axis (see Figure 5.2). For a field polarized perpendicular to the nanowire,  $g$  equals  $\sqrt{\epsilon_s/(\epsilon_s + \epsilon_o)}$ , where  $\epsilon_s$  and  $\epsilon_o$  are the permittivities of the nanowire material and free-space, respectively. In the case of the field polarization parallel to the nanowire, the value of  $g$  is small and is on the order of  $(d/L)\sqrt{\epsilon_s/\epsilon_o}$ , where  $d$  and  $L$  are the diameter and length of the nanowire respectively. Since  $d \ll L$ , when the field is polarized parallel to the nanowires,  $\Omega_p$  is much smaller than  $\omega_p$ . We estimate  $\Omega_p$  to be less than 300 GHz for even the largest photoexcited carrier densities in our experiments. The interaction between nanowires

is expected to reduce the depolarization field inside the nanowires and, therefore, further reduce the value of  $\Omega_p$ . At frequencies much larger than  $\Omega_p$ ,  $\sigma_{\text{eff}}(\omega)$  reduces to the Drude result, and in the DC limit,  $\sigma_{\text{eff}}(\omega)$  goes to zero as it should for a finite-length uncontacted nanowire. The differential THz transmission (normalized to the transmission in the absence of photoexcitation) can be written as,

$$\begin{aligned} \frac{\Delta t(\omega)}{t} &= \frac{1}{1 + \sigma_{\text{eff}}(\omega) F(\omega) \eta_o f d / (1 + n)} - 1 \\ &\approx -\sigma_{\text{eff}}(\omega) F(\omega) \eta_o f d / (1 + n) \end{aligned} \quad (5.3)$$

where  $\eta_o$  is the impedance of free space,  $f \approx .08$  is the fill factor of the nanowires,  $d = 80$  nm is the diameter of a nanowire, and  $n = 1.96$  is the THz refractive index of the quartz substrate [160].  $F(\omega)$  is an overlap factor that accounts for the frequency dependence of the measured THz response due to the mismatch between the optical and THz focus spots. Assuming Gaussian transverse intensity profiles for the optical and THz beams, the overlap factor is found to be,

$$F(\omega) = \omega^2 / (\omega_o^2 + \omega^2) \quad (5.4)$$

where  $\omega_o \approx 2\pi c/a$  is approximately the frequency corresponding to the standard deviation,  $a = 150$   $\mu\text{m}$ , of the optical beam transverse intensity profile.

In the case of the THz field polarized along the nanowires, since  $\Omega_p \ll \omega$  for frequencies  $\omega$  in the 0.5-3.0 THz range,  $\sigma_{\text{eff}}(\omega)$  has the frequency dependence of the Drude model. There is therefore no carrier density dependence in the frequency dispersion of the differential THz transmission, in agreement with the measured results shown earlier in Figure 4.7. Figure 5.3 shows the measured frequency spectra (solid lines) of  $|\Delta E(\omega)/E|$  for different pump pulse energies. Also shown are the theoretical fits (dashed lines) obtained from Equation 5.3. As seen in Figure 5.3, the theory

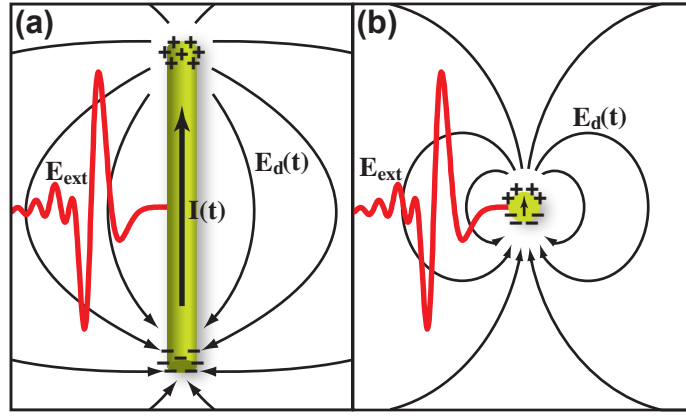


Figure 5.2: (a) A nanowire oriented parallel to the polarization of the external THz field ( $E_{\text{ext}}$ ). The depolarization field ( $E_d$ ) due to charge confinement on the surface of the nanowire is weak, allowing a Drude-like induced current. (b) A nanowire oriented perpendicular to the external field polarization. Here, the depolarization field is strong, suppressing the induced current.

agrees well with both the frequency dependence and the carrier density dependence of the data. From our fits, we find the momentum scattering time to be  $\tau_D = 70 \pm 15$  fs, which corresponds to an effective electron plus hole mobility of  $1590 \text{ cm}^2\text{V}^{-1}\text{sec}^{-1}$ . This is smaller than the reported value for the bulk Germanium electron plus hole mobility of  $5700 \text{ cm}^2\text{V}^{-1}\text{sec}^{-1}$  at 300 K [159].

Photoexcited carriers in oriented nanowires are expected to exhibit a polarization dependent THz response due to the geometries depicted in Figure 5.2. As a result of the nanowire film and polarizer orientation described in Figure 5.1, the THz field had components both parallel and perpendicular to the nanowires. After transmission through the nanowire sample, the field polarization was selected for measurements of  $\Delta E/E$  by rotating the polarizer through an angle  $\theta$  with respect to the nanowires. Figure 5.4 shows the measured values of  $|\Delta E/E|$  for different angles  $\theta$ . The most striking feature of the data is the absence of any measurable THz response when the field is polarized perpendicular to the nanowires. In this case, the surface plasmon frequency  $\Omega_p$  equals  $\omega_p \sqrt{\epsilon_s / (\epsilon_s + \epsilon_o)}$  and is in the tens of THz range for the photoexcited carrier densities in our experiments. Equation 5.2 shows that when  $\Omega_p \gg \omega$ , and

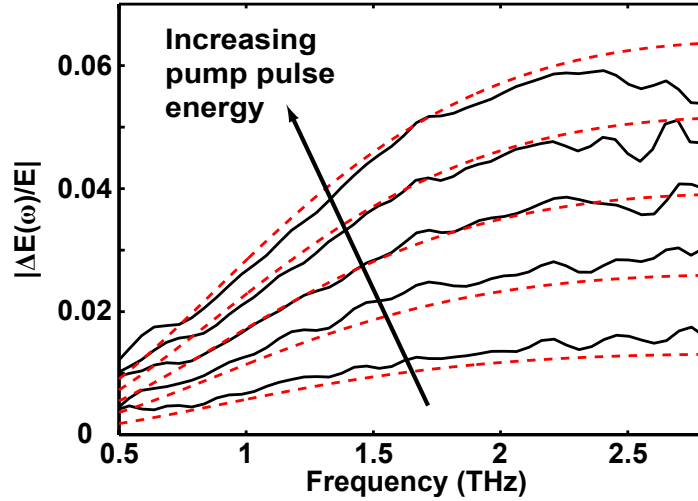


Figure 5.3: Data (solid) and theory (dashed) for the spectra of the differential THz transmission  $|\Delta E(\omega)/E|$  are shown for different pump pulse energies. The theory uses a standard deviation of  $\sim 150 \mu\text{m}$  for the optical intensity profile at the focus and a momentum scattering time  $\tau_D = 70 \pm 15$  fs independent of the carrier density.

the product  $\omega\tau_D$  is not too small, the induced current is significantly reduced compared to the case when  $\Omega_p \ll \omega$ . Therefore, for perpendicular THz field components, the depolarization field is strong enough to suppress the induced current, and so the resulting THz response is much weaker compared to that for parallel components. In this way, the shape anisotropy of the nanowires on subwavelength scales determines the polarization dependence of the THz response. Assuming that the THz response of oriented nanowires is negligibly small when the field is polarized perpendicular to the nanowires, the measured THz transmission is expected to be proportional to the cosine of the angle between the field polarization and the nanowire axis. In our experiments, since the field polarization is selected post-transmission, the measured values of  $|\Delta E/E|$  are expected to be proportional to  $\cos(\theta)/\cos(\pi/4 - \theta)$ . Figure 5.4(b) shows that the (peak) values of  $|\Delta E/E|$  exhibit exactly this angular dependence.

Plasmonic confinement is responsible for the dramatic polarization-dependence of the THz response in Ge nanowires. There is the tendency to lean on the intuition that in a structure with dimensions such as a nanowire, charge can flow in the

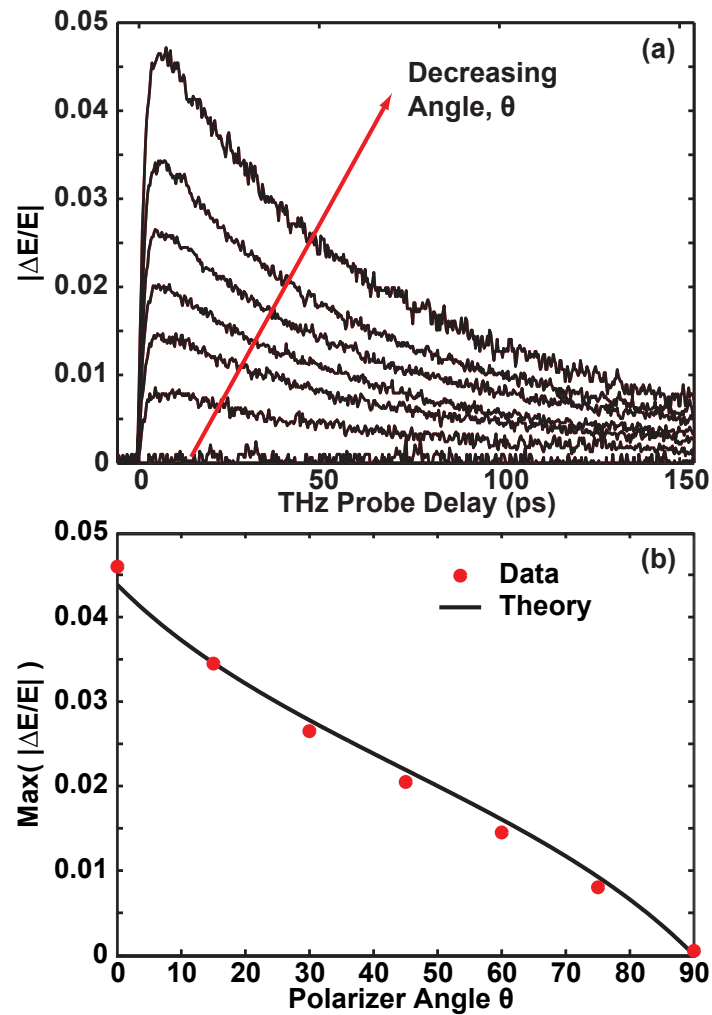


Figure 5.4: (a) Measured differential terahertz transmission  $|\Delta E/E|$  as a function of pump-probe delay for polarizer angles of  $\theta = 0, 15, 30, 45, 60, 75, 90$  degrees. At  $\theta = 90$  degrees,  $|\Delta E/E|$  is negligibly small and lost in the noise. (b) Maximum values of  $|\Delta E/E|$  are shown versus the polarizer angle  $\theta$ . The angular dependence expected from the theory is also plotted (solid line).

parallel direction, and physical confinement simply prevents charge from flowing in the perpendicular direction. But this picture is too simplistic. The depolarization field is required for a nuanced understanding of conduction in semiconductor micro- and nanostructures. After all, it is the depolarization field which ultimately prevents conduction below the plasma resonance frequency. This plasmonic theory also accounts for the polarization-dependence of the measurement, despite the nanowires being severely subwavelength in all dimensions compared to the probe. Ultimately, plasmonics is framework within which to properly understand the AC conductivity in semiconductor nanowires for active THz devices.

## 5.2 Confined Plasmons in Graphene Microstructures

Graphene electronics and optoelectronics have emerged as fields of tremendous interest not only as improvements to existing technology, but also as platforms for completely novel devices. A particularly interesting application of graphene is for plasmonic devices [161, 162, 163], which manipulate charge density waves in the two-dimensional atomic sheet. Graphene plasmons can have frequencies in the 1-100 terahertz range but wavelengths in the micron and sub-micron range [164, 163, 165], enabling extreme confinement of electromagnetic energy. In addition, plasmon frequencies in graphene can be tuned through electrostatic [161] or chemical [162] doping, making graphene plasmonics a unique platform for tunable terahertz sources, detectors, switches, filters, interconnects, and sensors.

The dispersion of plasmons in bulk graphene has been obtained analytically [164], and the experimental results have been shown to agree well with the theoretical predictions [165]. Plasmons can be confined in patterned graphene micro- and nanostructures such that only a discrete set of modes can oscillate [161, 162]. Such confined plasmon modes are of interest for device applications since, unlike bulk plasmons, they can couple directly to normally incident electromagnetic radiation. Confined plasmon modes have been observed and analyzed in two-dimensional electron gases in parabolic-band semiconductors [166, 167, 168]. Several numerical and analytical models have also been reported for describing the plasmons in graphene microstructures [169, 170, 171, 172, 173, 174]. Yet, models for confined plasmons in graphene

have not been compared quantitatively against experiments, and the accuracy of models based on classical electrodynamics remains unclear. For example, although experiments have shown that the scaling of the confined plasmon frequency with conductivity and size is in agreement with the long wavelength bulk plasmon dispersion [161, 162], there have been no direct comparisons of the predicted plasmon frequencies with the measured values.

In this Section, we present and quantitatively compare experimental and theoretical results for confined plasmon modes in graphene. We show that the long wavelength plasmon modes in graphene microstructures can be described by an eigenvalue equation. Using perturbation theory, we extend the eigenvalue equation to plasmon supermodes of arrays of interacting graphene microstructures. The results obtained from this method match well the results obtained using a numerical finite-difference time-domain (FDTD) technique. By comparing the measured transmission spectra of interacting plasmon modes in arrays of graphene strips with the theoretical results, we show that the theoretical models quantitatively match the experimental data very well.

Much of the material presented in this Section appears in Ref. [175] and was a collaboration between myself, Parinita Nene, Wei-Min Chan, Christina Manolatu, Sandip Tiwari, Farhan Rana, Joshua W. Kevek, and Paul L. McEuen.

### 5.2.1 Far-IR Spectroscopy of Graphene Plasmonic Strips

A cross-section of the structures considered in this work is shown in Figure 5.5(a), which shows an array of patterned graphene strips. The graphene used in our experiments was grown by chemical vapor deposition (Kevek Innovations 1" System) on copper foils and transferred, as described by Li et al. [176], to high-resistivity silicon wafers ( $>10 \text{ k}\Omega\text{-cm}$ ) with  $\sim 300 \text{ nm}$  of thermally grown  $\text{SiO}_2$ . Arrays of graphene strips

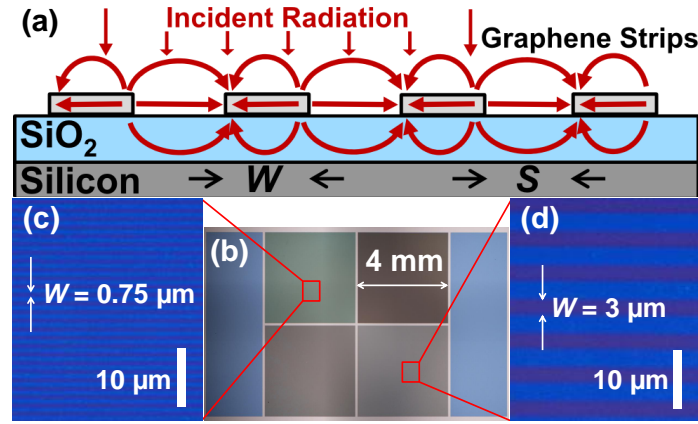


Figure 5.5: (a) A cross-section (not to scale) of an array of graphene strips with the electric field lines for the lowest plasmon supermode. (b) Optical micrograph of the sample with four regions of etched graphene strips (square regions in the center) and two reference regions. (c,d) Bright-field optical micrographs (100X) detailing etched graphene strip arrays after the resist was removed.

of widths  $W = 0.75, 1, 2,$  and  $3 \mu\text{m}$  were patterned using standard photolithography followed by etching in an oxygen plasma (see Fig 5.5(b)). For all devices, the strip width  $W$  and the spacing  $S$  between the strips were chosen to be equal. Graphene strips were doped using  $\text{HNO}_3$  [177]. The doping density was estimated to be in the  $4.5\text{-}5.0 \times 10^{12} \text{ cm}^{-2}$  range using the Raman technique described by Das et al. [178].

Plasmon resonances of arrays of graphene strips were measured at room temperature using Fourier-transform infrared spectroscopy (FTIR). Figure 5.6 shows the transmission spectra, of all four strip sizes, for polarizations perpendicular (a) and parallel (b) to the strips. The transmission of incident radiation polarized parallel to the strips decreases monotonically at long wavelengths, showing the expected Drude-like frequency dependence. There is no dependence on the strip width. Transmission spectra of incident radiation polarized perpendicular to the strips show plasmon resonances [161, 162].

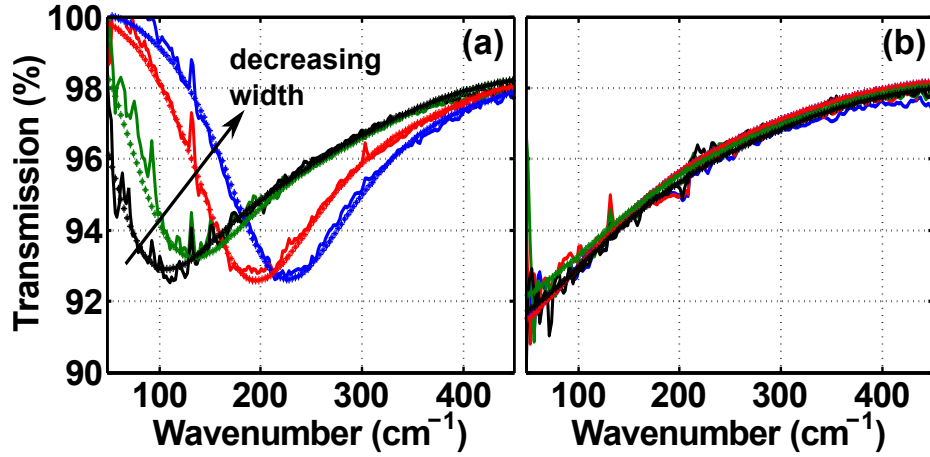


Figure 5.6: (Solid) Measured transmission of radiation polarized (a) perpendicular and (b) parallel to graphene strips is plotted for four different strip widths  $W = 0.75, 1, 2,$  and  $3 \mu\text{m}$ . For all devices, the spacing  $S$  between strips is equal to the width. A bare  $\text{SiO}_2/\text{Si}$  substrate is used as reference. (Dots) FDTD simulation fits to the measured results. Extracted resonance frequencies are  $226, 197, 135,$  and  $112 \text{ cm}^{-1}$ .

### 5.2.2 Basic Plasmon Model

As described in Section 5.1, the measured transmission spectra can be described qualitatively using a damped harmonic oscillator model[158, 110, 161, 162, 173] for the effective conductivity,

$$\frac{T_\xi(\omega)}{T_{\text{ref}}(\omega)} = \left| 1 + \frac{\eta_o f \sigma(\omega=0)}{1 + n_{\text{sub}}} \frac{i\omega/\tau}{\omega^2 - \xi \Omega_p^2 + i\omega/\tau_D} \right|^{-2} \quad (5.5)$$

Here,  $\eta_o$  is the free-space impedance,  $\sigma(\omega=0)$  is the DC conductivity of bulk graphene,  $f$  is the fill-factor of the strips,  $n_{\text{sub}}$  is the refractive index of the substrate,  $\tau$  is the Drude scattering time,  $\Omega_p$  is the confined plasmon frequency, and  $\xi = 0$  (or 1) for incident radiation polarized parallel (or perpendicular) to the strips. The bulk plasmon frequency for small wavevectors is given by the expression [164],

$$\omega_p(q) = \sqrt{\frac{\sigma(\omega=0)q}{2\epsilon_{\text{avg}}\tau_D}} \quad (5.6)$$

where  $q$  is the magnitude of the plasmon wavevector and  $\epsilon_{\text{avg}}$  is the average dielectric constant surrounding the graphene sheet. Using  $q = \pi/W$  [179], we find that Equation 5.6 significantly overestimates the confined plasmon frequencies compared to the experimental values. For example, using Equation 5.5 to fit the transmission spectra of  $W = 1 \mu\text{m}$  arrays for parallel polarizations ( $\xi = 0$ ), we find the average value of  $\sigma(\omega = 0)$  and  $\tau_{\text{D}}$  to be 0.95 mS and 31.5 fs, respectively. Equation 5.6 then gives a plasmon frequency of  $\sim 245 \text{ cm}^{-1}$ , which is significantly higher than the measured confined plasmon frequency of  $\Omega_p \approx 197 \text{ cm}^{-1}$ . Such a large error suggests that better models are needed to understand confined plasmon modes in patterned graphene structures.

### 5.2.3 Analytic Electrodynamic Model

We first present an analytic technique that captures the essential physics of the problem and results in an eigenvalue equation for the plasmon modes. This method is essentially an analytical computation of the geometrical factor  $g$  from Section 5.1. Assuming a Drude-like frequency dependence of the graphene conductivity [146], we start with the time-derivative of the equation for the 2-D current density  $\vec{K}$ ,

$$\frac{\partial^2 \vec{K}}{\partial t^2} + \frac{1}{\tau_{\text{D}}} \frac{\partial \vec{K}}{\partial t} = \frac{\sigma(\omega=0)}{\tau_{\text{D}}} \frac{\partial}{\partial t} \left( \vec{E}_{\text{inc}} + \vec{E}_d \right) \quad (5.7)$$

Here,  $\vec{E}_{\text{inc}}$  is the incident field and  $\vec{E}_d$  is the depolarization field that results from the plasmon charge density. Only field components in the plane of the graphene sheet are included in Equation 5.7.

We wish to relate the time derivative of the depolarization field in a graphene microstructure to the 2D sheet current density. We start with the expression for

electrostatic potential due to the charges within the graphene:

$$\phi(\vec{r}, t) = \int d^3\vec{r}' \frac{\rho(\vec{r}', t)}{4\pi\epsilon|\vec{r} - \vec{r}'|} \quad (5.8)$$

where  $\rho$  is the charge density and  $\epsilon$  is the average dielectric permittivity of the materials on either side of the graphene sheet. We define the depolarization field as  $\vec{E}_d(\vec{r}, t) = -\vec{\nabla}\phi(\vec{r}, t)$ . So taking the gradient with respect to  $r$  of Equation 5.8 and substituting in  $E_d$ , we have

$$\begin{aligned} E_d(\vec{r}, t) &= - \int \frac{d^3\vec{r}'}{4\pi\epsilon} \vec{\nabla}_{\vec{r}} \frac{1}{|\vec{s}|} \rho(\vec{r}', t) \\ E_d(\vec{r}, t) &= \int \frac{d^3\vec{r}'}{4\pi\epsilon} \frac{\vec{s}}{|\vec{s}|^3} \rho(\vec{r}', t). \end{aligned} \quad (5.9)$$

where we define the separation vector  $\vec{s} = \vec{r} - \vec{r}'$ . By the charge continuity equation, we relate the charge in the graphene to the sheet current,

$$\vec{\nabla}_{\vec{r}'} \cdot \vec{K}(\vec{r}', t) = -\frac{\partial\rho(\vec{r}', t)}{\partial t}. \quad (5.10)$$

Taking a partial derivative with respect to time of Equation 5.9 and plugging in Equation 5.10, we have

$$\frac{\partial E_d(\vec{r}, t)}{\partial t} = - \int \frac{d^2\vec{r}'}{4\pi\epsilon} \frac{\vec{s}}{|\vec{s}|^3} \vec{\nabla}_{\vec{r}'} \cdot \vec{K}(\vec{r}', t). \quad (5.11)$$

Next, we integrate by parts to arrive at

$$\frac{\partial E_d(\vec{r}, t)}{\partial t} = \int \frac{d^2\vec{r}'}{4\pi\epsilon} \left( \vec{K}(\vec{r}', t) \cdot \vec{\nabla}_{\vec{r}'} \right) \frac{\vec{s}}{|\vec{s}|^3}. \quad (5.12)$$

As with any integration by parts, there is an additional boundary term, which in this case is a contour integral at  $|\vec{s}| = \infty$  that goes to zero. By decomposing the vectors

in Equation 5.12 into Cartesian components, distributing, performing the derivatives, and rearranging, we simplify this expression to,

$$\begin{aligned}\frac{\partial E_d(\vec{r}, t)}{\partial t} &= - \int \frac{d^2\vec{r}'}{4\pi\epsilon} \left[ \frac{\vec{K}(\vec{r}', t)}{|\vec{s}|^3} - \frac{3\vec{s}(\vec{s} \cdot \vec{K}(\vec{r}', t))}{|\vec{s}|^5} \right] \\ \frac{\partial E_d(\vec{r}, t)}{\partial t} &= - \int \frac{d^2\vec{r}'}{4\pi\epsilon} \frac{1}{|\vec{s}|^3} \left[ \mathbb{1} - \frac{3\vec{s} \otimes \vec{s}}{|\vec{s}|^2} \right] \cdot \vec{K}(\vec{r}', t)\end{aligned}\quad (5.13)$$

where  $\mathbb{1}$  is the identity matrix, and  $\otimes$  is a tensor product.

Allowing the tensor  $\vec{f}(\vec{r} - \vec{r}') = [\mathbb{1} - 3\vec{s} \otimes \vec{s}/|\vec{s}|^2]/|\vec{s}|^3$ , the depolarization field can be related to the current density by,

$$\frac{\partial \vec{E}_d(\vec{r}, t)}{\partial t} = \frac{-1}{4\pi\epsilon_{\text{avg}}} \int d^2\vec{r}' \vec{f}(\vec{r} - \vec{r}') \cdot \vec{K}(\vec{r}', t) \quad (5.14)$$

$\vec{f}(\vec{r} - \vec{r}')$  is related to the Green's function that relates the field to the polarization density and can be computed for more complicated geometries than considered in this work.

We see from Equation 5.7 that if  $(\sigma(\omega=0)/\tau_D)\partial\vec{E}_d/\partial t$  equals  $-\Omega_p^2\vec{K}$ , then in the absence of  $E_{\text{inc}}$  and dissipation the current density will oscillate at the frequency  $\Omega_p$ . Comparing with Equation 5.14, it follows that the current density associated with the plasmon mode satisfies the following eigenvalue equation,

$$\frac{\sigma(\vec{r}, \omega=0)}{4\pi\epsilon_{\text{avg}}\tau_D} \int d^2\vec{r}' \vec{f}(\vec{r} - \vec{r}') \cdot \vec{K}(\vec{r}') = \Omega_p^2 \vec{K}(\vec{r}) \quad (5.15)$$

The above equation can be solved for the current densities  $\vec{K}_m$  and frequencies  $\Omega_{pm}$  associated with the plasmon modes in any graphene structure. The modes satisfy the orthogonality condition,  $\int d^2\vec{r} \vec{K}_m(\vec{r}) \cdot \vec{K}_p(\vec{r})/\sigma(\vec{r}, \omega=0) \propto \delta_{mp}$ . For the case of bulk plasmons, Equation 5.15 reproduces the result in Equation 5.6. Solving the eigenvalue equation numerically for the case of a single infinitely long graphene strip, we obtain

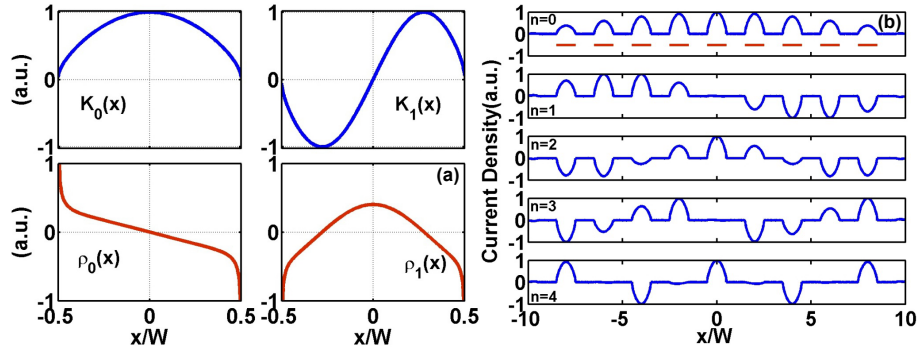


Figure 5.7: (a) The computed current densities  $K(x)$  (top) and charge densities  $\rho(x)$  (bottom) for the lowest two plasmon modes of a graphene strip are plotted. (b) The computed current densities are plotted for the first 5 supermodes of an array consisting of 9 graphene strips ( $W=S$ ). Locations of the strips are indicated by the red horizontal lines.

the following result for the frequency of the lowest two plasmon modes,

$$\Omega_{p0} \approx \sqrt{\frac{\sigma(\omega=0)1.156}{\epsilon_{\text{avg}}\tau_D W}}, \quad \Omega_{p1} \approx \sqrt{\frac{\sigma(\omega=0)2.751}{\epsilon_{\text{avg}}\tau_D W}} \quad (5.16)$$

The computed current and charge densities for the lowest two plasmon modes are shown in Figure 5.7(a). Although all even plasmon modes (0, 2, 4...) will couple with normally incident radiation, only the lowest plasmon mode will couple appreciably. The scaling of the plasmon frequency with  $1/\sqrt{W}$  is in perfect agreement with our data. For the case  $W = 1 \mu\text{m}$ , using Equation 5.16 and the extracted values of  $\sigma(\omega=0)$  and  $\tau_D$ ,  $\omega_{p0}$  is  $\sim 211 \text{ cm}^{-1}$ . The eigenvalue equation more accurately models the plasma resonance than Equation 5.6 (with  $q=\pi/W$ ), but it still overestimates the measured resonance frequency by  $\sim 6.5\%$ . We next address possible origins of this remaining discrepancy.

## 5.2.4 Graphene Plasmon Interactions

Interactions among plasmon modes in neighboring strips can be included by solving Equation 5.15 using  $\sigma(\vec{r}, \omega=0)$  appropriate for an array of graphene strips. Interac-

tions lift the degeneracy among strips and result in a band of plasmon modes that are the supermodes of the array. The computed current density for the lowest five supermodes of an array containing nine strips is shown in Figure 5.7(b). Only the lowest supermode couples appreciably to the normally incident radiation, and it is the frequency of this supermode that is measured in our transmission experiments. Unfortunately, the matrix eigenvalue equation obtained from Equation 5.15 is not sparse, so obtaining solutions for large arrays is computationally prohibitive. Starting from the lowest plasmon mode of a single strip, perturbation technique can be used to obtain an expression for the frequency  $\Omega_p(n, N)$  and the current density  $\vec{K}(n, N)(\vec{r})$  of the  $n$ th supermode ( $n=0\dots N-1$ ) of an  $N$ -strip array,

$$\Omega_p^2(n, N) \approx \Omega_{p0}^2 \left( 1 - 2\Delta_1 \cos \left( \pi \frac{n+1}{N+1} \right) \right) \quad (5.17)$$

$$\vec{K}(n, N)(\vec{r}) \approx \sum_{j=1}^N \vec{K}_0(\vec{r} - j(S+W)\hat{x}) \sin \left( \pi j \frac{n+1}{N+1} \right) \quad (5.18)$$

where  $\Delta_1$  is the first nearest neighbor interaction parameter. Including second nearest neighbor interactions,  $\Omega_p^2(0, \infty) = \Omega_{p0}^2 (1 - 2\Delta_1 - 2\Delta_2)$ .  $\Delta_1$  and  $\Delta_2$  are given by the expression,

$$\Delta_\theta = - \frac{\int d^2\vec{r} \int d^2\vec{r}' \vec{K}_0(\vec{r}) \cdot \vec{f}(\vec{r} - \vec{r}') \cdot \vec{K}_0(\vec{r}' - \theta(S+W)\hat{x})}{\int d^2\vec{r} \int d^2\vec{r}' \vec{K}_0(\vec{r}) \cdot \vec{f}(\vec{r} - \vec{r}') \cdot \vec{K}_0(\vec{r}')} \quad (5.19)$$

Figure 5.8 shows the the calculated values of  $\Omega_p^2(0, \infty)$  as function of the strip spacing  $S$  assuming first and second nearest neighbor interactions. The plasmon frequency is reduced as a result of the interactions among neighboring strips effectively reducing the depolarization field. For example, for  $S=W=1 \mu\text{m}$ , the decrease in the value of  $\Omega_{p0}$  compared to  $\Omega_p(0, \infty)$  due to mode coupling is predicted to be  $\sim 7\%$ . To test these predictions, we performed Far-IR spectroscopy on arrays of graphene plasmonic

strips with varying spacing. Figure 5.8 also displays data sets of plasma resonance frequencies extracted from two samples with arrays of  $1 \mu\text{m}$  strips spaced by  $S = 0.5, 0.75, 1, 2,$  and  $3 \mu\text{m}$  [180]. This data quantitatively matches the perturbation theory well, indicating that we have captured the relevant physics. For the  $1 \mu\text{m}$  strips of Figure 5.6(a), the perturbation theory predicts  $\Omega_p(0, \infty) \sim 196 \text{ cm}^{-1}$ , which is closer to the measured  $\sim 197 \text{ cm}^{-1}$  than  $\omega_{p0}$  alone. These results suggest that interactions cannot be ignored between nearby graphene plasmonic structures.

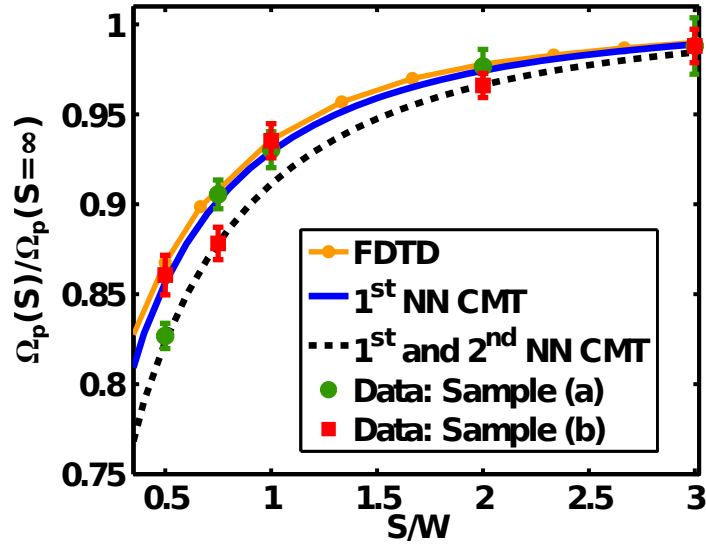


Figure 5.8: The frequencies of the lowest plasmon supermode  $\Omega_p(0, \infty)$  of an infinite graphene strip array calculated using 1st and 2nd nearest neighbor perturbation theory as well as FDTD are plotted as a function of the ratio  $S/W$ . Also shown are data points from two samples measure via Far-IR transmission spectroscopy [180].

The eigenvalue equation does not include retardation effects, which could be important in the case of large arrays, and it also does not account for the discontinuity in the field at the oxide/silicon interface (screening by the silicon substrate). A technique is needed that incorporates these effects, can be used to determine the accuracy of Equation 5.15, and can also compute the measured transmission spectra more accurately than Equation 5.5. For example, Equation 5.5 predicts  $T_{\xi=0}(\omega = 0) = T_{\xi=1}(\omega = \Omega_p)$ , but the measured values in Figure 5.6 differ by  $\sim 1.5\%$ .

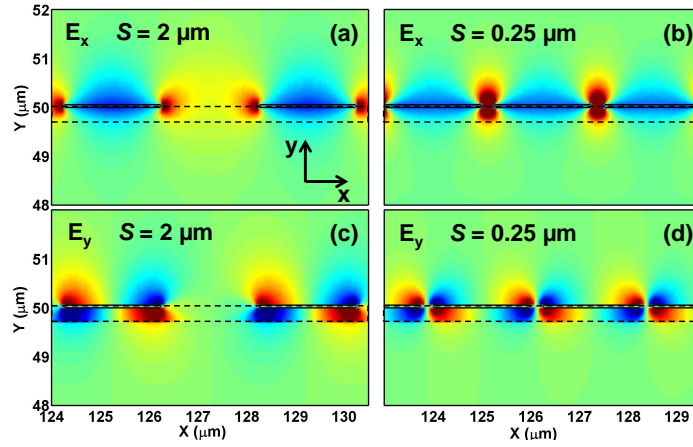


Figure 5.9: FDTD simulation results are shown for the  $x$ - (a,b) and  $y$ - (c,d) components of the electric fields for the lowest order plasmon supermode in two  $W = 2 \mu\text{m}$  arrays of graphene strips ( $S = 2 \mu\text{m}$  (a,c),  $S=0.25 \mu\text{m}$  (b,d)). The dashed lines indicate the locations of the silicon/oxide and oxide/air interfaces.

The discrepancy arises because the transmission through the gaps in the strip array cannot be modeled simply with a fill-factor  $f$ , especially when the incident radiation is polarized perpendicular to the strips and  $S \leq W$ .

### 5.2.5 Finite-Difference Time-Domain Simulation

In the FDTD method, Maxwell's equations are stepped in time. In order to model plasmons, we include an auxiliary equation for the graphene current density (Eq.5.7 without the extra time-derivative) and step the equations using Yee's leap-frogging algorithm[181]. This approach naturally handles interactions and electromagnetic retardation. A challenge in the FDTD technique is the range of length scales important to the problem. The radiation frequencies of interest have free-space wavelengths extending up to  $300 \mu\text{m}$ , but the corresponding plasmon wavelengths are on the order of  $1 \mu\text{m}$ . Furthermore, it is important for the modeled graphene thickness to be much less than the plasmon wavelength. Therefore, the length scales of importance span three orders of magnitude, necessitating a highly non-uniform mesh, with

grid steps varying from  $0.01 - 0.5 \mu\text{m}$ . The computational domain spans more than  $200 \times 200 \mu\text{m}^2$ , and is surrounded by perfectly-matched layer boundaries[181]. We use the values  $4\epsilon_0$  and  $12\epsilon_0$  for the THz dielectric constants of  $\text{SiO}_2$  and Si, respectively. Plasmonic structures are excited at zero angle of incidence with a broadband (0.5-15 THz) pulse of electromagnetic radiation. The transmission spectra for fields polarized parallel and perpendicular to the strips are obtained by Fourier-transforming the time-domain transmitted pulse. Values of  $\sigma(\omega = 0)$  and  $\tau_D$  used in the simulations were iteratively improved until the simulated transmission spectra for both polarizations optimally fit the measured spectra.

The FDTD simulation results, shown in Figure 5.6, accurately fit the measurements. Extracted values of  $\sigma(\omega = 0)$  and  $\tau_D$  lie in the range 0.91-0.95 mS and 29.5-31.5 fs, respectively. Using the expression for the graphene conductivity in Ref. [146], these values correspond to doping densities of  $5.0 - 5.2 \times 10^{12} \text{ cm}^{-2}$ , consistent with the densities determined using the Raman technique. Small variations in the parameters across the CVD graphene sample are consistent with those measured by terahertz spectroscopy in similar samples[182]. The ability of the FDTD technique to quantitatively fit the depth and width of the plasmon resonances, while also predicting their center frequencies to an accuracy within one percent, underscores its usefulness as a tool for modeling graphene plasmonic structures.

The computed  $x$ - and  $y$ -components of the electric field for the lowest plasmon supermode are shown in Fig.5.9 for arrays of graphene strips with two different spacings ( $S=2, 0.25 \mu\text{m}$  and  $W=2 \mu\text{m}$ ). The locations of the graphene strips are indicated by the thin black lines at  $y = 50 \mu\text{m}$ . The dashed lines indicate the locations of the silicon/oxide and oxide/air interfaces. The field is highly localized near the graphene sheet, extending a distance on the order of the plasmon wavelength. The discontinuity in the normal ( $y$ ) component of the field at the silicon/oxide interface is also

visible. In contrast with the  $S = 2.0 \mu\text{m}$  case, when  $S = 0.25 \mu\text{m}$ , the field in the gaps between strips is stronger than the field in the center of the strips. This effect helps to reveal the physical origins of the interaction between neighboring strips. The plasmon charge density that accumulates at the edges of an isolated strip generates a depolarization field  $\vec{E}_d$  with  $\Omega_{p0}^2 \propto |\vec{E}_d|$ . In a strip array, this edge charge density is partially imaged on the neighboring strips, as depicted in Figure 5.5(a). This effect increases the depolarization field in the gaps between strips but reduces the field within each strip. Equivalently, the depolarization fields from neighboring strips are in-phase in the gaps between strips but out-of-phase in their centers. Therefore,  $\Omega_p(0, \infty) < \Omega_{p0}$ . In contrast, in the highest supermode of the array, the current density oscillations in neighboring strips are out of phase, so  $\Omega_p(N, \infty) > \Omega_{p0}$ .

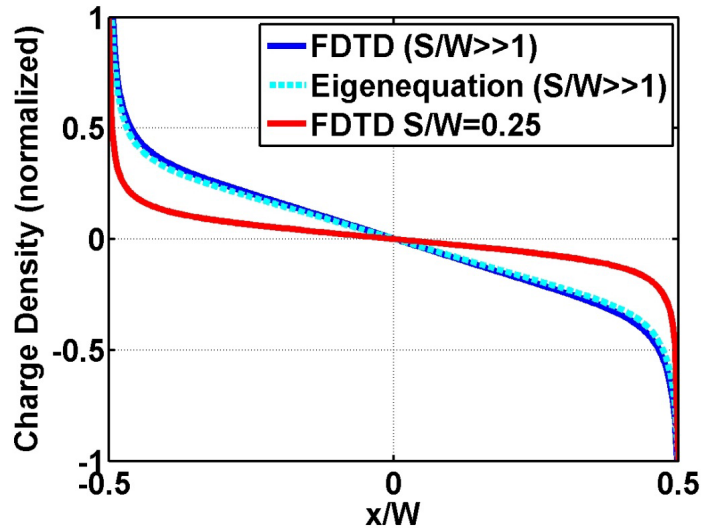


Figure 5.10: The computed charge densities for the lowest plasmon mode in an isolated graphene strip ( $S/W \gg 1$ ) and in an array of strips with  $S/W = 0.25$  are plotted. The charge densities were computed using FDTD ( $S/W \gg 1$  and  $S/W = 0.25$ ) and the eigenvalue equation (Equation 5.15) ( $S/W \gg 1$ ).

One aspect of the supermode oscillation that is well-captured by the FDTD simulation is the plasmon charge density. Figure 5.10 shows the FDTD-computed charge density in a strip for the lowest-order supermode with  $S/W \gg 1$  and  $S/W = 0.25$ . Also

shown is the charge density obtained by solving Equation 5.15 for  $S/W \gg 1$ , which is nearly identical to the FDTD result. But when  $S/W \ll 1$ , the FDTD calculation reveals that the charge density is significantly modified as a result of interactions; the charge density increases near the strip edges to screen the fields of the neighboring strips. Since the perturbation theory assumed that the charge and current densities are unmodified from the lowest plasmon mode of an isolated strip, the results become less accurate when  $S/W \ll 1$ . The good agreement obtained between the FDTD method and the analytic model for  $S/W > 1$  suggests that retardation effects do not play a significant role in the structures considered in this work.

### 5.2.6 Outlook

We presented experimental and theoretical results for the confined plasmon modes in graphene microstructures. We presented an analytic model which captures the essential physics and gives an eigenvalue equation for computing plasmon modes. We also presented a universally applicable FDTD technique. The theoretical models presented show good agreement with the measurements, and demonstrate the importance of interactions in plasmonic structures. This work, to the best of our knowledge, is the first time that theoretical and numerical models have been presented and tested against experiments for confined plasmon modes in graphene microstructures in a quantitative way. This quantitative agreement suggests that models based on classical electrodynamics theory are accurate for practical simulations of these devices. The techniques presented in this paper can be used to understand, model, and design complex graphene plasmonic structures for applications ranging from IR detectors and chemical sensors to plasmonic radiation sources, oscillators, modulators, and metamaterials. But the remaining challenges for the creation of practical devices is the quality, or Q-factor, of the resonators as measured by the scattering time,  $\tau_D$ .

This is a problem that requires high quality graphene material, transfer, etching, and doping. While high quality (at room temperature) graphene devices have been fabricated (e.g. on Boron nitride substrates [183]), they have primarily been based on exfoliated materials. There is the need for high quality, large-scale, scalable materials, substrates, dopants, and processes that can lead to the practical implementation of the tunable THz and infrared applications listed above.

# Chapter 6

## Terahertz Emission from Silicon Carbide

### 6.1 Introduction

Silicon Carbide (SiC) is a wide bandgap semiconductor possessing high mechanical stability, chemical stability, and thermal conductivity. As a result, it is a promising candidate for high-field and high-power electronics[184, 185]. Recently, SiC has also been explored for terahertz (THz) applications. Electrically-pumped THz emitters based on electronic transitions between impurity states have been demonstrated[186]. SiC devices, such as IMPATT oscillators, are also being explored for high power applications in the low THz region[187].

In this Chapter, we present results on the emission of coherent terahertz (THz) radiation from semi-insulating 6H-SiC excited with near-IR femtosecond optical pulses. Broadband THz generation and detection in semiconductors with femtosecond (fs) optical pulses is a powerful and well-studied mechanism with applications in spectroscopy, imaging, and sensing[29]. Many semiconductors, such as GaAs and InAs, emit coherent broadband THz pulses upon excitation with femtosecond optical pulses

due to free-carrier generation and subsequent carrier dynamics in internal or externally applied electric fields[26, 29]. 6H-SiC has a large spontaneous polarization and, therefore, a large permanent bulk electric field [188]. However, the large indirect bandgap of SiC ( $>3$  eV[189, 190]) implies that free-carrier generation via direct interband absorption is not possible for ultrafast pump lasers operating around 800 nm. Free-carrier generation through two-photon or defect absorption is possible. A nonlinear mechanism, such as optical rectification[29], can also be responsible for the generation of THz radiation. The nonlinear optical properties of various SiC polytypes have been previously studied, and 6H-SiC is known to have a large second-order nonlinear susceptibility [189, 191] comparable to crystals such as lithium niobate ( $\chi_{zzz}^{(2)} \sim -60$  pm/V [32]) and ZnTe ( $\chi_{xyz}^{(2)} \sim 90$  pm/V [192]). In this paper, we study the THz radiation dependence on the optical pump polarization, the pump angle of incidence, and the pump power. We show that second order optical nonlinearity, and not free-carrier dynamics, is responsible for THz emission. Given its material hardness, high optical damage threshold, small optical losses, and high optical nonlinearity, SiC is promising for generating broadband high power THz radiation.

Much of the material presented in this Section appears in Ref. [193] and was a collaboration between myself, Paul A. George, Jahan Dawlaty, Shriram Shivaraman, Mvs Chandrashekhara, Michael Spencer, and Farhan Rana.

## 6.2 Experiment and Results

We used a mode-locked Ti:Sapphire laser system to produce optical pump pulses with center wavelength 780 nm, duration 90 fs, repetition rate 81 MHz, and pulse energies varying from 1–15 nJ. We controlled the pump polarization angle ( $\theta$ ) with polarizers and a half-waveplate. The samples were vanadium-compensated semi-insulating 6H-SiC (0001) wafer pieces, 380  $\mu\text{m}$  thick, which we mounted vertically such that the

crystals could be rotated about the vertical axis, thus controlling the angle of incidence ( $\phi$ ) of the pump beam. We mechanically chopped the pump beam at 2.5 kHz and focused it onto the sample. The emitted THz radiation was collected in a nitrogen-purged environment with off-axis parabolic mirrors and detected in the time domain by means of a standard electro-optic sampling detection setup with a 1 mm thick (110)-ZnTe crystal[29, 194]. We have observed strong THz pulses with maximum spectral power signal-to-noise ratios better than one thousand and detection-limited bandwidths wider than 3 THz using a 1 second lock-in time constant. Figure 6.1 shows a representative electric field transient and its accompanying spectrum. We will discuss the dip in the spectrum around 1.9 THz below.

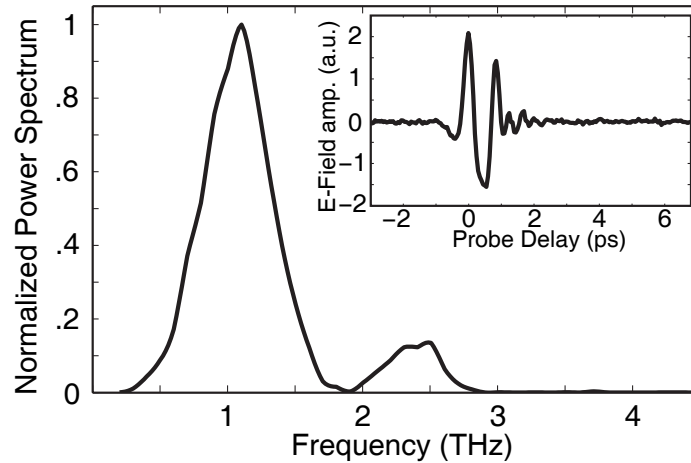


Figure 6.1: Power spectrum of observed electric field. Inset: Observed transient electric field amplitude.

### 6.2.1 Determination of Emission Mechanism

Terahertz emission via the generation and subsequent motion of free-carriers generally has little dependence on the pump polarization or the pump angle of incidence (other than that which is related to the transmission/reflection of the pump and the emitted THz radiation at the crystal interfaces). In contrast, the emission of THz

radiation from nonlinear optical rectification is strongly dependent on the pump polarization and angle of incidence as dictated by the form of the second-order nonlinear susceptibility tensor  $\chi_{ijk}^{(2)}$ [29, 32]. 6H-SiC has 6mm hexagonal crystal symmetry and therefore, under Kleinman's condition, there are only two independent components of  $\chi_{ijk}^{(2)}$ , written[32]

$$\chi_{ijk}^{(2)} = \begin{bmatrix} 0 & 0 & 0 & 0 & \chi_{zxx}^{(2)} & 0 \\ 0 & 0 & 0 & \chi_{zxx}^{(2)} & 0 & 0 \\ \chi_{zxx}^{(2)} & \chi_{zxx}^{(2)} & \chi_{zzz}^{(2)} & 0 & 0 & 0 \end{bmatrix}. \quad (6.1)$$

The nonlinear polarization,  $\vec{P}(\omega)$ , generated by the near-infrared pump pulse,  $\vec{E}(\omega)$ , is related to the second-order nonlinear susceptibility tensor as[29]

$$\vec{P}(\omega) = \epsilon_0 \chi^{(2)}(\omega = \omega_1 - \omega_2) \vec{E}(\omega_1) \vec{E}^*(\omega_2). \quad (6.2)$$

Then the emitted THz-frequency electric field is, in the time domain[29],

$$\vec{E}^{\text{THz}} \propto \frac{\partial^2 \vec{P}(t)}{\partial t^2}. \quad (6.3)$$

Following the analysis of Chen *et al.*[194], we calculate the expected dependence of the THz E-field amplitude on the pump polarization and angle of incidence as follows, including the dependence of the detection on the THz polarization. From Equations 6.1 and 6.2, we can express the induced nonlinear polarization vector rel-

ative to the SiC crystal orientation[32, 194]:

$$\begin{bmatrix} P_x \\ P_y \\ P_z \end{bmatrix} = \epsilon_0 \begin{bmatrix} 0 & 0 & 0 & 0 & \chi_{zxx}^{(2)} & 0 \\ 0 & 0 & 0 & \chi_{zxx}^{(2)} & 0 & 0 \\ \chi_{zxx}^{(2)} & \chi_{zxx}^{(2)} & \chi_{zzz}^{(2)} & 0 & 0 & 0 \end{bmatrix} \begin{bmatrix} E_x^2 \\ E_y^2 \\ E_z^2 \\ 2E_y E_z \\ 2E_x E_z \\ 2E_x E_y \end{bmatrix} \quad (6.4)$$

$$\begin{bmatrix} P_x \\ P_y \\ P_z \end{bmatrix} \propto \begin{bmatrix} 2\chi_{zxx}^{(2)} E_x E_z \\ 2\chi_{zxx}^{(2)} E_y E_z \\ \chi_{zxx}^{(2)} E_x^2 + \chi_{zxx}^{(2)} E_y^2 + \chi_{zzz}^{(2)} E_z^2 \end{bmatrix} \quad (6.5)$$

Here, the  $x$ - $y$  plane is the hexagonal plane of the SiC crystal, and the  $z$  direction is parallel to the  $c$ -axis of the SiC crystal (i.e. perpendicular to the hexagonal plane). We define the pump electric field pulse as traveling in the  $z'$  direction before entering the SiC crystal, with a linear polarization angle  $\theta$  somewhere in the  $x'$ - $y'$  plane, where the primed coordinates indicate the lab reference frame:  $\vec{E}' = E_0(\cos(\theta), \sin(\theta), 0)$ . It is clear from Equation 6.5 that due the crystal symmetry, pumping at normal incidence ( $E_z = 0$ ) would result in  $P_x = P_y = 0$  and no THz emission in the  $z$  direction.

Generally, the pump is incident on the SiC crystal at an angle of  $\phi$ , so we transform the field components to the SiC crystalline frame, including refraction from Snell's Law, and compute the orientation and amplitude of the induced nonlinear polarization as in Equation 6.5. The experimental apparatus was aligned such that the detected THz field is proportional to the component of the nonlinear polarization perpendicular

to the pump propagation direction:

$$\vec{E}_{\text{THz}} \propto \hat{k} \times \vec{P} \times \hat{k} \quad (6.6)$$

where  $\hat{k}$  is the unit vector parallel to the pump propagation direction. Finally, we compute the polarization dependence of the transmission of the THz from SiC into air, as well as the THz polarization dependence of the detection using electro-optic sampling by the Pockels effect in (110) ZnTe[194]. The result of these calculations is an estimate of the relative electro-optic sampling signal as a function of polarization angle  $\theta$ , angle of incidence  $\phi$ , and the ratio  $\chi_{zzz}^{(2)}/\chi_{zxx}^{(2)}$ .

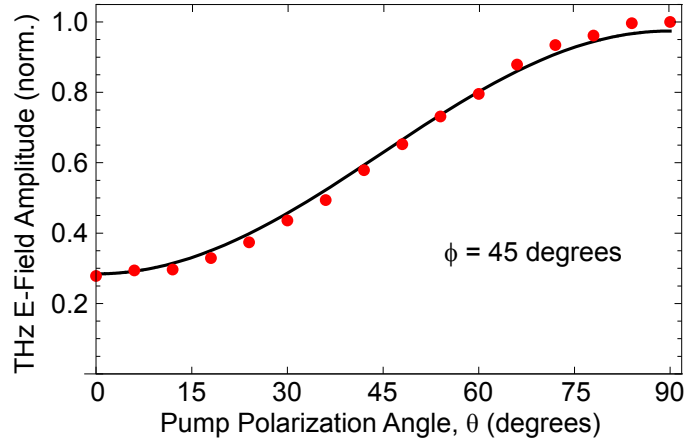


Figure 6.2: Normalized peak-to-peak electric field versus excitation polarization, with angle of incidence  $\phi = 45$  degrees. 0 degrees corresponds to TE polarization, 90 degrees to TM. Fit with  $\chi_{zzz}^{(2)}/\chi_{zxx}^{(2)} = -3.0$ .

Figure 6.2 shows experimental results for the dependence of the THz E-field amplitude on the pump polarization while the pump angle of incidence is 45 degrees. The corresponding theoretical curve is also shown, calculated following the analysis above. The E-field amplitude shows a strong dependence on the pump polarization and there is a good fit of the optical rectification theory to the experimental data. The ratio of  $\chi_{zzz}^{(2)}/\chi_{zxx}^{(2)}$  is the only fitting parameter, and the fit in Figure 6.2 corresponds

to a value of  $\chi_{zzz}^{(2)}/\chi_{zxx}^{(2)} = -3.0$ .

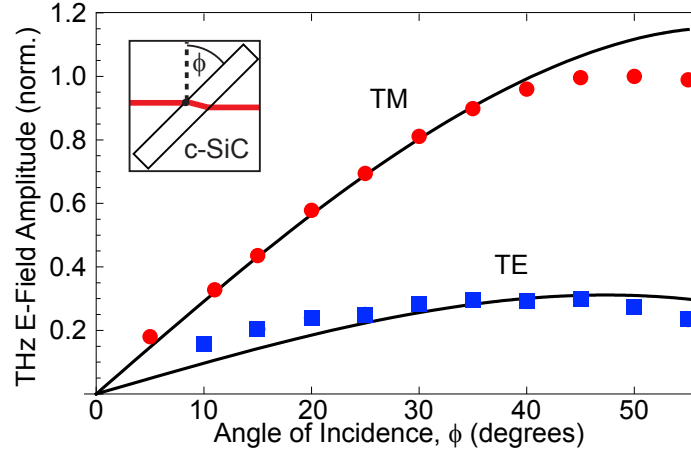


Figure 6.3: Normalized peak-to-peak electric field versus angle of incidence for TE (filled square) and TM (filled circle) pump polarizations.

To further confirm the optical rectification process, we study the THz E-field amplitude dependence on the pump angle of incidence. The experimental results for TE and TM pump polarizations are shown in Figure 6.3 along with the theoretical curves. The theory fits the data well. As expected from the form of  $\chi_{ijk}^{(2)}$ ,  $E_{\text{THz}}$  approaches zero at small  $\phi$ . The discrepancies that we observe at extreme angles of incidence can be a result of non-ideal phase matching and reduced collection efficiencies (discussed later).

For a second order nonlinear emission process, the terahertz field amplitude is expected to be proportional to the pump power. In Figure 6.4, we plot the maximum THz pulse amplitude versus the pump pulse energy. The observed linear dependence agrees with THz generation via optical rectification. For comparison, we plot the amplitude of THz emission from a 1 mm thick (110) ZnTe crystal at normal incidence, adjusted for crystal length. The evidence given by the THz emission amplitude dependence on  $\theta$ ,  $\phi$ , and pump pulse energy all unambiguously indicate that the mechanism responsible for THz emission in SiC is nonlinear optical rectification.

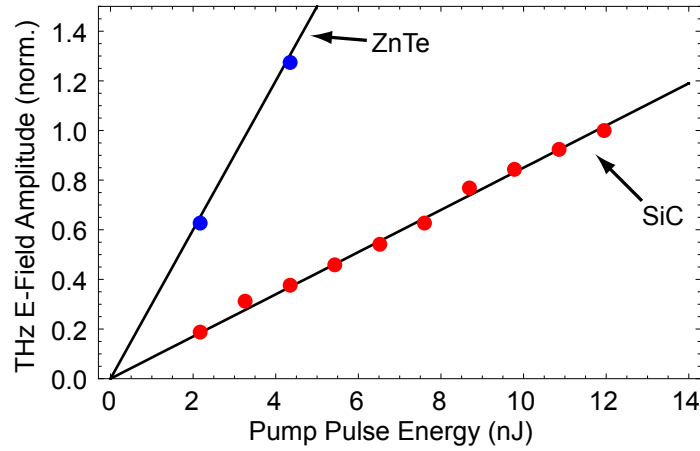


Figure 6.4: Normalized peak-to-peak electric field versus excitation pulse energy (at 780 nm) for SiC ( $\phi = 45^\circ$ ) and ZnTe (normal incidence).

### 6.2.2 The Ratio of Nonlinear Susceptibility Components

The ratio of  $\chi_{zzz}^{(2)}/\chi_{zxx}^{(2)}$ , the fitting parameter used in Figures 6.2 and 6.3, has been the subject of several investigations (see Table 6.1). The theoretically predicted value of this ratio is exactly -2 for cubic 3C-SiC and varies between -0.5 and -2.0 for  $n$ H-SiC (with  $2 \leq n \leq \infty$ ). To date, the measured values of this ratio have been found to be much larger than the predicted values. Our measurements of the TM/TE ratio at  $\phi = 40$  degrees yielded a value of  $\chi_{zzz}^{(2)}/\chi_{zxx}^{(2)}$  equal to  $-3.0$  with a 95% confidence interval of  $\pm 2.6$ . Table 6.1 shows that our measured value of  $\chi_{zzz}^{(2)}/\chi_{zxx}^{(2)}$  is the closest to the theoretical values among reported results for 6H-SiC.

### 6.2.3 Refractive Index and Phase Matching

To study the efficacy of THz emission, we present measurements of the complex index of refraction of SiC at THz frequencies (see Figure 6.5). This data was obtained by transmitting broadband THz pulses generated with a photoconductive antenna through our samples in a static transmission measurement. We then extract the complex refractive index as we describe in Section 2.4, using Equation 2.10. We see

6H-SiC		$\chi_{zzz}^{(2)}/\chi_{zxx}^{(2)}$	$\chi_{zzz}^{(2)}$	$\chi_{zxx}^{(2)}$
Theory	Wu <i>et al.</i> [195]	-1.89	38.6	-20.4
	Adolph <i>et al.</i> [196]	-1.85	18.1	-9.8
	Rashkeev <i>et al.</i> [197]	-1.84	17.8	-9.7
	Chen <i>et al.</i> [198]	-1.84	27.6	-15.0
Exp.	Lundquist <i>et al.</i> [189]	-10	86	-8.6
	Niedermeier <i>et al.</i> [191]	-6	24±10	-4±2
	This work	-3.0±2.6		

Table 6.1: Summary of calculated (Refs. [195],[196],[197],[198]) and measured (Refs. [189], [191]) values of the ratio  $\chi_{zzz}^{(2)}/\chi_{zxx}^{(2)}$ . Tensor elements  $\chi_{zzz}^{(2)}$  and  $\chi_{zxx}^{(2)}$  (in units of pm/V) are included for reference. The measured value from this work is in close agreement with theoretical values to date.

that SiC is nearly dispersionless in the low THz range, with an index of refraction  $n = 3.0$ . Also, power absorption,  $\alpha$ , is small.

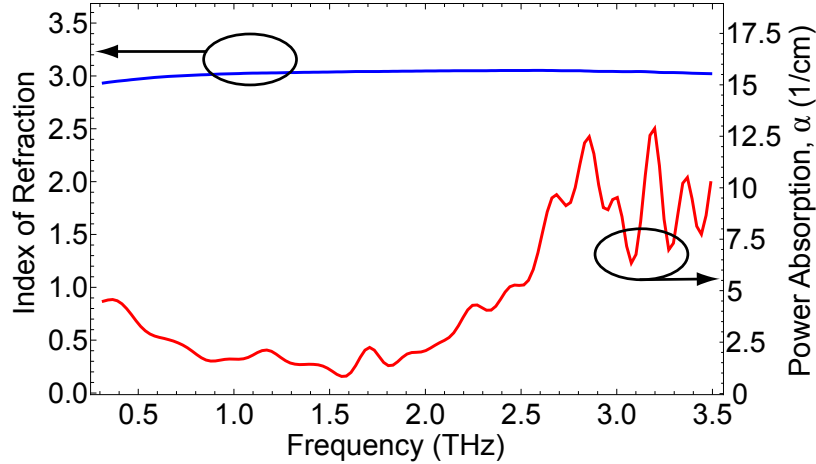


Figure 6.5: Index of refraction and power absorption of SiC versus frequency at 300K.

Since the group index of SiC at 780 nm is  $n_{\text{opt}}^{\text{gr}} \approx 2.72$ [199], there is non-ideal phase matching between the pump pulse and THz waves. The coherence length is  $l_c = \pi/\Delta k \approx 0.54$  [mm THz]/ $f$  [THz] in the measured range, where  $\Delta k = \omega(n_{\text{THz}} - n_{\text{opt}}^{\text{gr}})/c$  and  $f$  is the frequency[200]. The non-ideal phase matching could explain the discrepancy between theory and experiment at extreme angles in Figure 6.3. At large  $\phi$  angles, total internal reflection of the emitted THz radiation cone becomes significant.

Furthermore, since the THz radiation is not strictly collimated with the pump beam, a small amount of THz radiation is detectable even at angles near zero. The spectrum for difference frequency generation under non-ideal phase matching conditions is known to depend on the frequency[32]. Specifically,  $E_{\text{THz}}(\omega) \propto \sin(\Delta kL/2)/(\Delta kL/2)$ . According to this relation, the first zero in the spectrum should occur around 2 THz. Figure 6.1 shows that the measured THz spectrum is in good agreement with the predictions.

### 6.3 Phase Matching for Efficient THz Generation

We have demonstrated broadband coherent THz emission from SiC by optical rectification. THz emission via optical rectification has been well studied in zinc blende crystals with cubic symmetries, such as GaAs and ZnTe[25, 194], as well as in crystals of trigonal (lithium niobate[201]) and  $\bar{6}m2$  hexagonal (GaSe[202]) symmetries. Among these alternatives, ZnTe stands out as being particularly well phase-matched for THz generation[200], and as such it is a popular crystal used for this purpose. Unfortunately, large phonon absorption within ZnTe prevents THz emission above  $\sim 3$  THz. Given SiC's higher optical damage threshold[190], comparable second order nonlinear susceptibility, robust mechanical properties, large phonon energy, and large direct bandgap ( $>5$  eV for 6H-SiC), it could prove to be a useful source of broadband THz radiation.

There are a couple of methods used to improve phase matching for high-efficiency THz emission in semiconductors. One option is periodic poling, which is a standard technique in nonlinear optics based on engineering a stack of alternately oriented crystals[32]. This technique has been applied to THz generation via optical rectification in lithium niobate[203], which is a crystal with a high  $\chi_2$  and damage threshold. But a working device can be challenging to fabricate, and the method produces nar-

rowband radiation. An alternate method to achieve phase matching for THz emission is with a tilted optical pulse front[201]. A tilted optical pump pulse front (achieved with a grating) can meet the phase matching condition  $\Delta k = 0$  with a THz beam emitted at an angle within the crystal. Then, with large optical powers, large THz pulse powers are possible, limited only by the dispersion of the crystal and the grating efficiency. The group of K. A. Nelson has used this technique with lithium niobate to great effect (see, e.g., [204, 205, 206]), which requires a tilt angle of  $\sim 64^\circ$ [201]. SiC has low THz absorption and dispersionless index of refraction in the 0.5-3.5 THz range, and since  $n_{\text{THz}}$  and  $n_{\text{opt}}^{\text{gr}}$  are relatively close in SiC, phase matching could be achieved with the comparatively small tilted pulse front of  $\sim 25^\circ$  for a 780 nm pump[201]. So SiC may be well-suited for this application, likely with higher bandwidth and than lithium niobate and similar THz pulse energy.

# Bibliography

- [1] C.-H. Jan, M. Agostinelli, H. Deshpande, M.A. El-Tanani, W. Hafez, U. Jalan, L. Janbay, M. Kang, H. Lakdawala, J. Lin, Y.-L. Lu, S. Mudanai, J. Park, A. Rahman, J. Rizk, W.-K. Shin, K. Soumyanath, H. Tashiro, C. Tsai, P. Vandervoorn, J.-Y. Yeh, and P. Bai. Rf cmos technology scaling in high-k/metal gate era for rf soc (system-on-chip) applications. In *Electron Devices Meeting (IEDM), 2010 IEEE International*, pages 27.2.1–27.2.4, Dec 2010.
- [2] Dayou Qian, Ezra Ip, Ming-Fang Huang, Ming jun Li, Arthur Dogariu, Shao-liang Zhang, Yin Shao, Yue-Kai Huang, Yequn Zhang, Xilin Cheng, Yue Tian, Philip Ji, Adam Collier, Ying Geng, Jesus Linares, Carlos Montero, Vicente Moreno, Xesus Prieto, and Ting Wang. 1.05pb/s transmission with 109b/s/hz spectral efficiency using hybrid single- and few-mode cores. In *Frontiers in Optics 2012/Laser Science XXVIII*, page FW6C.3. Optical Society of America, 2012.
- [3] Amazon web services. <http://aws.amazon.com/big-data/>. Accessed: 2014-10-30.
- [4] R. W. Coons, D. Campos, M. Crank, S. S. Harilal, and A. Hassanein. Comparison of euv spectral and ion emission features from laser-produced sn and li plasmas. *Proc. SPIE*, 7636:763636, 2010.
- [5] Peter H. Siegel. Terahertz technology. *IEEE Transactions on Microwave Theory and Techniques*, 50(3):910–928, 2002.
- [6] Masayoshi Tonouchi. Cutting-edge terahertz technology. *Nature Photonics*, 1:97–105, 2007.
- [7] Shi wei Dong, Zhong-Bo Zhu, and Ying Wang. Advances of terahertz research and terahertz satellite communications. In *Electronics, Communications and Control (ICECC), 2011 International Conference on*, pages 4122–4125, Sept 2011.
- [8] M. S. Dresselhaus. What’s next for low-dimensional materials? *Materials Research Letters*, 2(1):1–9, 2014.

- [9] Charles Kittel. *Introduction to Solid State Physics*. John Wiley & Sons, eighth edition, 2005.
- [10] S.L. Chuang. *Physics of Optoelectronic Devices*. Wiley Series in Pure and Applied Optics. Wiley, 1995.
- [11] John H. Davies. *The Physics of Low-dimensional Semiconductors: An introduction*. Cambridge University Press, Cambridge, UK, 1998.
- [12] Changgu Lee, Xiaoding Wei, Jeffrey W. Kysar, and James Hone. Measurement of the elastic properties and intrinsic strength of monolayer graphene. *Science*, 321(5887):385–388, 2008.
- [13] J. Scott Bunch, Scott S. Verbridge, Jonathan S. Alden, Arend M. van der Zande, Jeevak M. Parpia, Harold G. Craighead, and Paul L. McEuen. Impermeable atomic membranes from graphene sheets. *Nano Letters*, 8(8):2458–2462, 2008.
- [14] S.A. Maier. *Plasmonics: Fundamentals and Applications: Fundamentals and Applications*. Springer, 2007.
- [15] Jon A. Schuller, Edward S. Barnard, Wenshan Cai, Young Chul Jun, Justin S. White, and Mark L. Brongersma. Plasmonics for extreme light concentration and manipulation. *Nature Materials*, 9:193–204, 2010.
- [16] Yihong Yang, Alisha Shutler, and D. Grischkowsky. Measurement of the transmission of the atmosphere from 0.2 to 2 thz. *Optics Express*, 19(9):8830–8838, Apr 2011.
- [17] Benjamin S. Williams. Terahertz quantum-cascade lasers. *Nature Photonics*, 1:517–525, 2007.
- [18] D. A. G. Deacon, L. R. Elias, J. M. J. Madey, G. J. Ramian, H. A. Schwettman, and T. I. Smith. First operation of a free-electron laser. *Phys. Rev. Lett.*, 38:892–894, Apr 1977.
- [19] Jefferson lab free electron laser. <https://www.jlab.org/free-electron-laser>. Accessed: 2014-10-30.
- [20] D. Molter, M. Theuer, and R. Beigang. Nanosecond terahertz optical parametric oscillator with a novel quasi phase matching scheme in lithium niobate. *Opt. Express*, 17(8):6623–6628, Apr 2009.
- [21] Teraphysics traveling wave tube. <http://www.teraphysics.com/index.php>. Accessed: 2014-10-30.
- [22] Brian C. Smith. *Fundamentals of Fourier Transform Infrared Spectroscopy*. Taylor and Francis, Boca Raton, FL, 2011.

- [23] Albert A. Michelson and Edward W. Morley. On the relative motion of the earth and the luminiferous ether. *American Journal of Science*, 34:333–345, 1887.
- [24] Peter Atkins and Julio De Paula. *Physical Chemistry*. W. H. Freeman and Company, New York, NY, 9 edition, 2009.
- [25] A. Rice, Y. Jin, X. F. Ma, X.C. Zhang, D. Bliss, J. Larkin, and M. Alexander. Terahertz optical rectification from (110) zinc-blende crystals. *Applied Physics Letters*, 64(11):1324–1326, 1994.
- [26] Ping Gu, Masahiko Tani, Shunsuke Kono, Kiyomi Sakai, and X.-C. Zhang. Study of terahertz radiation from inas and insb. *Journal of Applied Physics*, 91(9):5533–5537, 2002.
- [27] D. H. Auston, K. P. Cheung, and P. R. Smith. Picosecond photoconducting hertzian dipoles. *Applied Physics Letters*, 45(3):284–286, 1984.
- [28] N. Katzenellenbogen and D. Grischkowsky. Efficient generation of 380 fs pulses of thz radiation by ultrafast laser pulse excitation of a biased metal-semiconductor interface. *Appl. Phys. Lett.*, 58(3):222–224, 1991.
- [29] K. Sakai. *Terahertz Optoelectronics*. Springer, New York, 2005.
- [30] Paul George. *Terahertz Time-Domain Spectroscopy: From Proteins to Nanostructures*. PhD thesis, Cornell University, 2009.
- [31] Q. Wu and X.C. Zhang. Free-space electro-optic sampling of terahertz beams. *Applied Physics Letters*, 67(24):3523–3525, 1995.
- [32] R. W. Boyd. *Nonlinear Optics*. Academic, New York, 1 edition, 1992.
- [33] H. Haus and J. Melcher. *Electromagnetic Fields and Energy*. Prentice Hall, New York, USA, 1989.
- [34] Z. Vardeny, J. Strait, and J. Tauc. Picosecond trapping of photocarriers in amorphous silicon. *Applied Physics Letters*, 42(7):580–582, 1983.
- [35] C. Thomsen, J. Strait, Z. Vardeny, H. J. Maris, J. Tauc, and J. J. Hauser. Coherent phonon generation and detection by picosecond light pulses. *Phys. Rev. Lett.*, 53:989–992, Sep 1984.
- [36] J. Strait and J. Tauc. Lightinduced defects in hydrogenated amorphous silicon observed by picosecond photoinduced absorption. *Applied Physics Letters*, 47(6):589–591, 1985.
- [37] Matthew C. Beard, Gordon M. Turner, and Charles A. Schmuttenmaer. Transient photoconductivity in gaas as measured by time-resolved terahertz spectroscopy. *Phys. Rev. B*, 62:15764–15777, Dec 2000.

- [38] K. P. H. Lui and F. A. Hegmann. Ultrafast carrier relaxation in radiation-damaged silicon on sapphire studied by optical-pump terahertz-probe experiments. *Applied Physics Letters*, 78(22):3478–3480, 2001.
- [39] R. A. Kaindl, M. A. Carnahan, D. Hagele, R. Lovenich, and D. S. Chemla. Ultrafast terahertz probes of transient conducting and insulating phases in an electronhole gas. *Nature*, 423:734–738, 2003.
- [40] R. A. Kaindl, D. Hägele, M. A. Carnahan, and D. S. Chemla. Transient terahertz spectroscopy of excitons and unbound carriers in quasi-two-dimensional electron-hole gases. *Phys. Rev. B*, 79:045320, Jan 2009.
- [41] Patrick Parkinson, James Lloyd-Hughes, Qiang Gao, H. Hoe Tan, Chennupati Jagadish, Michael B. Johnston, and Laura M. Herz. Transient terahertz conductivity of gaas nanowires. *Nano Letters*, 7(7):2162–2165, 2007.
- [42] D. G. Cooke, F. C. Krebs, and P. U. Jepsen. Direct observation of sub-100 fs mobile charge generation in a polymer-fullerene film. *Phys. Rev. Lett.*, 108:056603, Jan 2012.
- [43] F. A. Hegmann, R. R. Tykwinski, K. P. H. Lui, J. E. Bullock, and J. E. Anthony. Picosecond transient photoconductivity in functionalized pentacene molecular crystals probed by terahertz pulse spectroscopy. *Phys. Rev. Lett.*, 89:227403, Nov 2002.
- [44] Ernst Knoesel, Mischa Bonn, Jie Shan, Feng Wang, and Tony F. Heinz. Conductivity of solvated electrons in hexane investigated with terahertz time-domain spectroscopy. *The Journal of Chemical Physics*, 121(1):394–404, 2004.
- [45] Ronald Ulbricht, Euan Hendry, Jie Shan, Tony F. Heinz, and Mischa Bonn. Carrier dynamics in semiconductors studied with time-resolved terahertz spectroscopy. *Rev. Mod. Phys.*, 83:543–586, Jun 2011.
- [46] Matthew C. Beard, Gordon M. Turner, and Charles A. Schmuttenmaer. Subpicosecond carrier dynamics in low-temperature grown gaas as measured by time-resolved terahertz spectroscopy. *Journal of Applied Physics*, 90(12):5915–5923, 2001.
- [47] Han-Kwang Nienhuys and Villy Sundström. Intrinsic complications in the analysis of optical-pump, terahertz probe experiments. *Phys. Rev. B*, 71:235110, Jun 2005.
- [48] James T. Kindt and Charles A. Schmuttenmaer. Theory for determination of the low-frequency time-dependent response function in liquids using time-resolved terahertz pulse spectroscopy. *The Journal of Chemical Physics*, 110(17):8589–8596, 1999.

- [49] V. Podzorov, M. E. Gershenson, Ch. Kloc, R. Zeis, and E. Bucher. High-mobility field-effect transistors based on transition metal dichalcogenides. *Applied Physics Letters*, 84(17):3301–3303, 2004.
- [50] Andrea Splendiani, Liang Sun, Yuanbo Zhang, Tianshu Li, Jonghwan Kim, Chi-Yung Chim, Giulia Galli, and Feng Wang. Emerging photoluminescence in monolayer mos<sub>2</sub>. *Nano Letters*, 10(4):1271–1275, 2010.
- [51] Kin Fai Mak, Changgu Lee, James Hone, Jie Shan, and Tony F. Heinz. Atomically thin mos<sub>2</sub>: A new direct-gap semiconductor. *Phys. Rev. Lett.*, 105:136805, Sep 2010.
- [52] Goki Eda, Hisato Yamaguchi, Damien Voiry, Takeshi Fujita, Mingwei Chen, and Manish Chhowalla. Photoluminescence from chemically exfoliated mos<sub>2</sub>. *Nano Letters*, 11(12):5111–5116, 2011.
- [53] Youngki Yoon, Kartik Ganapathi, and Sayeef Salahuddin. How good can monolayer mos<sub>2</sub> transistors be? *Nano Letters*, 11(9):3768–3773, 2011.
- [54] Ting Cao, Gang Wang, Wenpeng Han, Huiqi Ye, Chuanrui Zhu, Junren Shi, Qian Niu, Pingheng Tan, Enge Wang, Baoli Liu, and Ji Feng. Valley-selective circular dichroism of monolayer molybdenum disulphide. *Nature Communications*, 3:887, 2012.
- [55] G. Kioseoglou, A. T. Hanbicki, M. Currie, A. L. Friedman, D. Gunlycke, and B. T. Jonker. Valley polarization and intervalley scattering in monolayer mos<sub>2</sub>. *Applied Physics Letters*, 101(22):221907, 2012.
- [56] Arend M. van der Zande, Pinshane Y. Huang, Daniel A. Chenet, Timothy C. Berkelbach, YuMeng You, Gwan-Hyoung Lee, Tony F. Heinz, David R. Reichman, David A. Muller, and James C. Hone. Grains and grain boundaries in highly crystalline monolayer molybdenum disulphide. *Nature Materials*, 12(6):554, 2013.
- [57] Wu Zhou, Xiaolong Zou, Sina Najmaei, Zheng Liu, Yumeng Shi, Jing Kong, Jun Lou, Pulickel M. Ajayan, Boris I. Yakobson, and Juan-Carlos Idrobo. Intrinsic structural defects in monolayer molybdenum disulfide. *Nano Letters*, 13(6):2615–2622, 2013.
- [58] Qing Hua Wang, Kouros Kalantar-Zadeh, Andras Kis, Jonathan N. Coleman, and Michael S. Strano. Electronics and optoelectronics of two-dimensional transition metal dichalcogenides. *Nature Nanotechnology*, (11):699, 2012.
- [59] Han Wang, Lili Yu, Yi-Hsien Lee, Yumeng Shi, Allen Hsu, Matthew L. Chin, Lain-Jong Li, Madan Dubey, Jing Kong, and Tomas Palacios. Integrated circuits based on bilayer mos<sub>2</sub> transistors. *Nano Letters*, 12(9):4674–4680, 2012.

- [60] Masihhur R. Laskar, Lu Ma, Santhakumar Kannappan, Pil Sung Park, Sriram Krishnamoorthy, Digbijoy N. Nath, Wu Lu, Yiyang Wu, and Siddharth Rajan. Large area single crystal (0001) oriented mos<sub>2</sub>. *Applied Physics Letters*, 102(25):252108, 2013.
- [61] Oriol Lopez-Sanchez, Dominik Lembke, Metin Kayci, Aleksandra Radenovic, and Andras Kis. Ultrasensitive photodetectors based on monolayer mos<sub>2</sub>. *Nature Nanotechnology*, 8:497–501, 2013.
- [62] F. K. Perkins, A. L. Friedman, E. Cobas, P. M. Campbell, G. G. Jernigan, and B. T. Jonker. Chemical vapor sensing with monolayer mos<sub>2</sub>. *Nano Letters*, 13(2):668–673, 2013.
- [63] Leandro M. Malard, Thonimar V. Alencar, Ana Paula M. Barboza, Kin Fai Mak, and Ana M. de Paula. Observation of intense second harmonic generation from mos<sub>2</sub> atomic crystals. *Phys. Rev. B*, 87:201401, May 2013.
- [64] Wenjuan Zhu, Tony Low, Yi-Hsien Lee, Han Wang, Damon B. Farmer, Jing Kong, Fengnian Xia, and Phaedon Avouris. Electronic transport and device prospects of monolayer molybdenum disulphide grown by chemical vapour deposition. *Nature Communications*, 5:4087, 2014.
- [65] K. F. Mak, K. L. McGill, J. Park, and P. L. McEuen. The valley hall effect in mos<sub>2</sub> transistors. *Science*, 344(6191):1489–1492, 2014.
- [66] Saptarshi Das, Hong-Yan Chen, Ashish Verma Penumatcha, and Joerg Appenzeller. High performance multilayer mos<sub>2</sub> transistors with scandium contacts. *Nano Letters*, 13(1):100–105, 2013.
- [67] Wenzhong Bao, Xinghan Cai, Dohun Kim, Karthik Sridhara, and Michael S. Fuhrer. High mobility ambipolar mos<sub>2</sub> field-effect transistors: Substrate and dielectric effects. *Applied Physics Letters*, 102(4):042104, 2013.
- [68] R. Fivaz and E. Mooser. Mobility of charge carriers in semiconducting layer structures. *Phys. Rev.*, 163:743–755, Nov 1967.
- [69] Sunkook Kim, Aniruddha Konar, Wan-Sik Hwang, Jong Hak Lee, Jiyoul Lee, Jaehyun Yang, Changhoon Jung, Hyoungsub Kim, and Jae-Young Yoo, Ji-Beom ang Choi. High-mobility and low-power thin-film transistors based on multilayer mos<sub>2</sub> crystals. *Nature Communications*, 3:1011, 2012.
- [70] N. R. Pradhan, D. Rhodes, Q. Zhang, S. Talapatra, M. Terrones, P. M. Ajayan, and L. Balicas. Intrinsic carrier mobility of multi-layered mos<sub>2</sub> field-effect transistors on sio<sub>2</sub>. *Applied Physics Letters*, 102(12):123105, 2013.
- [71] Branimir Radisavljevic and Andras Kis. Mobility engineering and a metal-insulator transition in monolayer mos<sub>2</sub>. *Nature Materials*, 12(9):815, 2013.

- [72] Nardeep Kumar, Jiaqi He, Dawei He, Yongsheng Wang, and Hui Zhao. Charge carrier dynamics in bulk mos[<sub>2</sub>] crystal studied by transient absorption microscopy. *Journal of Applied Physics*, 113(13):133702, 2013.
- [73] Kristen Kaasbjerg, Kristian S. Thygesen, and Karsten W. Jacobsen. Phonon-limited mobility in *n*-type single-layer mos<sub>2</sub> from first principles. *Phys. Rev. B*, 85:115317, Mar 2012.
- [74] Nan Ma and Debdeep Jena. Charge scattering and mobility in atomically thin semiconductors. *Phys. Rev. X*, 4:011043, Mar 2014.
- [75] T. Korn, S. Heydrich, M. Hirmer, J. Schmutzler, and C. Schuller. Low-temperature photocarrier dynamics in monolayer mos[<sub>2</sub>]. *Applied Physics Letters*, 99(10):102109, 2011.
- [76] Jared H. Strait, Parinita Nene, and Farhan Rana. High intrinsic mobility and ultrafast carrier dynamics in multilayer metal dichalcogenide mos<sub>2</sub>. *arXiv:1408.2562*, 2014.
- [77] B. L. Evans and P. A. Young. Optical absorption and dispersion in molybdenum disulphide. *Proc.R. Soc. A*, 284(1398):402–422, 1965.
- [78] Giriraj Jnawali, Yi Rao, Hugen Yan, and Tony F. Heinz. Observation of a transient decrease in terahertz conductivity of single-layer graphene induced by ultrafast optical excitation. *Nano Letters*, 13(2):524–530, 2013.
- [79] H. Peelaers and C. G. Van de Walle. Effects of strain on band structure and effective masses in mos<sub>2</sub>. *Phys. Rev. B*, 86:241401, Dec 2012.
- [80] Ferdows Zahid, Lei Liu, Yu Zhu, Jian Wang, and Hong Guo. A generic tight-binding model for monolayer, bilayer and bulk mos<sub>2</sub>. *AIP Advances*, 3(5):052111, 2013.
- [81] T. Kawamura and S. Das Sarma. Phonon-scattering-limited electron mobilities in al<sub>x</sub>ga<sub>1-x</sub>as/gaas heterojunctions. *Phys. Rev. B*, 45:3612–3627, Feb 1992.
- [82] Tawinan Cheiwchanchamnangij and Walter R. L. Lambrecht. Quasiparticle band structure calculation of monolayer, bilayer, and bulk mos<sub>2</sub>. *Phys. Rev. B*, 84:205302, 2012.
- [83] Ji Feng, Xiaofeng Qian, Cheng-Wei Huang, and Ju Li. Strain-engineered artificial atom as a broad-spectrum solar energy funnel. *Nature Photonics*, 6:866, March 2012.
- [84] Keliang He, Charles Poole, Kin Fai Mak, and Jie Shan. Experimental demonstration of continuous electronic structure tuning via strain in atomically thin mos<sub>2</sub>. *Nano Letters*, 13:2931, May 2013.

- [85] M. Pollak and T. H. Geballe. Low-frequency conductivity due to hopping processes in silicon. *Phys. Rev.*, 122:1742–1753, Jun 1961.
- [86] Howard K. Rockstad. Hopping conduction and optical properties of amorphous chalcogenide films. *Journal of Non-Crystalline Solids*, 2:192–202, 1970.
- [87] G. E. Pike. ac conductivity of scandium oxide and a new hopping model for conductivity. *Phys. Rev. B*, 6:1572–1580, Aug 1972.
- [88] Rolf Landauer. The electrical resistance of binary metallic mixtures. *Journal of Applied Physics*, 23(7):779–784, 1952.
- [89] J.P. Clerc, G. Giraud, J.M. Laugier, and J.M. Luck. The electrical conductivity of binary disordered systems, percolation clusters, fractals and related models. *Advances in Physics*, 39(3):191–309, 1990.
- [90] P. F. Henning, C. C. Homes, S. Maslov, G. L. Carr, D. N. Basov, B. Nikolić, and M. Strongin. Infrared studies of the onset of conductivity in ultrathin pb films. *Phys. Rev. Lett.*, 83:4880–4883, Dec 1999.
- [91] Haining Wang, Jared H. Strait, Paul A. George, Shriram Shivaraman, Virgil B. Shields, Mvs Chandrashekar, Jeonghyun Hwang, Farhan Rana, Michael G. Spencer, Carlos S. Ruiz-Vargas, and Jiwoong Park. Ultrafast relaxation dynamics of hot optical phonons in graphene. *Applied Physics Letters*, 96(8):081917, 2010.
- [92] Mark Lundstorm. *Fundamentals of Carrier Transport*. Cambridge University Press, Cambridge, UK, 2 edition, 2009.
- [93] Shengjun Yuan, Rafael Roldán, M. I. Katsnelson, and Francisco Guinea. Effect of point defects on the optical and transport properties of mos<sub>2</sub> and ws<sub>2</sub>. *Phys. Rev. B*, 90:041402, Jul 2014.
- [94] Shuxian Wang, Haohai Yu, Huaijin Zhang, Aizhu Wang, Mingwen Zhao, Yanxue Chen, Liangmo Mei, and Jiyang Wang. Broadband few-layer mos<sub>2</sub> saturable absorbers. *Advanced Materials*, 26(21):3538–3544, 2014.
- [95] Kangpeng Wang, Jun Wang, Jintai Fan, Mustafa Lotya, Arlene O'Neill, Daniel Fox, Yanyan Feng, Xiaoyan Zhang, Benxue Jiang, Quanzhong Zhao, Hongzhou Zhang, Jonathan N. Coleman, Long Zhang, and Werner Josef Blau. Ultrafast saturable absorption of two-dimensional mos<sub>2</sub> nanosheets. *ACS Nano*, 7(10):9260–9267, 2013.
- [96] Marco M. Furchi, Dmitry K. Polyushkin, Andreas Pospischil, and Thomas Mueller. Mechanisms of photoconductivity in atomically thin mos<sub>2</sub>. *arXiv:1406.5640*, June 2014.

- [97] Peter T. Landsberg. *Recombination in Semiconductors*. Cambridge University Press, Cambridge, UK, 1 edition, 1992.
- [98] B. K. Ridley. *Quantum Processes in Semiconductors*. Oxford University Press, New York, USA, 5 edition, 2013.
- [99] E. Gaubas, M. Bauža, A. Uleckas, and J. Vanhellenmont. Carrier lifetime studies in ge using microwave and infrared light techniques. *Mat. Sci. in Semicond. Proc.*, 9:781–787, 2006.
- [100] Kyungjune Cho, Tae-Young Kim, Woanseo Park, Juhun Park, Dongku Kim, Jington Jang, Hyunhak Jeong, Seunghun Hong, and Takhee Lee. Gate-bias stress-dependent photoconductive characteristics of multi-layer mos<sub>2</sub> field-effect transistors. *Nanotechnology*, 25:155201, June 2014.
- [101] Bozhi Tian, Thomas J. Kempa, and Charles M. Lieber. Single nanowire photovoltaics. *Chem. Soc. Rev.*, 38(1):16–24, 2009.
- [102] Wei Lu and Charles M. Lieber. Nanowire transistor performance limits and applications. *IEEE Trans. Electron Dev.*, 55(11):2859–2876, 2008.
- [103] Donald J. Surbuly, Matt Law, Haoquan Yan, and Peidong Yang. Semiconductor nanowires for subwavelength photonics integration. *J. Phys. Chem. B*, 109(32):15190–15213, 2005.
- [104] Y. H. Ahn and Jiwoong Park. Efficient visible light detection using individual germanium nanowire field effect transistors. *Appl. Phys. Lett.*, 91:162102, 2007.
- [105] Matt Law, Joshua Goldberger, and Peidong Yang. Semiconductor nanowires and nanotubes. *Annu. Rev. Mater. Res.*, 34:83–122, 2004.
- [106] R. Agarwal and C.M. Lieber. Semiconductor nanowires: Optics and optoelectronics. *Appl. Phys. A*, 85:209–215, 2006.
- [107] R. P. Prasankumar, S. Choi, S. A. Trugman, S. T. Picraux, and A. J. Taylor. Ultrafast electron and hole dynamics in germanium nanowires. *Nano Lett.*, 8(6):1619–1624, 2008.
- [108] Chi-Kuang Sun, Shih-Ze Sun, Kung-Hsuan Lin, Kenneth Yi-Jie Zhang, Hsiang-Lin Liu, Sai-Chang Liu, and Jih-Jen Wu. Ultrafast carrier dynamics in zno nanorods. *Appl. Phys. Lett.*, 87:023106, 2005.
- [109] Paul A. George, Jared H. Strait, Jahan Dawlaty, Shriram Shivaraman, Mvs Chandrashekhara, Farhan Rana, and Michael G. Spencer. Ultrafast optical-pump terahertz-probe spectroscopy of the carrier relaxation and recombination dynamics in epitaxial graphene. *Nano Lett.*, 8:4248–4251, 2008.

- [110] Jared H. Strait, Paul A. George, Mark Levendorf, Martin Blood-Forsythe, Farhan Rana, and Jiwoong Park. Measurements of the carrier dynamics and terahertz response of oriented germanium nanowires using optical-pump terahertz-probe spectroscopy. *Nano Letters*, 9(8):2967–2972, 2009.
- [111] Yi Cui, Lincoln J. Lauhon, Mark S. Gudiksen, Jianfang Wang, and Charles M. Lieber. Diameter-controlled synthesis of single-crystal silicon nanowires. *Appl. Phys. Lett.*, 78(15):2214–2216, 2001.
- [112] Hemanth Jagannathan, Michael Deal, Yoshio Nishi, Jacob Woodruff, Christopher Chidsey, and Paul C. McIntyre. Nature of germanium nanowire heteroepitaxy on silicon substrates. *Journal of Applied Physics*, 100(2):024318, 2006.
- [113] Zhiyong Fan, Johnny C. Ho, Zachery A. Jacobson, Roie Yerushalmi, Robert L. Alley, Haleh Razavi, and Ali Javey. Wafer-scale assembly of highly ordered semiconductor nanowire arrays by contact printing. *Nano. Lett.*, 8(1):20–25, 2008.
- [114] Q. Wu, M. Litz, and X.-C. Zhang. Broadband detection capability of znTe electro-optic field detectors. *Appl. Phys. Lett.*, 68(21):2924–2926, 1996.
- [115] D. W. Bailey and C. J. Stanton. Calculations of femtosecond differential optical transmission in germanium. *J. Appl. Phys.*, 77(5):2107–2115, 1994.
- [116] Koichiro Tanaka, Hideyuki Ohtake, Hiroyuki Nansei, and Tohru Suemoto. Subpicosecond hot-hole relaxation in germanium studied by time-resolved inter-valence-band raman scattering. *Phys. Rev. B*, 52(15):10709–10712, Oct 1995.
- [117] A. Urbanowicz, R. Adomavičius, and A. Krotkus. Terahertz emission from photoexcited surfaces of Ge crystals. *Physica B*, 367:152–157, 2005.
- [118] François Léonard, A. Alec Talin, B. S. Swartzentruber, and S. T. Picraux. Diameter-dependent electronic transport properties of Au-catalyst/Ge-nanowire Schottky diodes. *Physical Review Letters*, 102(10):106805, 2009.
- [119] Richard S. Muller and Theodore I. Kamins. *Device Electronics for Integrated Circuits*. John Wiley & Sons, third edition, 2003.
- [120] Brian A. Bryce, Mark C. Reuter, Brent A. Wacaser, and Sandip Tiwari. Contactless measurement of surface dominated recombination in gold- and aluminum-catalyzed silicon vapor–liquid–solid wires. *Nano Letters*, 11(10):4282–4287, 2011.
- [121] A. K. Geim and K. S. Novoselov. The rise of graphene. *Nature Materials*, 6:183–191, 2007.

- [122] D. S. L. Abergel, V. Apalkov, J. Berashevich, K. Ziegler, and Tapash Chakraborty. Properties of graphene: a theoretical perspective. *Advances in Physics*, 59:261–482, 2010.
- [123] F. Bonaccorso, Z. Sun, T. Hasan, and A. C. Ferrari. Graphene photonics and optoelectronics. *Nature Photonics*, 4:611–622, 2010.
- [124] Qiaoliang Bao, Han Zhang, Yu Wang, Zhenhua Ni, Yongli Yan, Ze Xiang Shen, Kian Ping Loh, and Ding Yuan Tang. Atomic-layer graphene as a saturable absorber for ultrafast pulsed lasers. *Advanced Functional Materials*, 19(19):3077–3083, 2009.
- [125] Fengnian Xia, Thomas Mueller, Yu ming Lin, Alberto Valdes-Garcia, and Phaedon Avouris. Ultrafast graphene photodetector. *Nature Nanotech.*, 4:839–843, 2009.
- [126] F. Rana. Graphene terahertz plasmon oscillators. *Nanotechnology, IEEE Transactions on*, 7(1):91–99, jan 2008.
- [127] Justin C. W. Song, Mark S. Rudner, Charles M. Marcus, and Leonid S. Levitov. Hot carrier transport and photocurrent response in graphene. *Nano Letters*, 11(11):4688–4692, 2011.
- [128] I. Meric, M. Y. Han, A. F. Young, B. Ozyilmaz, Kim P., and K. L. Shepard. Current saturation in zero-bandgap, top-gated graphene field-effect transistors. *Nature Nanotechnology*, 3:654, 2008.
- [129] Chun Hung Lui, Kin Fai Mak, Jie Shan, and Tony F. Heinz. Ultrafast photoluminescence from graphene. *Phys. Rev. Lett.*, 105(12):127404, Sep 2010.
- [130] Jahan M. Dawlaty, Shriram Shivaraman, Mvs Chandrashekhar, Farhan Rana, and Michael G. Spencer. Measurement of ultrafast carrier dynamics in epitaxial graphene. *Applied Physics Letters*, 92(4):042116, 2008.
- [131] Haining Wang, Jared H. Strait, Paul A. George, Shriram Shivaraman, Virgil B. Shields, Mvs Chandrashekhar, Jeonghyun Hwang, Farhan Rana, Michael G. Spencer, Carlos S. Ruiz-Vargas, and Jiwoong Park. Ultrafast relaxation dynamics of hot optical phonons in graphene. *Applied Physics Letters*, 96(8):081917, 2010.
- [132] Dong Sun, Zong-Kwei Wu, Charles Divin, Xuebin Li, Claire Berger, Walt A. de Heer, Phillip N. First, and Theodore B. Norris. Ultrafast relaxation of excited dirac fermions in epitaxial graphene using optical differential transmission spectroscopy. *Phys. Rev. Lett.*, 101(15):157402, Oct 2008.
- [133] Libai Huang, Gregory V. Hartland, Li-Qiang Chu, Luxmi, Randall M. Feenstra, Chuanxin Lian, Kristof Tahy, and Huili Xing. Ultrafast transient absorption

- microscopy studies of carrier dynamics in epitaxial graphene. *Nano Letters*, 10(4):1308–1313, 2010.
- [134] Ryan W. Newson, Jesse Dean, Ben Schmidt, and Henry M. van Driel. Ultrafast carrier kinetics in exfoliated graphene and thin graphite films. *Opt. Express*, 17(4):2326–2333, Feb 2009.
- [135] Leandro M Malard, Kin Fai Mak, A H Castro Neto, N M R Peres, and Tony F Heinz. Observation of intra- and inter-band transitions in the transient optical response of graphene. *New Journal of Physics*, 15(1):015009, 2013.
- [136] Kwangu Kang, Daner Abdula, David G. Cahill, and Moonsub Shim. Lifetimes of optical phonons in graphene and graphite by time-resolved incoherent anti-stokes raman scattering. *Phys. Rev. B*, 81(16):165405, Apr 2010.
- [137] Wang-Kong Tse and S. Das Sarma. Energy relaxation of hot dirac fermions in graphene. *Phys. Rev. B*, 79(23):235406, Jun 2009.
- [138] R. Bistritzer and A. H. MacDonald. Electronic cooling in graphene. *Phys. Rev. Lett.*, 102(20):206410, May 2009.
- [139] H. Choi, F. Borondics, D. A. Siegel, S. Y. Zhou, M. C. Martin, A. Lanzara, and R. A. Kaindl. Broadband electromagnetic response and ultrafast dynamics of few-layer epitaxial graphene. *Applied Physics Letters*, 94(17):172102, 2009.
- [140] Farhan Rana. Electron-hole generation and recombination rates for coulomb scattering in graphene. *Phys. Rev. B*, 76(15):155431, Oct 2007.
- [141] Torben Winzer, Andreas Knorr, and Ermin Malic. Carrier multiplication in graphene. *Nano Lett.*, 10(12):4839–4843, 2010.
- [142] Farhan Rana, Paul A. George, Jared H. Strait, Jahan Dawlaty, Shriram Shivaraman, Mvs Chandrashekhar, and Michael G. Spencer. Carrier recombination and generation rates for intravalley and intervalley phonon scattering in graphene. *Phys. Rev. B*, 79(11):115447, Mar 2009.
- [143] Farhan Rana, Jared H. Strait, Haining Wang, and Christina Manolatu. Ultrafast carrier recombination and generation rates for plasmon emission and absorption in graphene. *Physical Review B*, 84(4):045437, 2011.
- [144] Jared H. Strait, Haining Wang, Shriram Shivaraman, Virgil Shields, Michael Spencer, and Farhan Rana. Very slow cooling dynamics of photoexcited carriers in graphene observed by optical-pump terahertz-probe spectroscopy. *Nano Letters*, 11(11):4902–4906, 2011.
- [145] Claire Berger, Zhimin Song, Xuebin Li, Xiaosong Wu, Nate Brown, Ccile Naud, Didier Mayou, Tianbo Li, Joanna Hass, Alexei N. Marchenkov, Edward H.

- Conrad, Phillip N. First, and Walt A. de Heer. Electronic confinement and coherence in patterned epitaxial graphene. *Science*, 312(5777):1191–1196, 2006.
- [146] Jahan M. Dawlaty, Shriram Shivaraman, Jared Strait, Paul George, Mvs Chandrashekar, Farhan Rana, Michael G. Spencer, Dmitry Veksler, and Yunqing Chen. Measurement of the optical absorption spectra of epitaxial graphene from terahertz to visible. *Applied Physics Letters*, 93(13):131905, 2008.
- [147] Markus Breusing, Claus Ropers, and Thomas Elsaesser. Ultrafast carrier dynamics in graphite. *Phys. Rev. Lett.*, 102(8):086809, Feb 2009.
- [148] Hidekatsu Suzuura and Tsuneya Ando. Phonons and electron-phonon scattering in carbon nanotubes. *Physical Review B*, 65:235412, 2002.
- [149] Ioannis Chatzakis, Hugen Yan, Daohua Song, Stephane Berciaud, and Tony F. Heinz. Temperature dependence of the anharmonic decay of optical phonons in carbon nanotubes and graphite. *Physical review B*, 83(20):205411, May 2011.
- [150] Stefano Piscanec, Michele Lazzeri, J. Robertson, Andrea C. Ferrari, and Francesco Mauri. Optical phonons in carbon nanotubes: Kohn anomalies, peierls distortions, and dynamic effects. *Phys. Rev. B*, 75(3):035427, Jan 2007.
- [151] Dimitri K. Efetov and Philip Kim. Controlling electron-phonon interactions in graphene at ultrahigh carrier densities. *Physical Review Letters*, 105:256805, 2010.
- [152] H. L. Stormer, L. N. Pfeiffer, K. W. Baldwin, and K. W. West. Observation of a bloch-grüneisen regime in two-dimensional electron transport. *Phys. Rev. B*, 41:1278–1281, Jan 1990.
- [153] Nathaniel M. Gabor, Justin C. W. Song, Qiong Ma, Nityan L. Nair, Thiti Taychatanapat, Kenji Watanabe, Takashi Taniguchi, Leonid S. Levitov, and Pablo Jarillo-Herrero. Hot carrier-assisted intrinsic photoresponse in graphene. *Science*, 334(6056):648–652, 2011.
- [154] Justin C. W. Song, Michael Y. Reizer, and Leonid S. Levitov. Disorder-assisted electron-phonon scattering and cooling pathways in graphene. *Phys. Rev. Lett.*, 109:106602, Sep 2012.
- [155] A. C. Betz, S. H. Jhang, E. Pallecchi, R. Ferreira, G. Fève, J-M. Berrier, and B. Placais. Supercollision cooling in undoped graphene. *Nature Physics*, 9:109–112, 2013.
- [156] Matt W. Graham, Su-Fei Shi, Daniel C. Ralph, Jiwoong Park, and Paul L. McEuen. Photocurrent measurements of supercollision cooling in graphene. *Nature Physics*, 9:103, 2013.

- [157] J M Pitarke, V M Silkin, E V Chulkov, and P M Echenique. Theory of surface plasmons and surface-plasmon polaritons. *Reports on Progress in Physics*, 70(1):1–87, 2007.
- [158] Han-Kwang Nienhuys and Villy Sundstrom. Influence of plasmons on terahertz conductivity measurements. *Applied Physics Letters*, 87(1):012101, 2005.
- [159] O. Madelung, editor. *Semiconductors: Group IV Elements and III-V Compounds*. Data in Science and Technology. Springer-Verlag, 1991.
- [160] C. M. Randall and R. D. Rawcliffe. Refractive indices of germanium, silicon, and fused quartz in the far infrared. *Appl. Opt.*, 6(11):1889–1895, 1967.
- [161] L. Ju, B. Geng, J. Horng, C. Girit, M. Martin, Z. Hao, H. A. Bechtel, A. Zettl, Y. R. Shen, and F. Wang. Graphene plasmonics for tunable terahertz metamaterials. *Nature Nanotechnology*, 6:630–634, 2011.
- [162] H. Yan, X. Li, B. Chandra, G. Tulevski, Y. Wu, M. Freitag, W. Zhu, P. Avouris, and F. Xia. Tunable infrared plasmonic devices using graphene/insulator stacks. *Nature Nanotechnology*, 7:330–334, 2012.
- [163] F. Rana. Graphene terahertz plasmon oscillators. *IEEE Trans. Nano.*, 7(1):91–99, Jan 2008.
- [164] E. H. Hwang and S. Das Sarma. Dielectric function, screening, and plasmons in two-dimensional graphene. *Phys. Rev. B*, 75:205418, May 2007.
- [165] Y. Liu, R. F. Willis, K. V. Emtsev, and Th. Seyller. Plasmon dispersion and damping in electrically isolated two-dimensional charge sheets. *Phys. Rev. B*, 78:201403(R), 2008.
- [166] Thomas N. Theis. Plasmons in inversion layers. *Surface Science*, 98(13):515 – 532, 1980.
- [167] T. Demel, D. Heitmann, P. Grambow, and K. Ploog. Far-infrared response of one-dimensional electronic systems in single- and two-layered quantum wires. *Phys. Rev. B*, 38:12732–12735, Dec 1988.
- [168] S. A. Mikhailov and N. A. Savostianova. Microwave response of a two-dimensional electron stripe. *Phys. Rev. B*, 71:035320, Jan 2005.
- [169] N M R Peres, Aires Ferreira, Yu V Bludov, and M I Vasilevskiy. Light scattering by a medium with a spatially modulated optical conductivity: the case of graphene. *Journal of Physics: Condensed Matter*, 24(24):245303, 2012.
- [170] N M R Peres, Yu V Bludov, Aires Ferreira, and M I Vasilevskiy. Exact solution for square-wave grating covered with graphene: surface plasmon-polaritons in the terahertz range. *Journal of Physics: Condensed Matter*, 25(12):125303, 2013.

- [171] Aires Ferreira and N. M. R. Peres. Complete light absorption in graphene-metamaterial corrugated structures. *Phys. Rev. B*, 86:205401, Nov 2012.
- [172] Arya Fallahi and Julien Perruisseau-Carrier. Design of tunable biperiodic graphene metasurfaces. *Phys. Rev. B*, 86:195408, Nov 2012.
- [173] Sukosin Thongrattanasiri, Frank H. L. Koppens, and F. Javier Garc'ia de Abajo. Complete optical absorption in periodically patterned graphene. *Phys. Rev. Lett.*, 108:047401, Jan 2012.
- [174] George H. Hanson. Dyadic green's functions and guided surface waves for a surface conductivity model of graphene. *J. App. Phys.*, 103:064302, 2008.
- [175] Jared H. Strait, Parinita Nene, Wei-Min Chan, Christina Manolatou, Sandip Tiwari, Farhan Rana, Joshua W. Kevek, and Paul L. McEuen. Confined plasmons in graphene microstructures: Experiments and theory. *Phys. Rev. B*, 87:241410, Jun 2013.
- [176] Xuesong Li, Weiwei Cai, Jinho An, Seyoung Kim, Junghyo Nah, Dongxing Yang, Richard Piner, Aruna Velamakanni, Inhwa Jung, Emanuel Tutuc, Sanjay K. Banerjee, Luigi Colombo, and Rodney S. Ruoff. Large-area synthesis of high-quality and uniform graphene films on copper foils. *Science*, 324(5932):1312–1314, 2009.
- [177] Amal Kasry, Marcelo A. Kuroda, Glenn J. Martyna, George S. Tulevski, and Ageeth A. Bol. Chemical doping of large-area stacked graphene films for use as transparent, conducting electrodes. *ACS Nano*, 4(7):3839–3844, 2010.
- [178] A. Das, S. Pisana, B. Chakraborty, S. Piscanec, S. K. Saha, U. V. Waghmare, K. S. Novoselov, H. R. Krishnamurthy, A. K. Geim, A. C. Ferrari, and A. K. Sood. Monitoring dopants by raman scattering in an electrochemically top-gated graphene transistor. *Nature Nanotechnology*, 3:210–215, 2008.
- [179] Hugen Yan, Tony Low, Wenjuan Zhu, Yanqing Wu, Marcus Freitag, Xuesong Li, Francisco Guinea, Phaeton Avouris, and Fengnian Xia. Damping pathways of mid-infrared plasmons in graphene nanostructures. *Nature Photonics*, 7:394–399, 2012.
- [180] Parinita Nene, Jared H. Strait, Wei-Min Chan, Christina Manolatou, Sandip Tiwari, Paul L. McEuen, and Farhan Rana. Coupling of plasmon modes in graphene microstructures. *Applied Physics Letters*, 105(14):143108, 2014.
- [181] Allen Taflove and Susan C. Hagness. *Computational Electrodynamics: The Finite-Difference Time-Domain Method*. Artech House, third edition, 2005.
- [182] J. L. Tomaino, A. D. Jameson, J. W. Kevek, M. J. Paul, A. M. van der Zande, R. A. Barton, P. L. McEuen, E. D. Minot, and Yun-Shik Lee. Terahertz imaging

- and spectroscopy of large-area single-layer graphene. *Opt. Express*, 19(1):141–146, Jan 2011.
- [183] C. R. Dean, A. F. Young, I. Meric, C. Lee, L. Wang, S. Sorgenfrei, K. Wantanabe, T. Taniguchi, P. Kim, K. L. Shepard, and J. Hone. Boron nitride substrates for high-quality graphene electronics. *Nature Nanotechnology*, 5:722–726, 2010.
- [184] W. J. Choyke, H. Matunami, and G. Pensl. *Silicon carbide: recent major advances*. Springer, New York, 1 edition, 2004.
- [185] R. Yakimova. Developments in the growth of wide bandgap semiconductors. *Physica Scripta*, T126:121, 2006.
- [186] P.-C. Lv, X. Zhang, J. Kolodzey, and A. Powell. Compact electrically pumped nitrogen-doped 4h-sic terahertz emitters operating up to 150 k. *Applied Physics Letters*, 87(24):241114, 2005.
- [187] J H Zhao, V Gruzinskis, Y Luo, M Weiner, M Pan, P Shiktorov, and E Starikov. Monte carlo simulation of 4h-sic impatt diodes. *Semiconductor Science and Technology*, 15(11):1093, 2000.
- [188] V. M. Polyakov and F. Schwierz. Formation of two-dimensional electron gases in polytypic sic heterostructures. *Journal of Applied Physics*, 98(2):023709, 2005.
- [189] P. M. Lundquist, W. P. Lin, G. K. Wong, M. Razeghi, and J. B. Ketterson. Second harmonic generation in hexagonal silicon carbide. *Applied Physics Letters*, 66(15):1883–1885, 1995.
- [190] G. Logan DesAutels, Chris Brewer, Mark Walker, Shane Juhl, Marc Finet, Scott Ristich, Matt Whitaker, and Peter Powers. Femtosecond laser damage threshold and nonlinear characterization in bulk transparent sic materials. *J. Opt. Soc. Am. B*, 25(1):60–66, Jan 2008.
- [191] S. Niedermeier, H. Schillinger, R. Sauerbrey, B. Adolph, and F. Bechstedt. Second-harmonic generation in silicon carbide polytypes. *Applied Physics Letters*, 75(5):618–620, 1999.
- [192] H. P. Wagner, M. Kühnelt, W. Langbein, and J. M. Hvam. Dispersion of the second-order nonlinear susceptibility in zn<sub>te</sub>, zn<sub>se</sub>, and zn<sub>s</sub>. *Phys. Rev. B*, 58:10494–10501, Oct 1998.
- [193] Jared H. Strait, Paul A. George, Jahan Dawlaty, Shriram Shivaraman, Mvs Chandrashekar, Farhan Rana, and Michael G. Spencer. Emission of terahertz radiation from sic. *Applied Physics Letters*, 95(5):051912, 2009.
- [194] Q. Chen, M. Tani, Zhiping Jiang, and X.-C. Zhang. Electro-optic transceivers for terahertz-wave applications. *J. Opt. Soc. Am. B*, 18(6):823–831, Jun 2001.

- [195] I. J. Wu and G. Y. Guo. Second-harmonic generation and linear electro-optical coefficients of sic polytypes and nanotubes. *Phys. Rev. B*, 78:035447, Jul 2008.
- [196] B. Adolph and F. Bechstedt. Influence of crystal structure and quasiparticle effects on second-harmonic generation: Silicon carbide polytypes. *Phys. Rev. B*, 62:1706–1712, Jul 2000.
- [197] Sergey N. Rashkeev, Walter R. L. Lambrecht, and Benjamin Segall. Second-harmonic generation in sic polytypes. *Phys. Rev. B*, 57:9705–9715, Apr 1998.
- [198] Jian Chen, Zachary H. Levine, and John W. Wilkins. Linear and nonlinear optical properties of four polytypes of sic. *Phys. Rev. B*, 50:11514–11519, Oct 1994.
- [199] P. T. B. Shaffer. Refractive index, dispersion, and birefringence of silicon carbide polytypes. *Appl. Opt.*, 10(5):1034–1036, May 1971.
- [200] Ajay Nahata, Aniruddha S. Weling, and Tony F. Heinz. A wideband coherent terahertz spectroscopy system using optical rectification and electro-optic sampling. *Applied Physics Letters*, 69(16):2321–2323, 1996.
- [201] János Hebling, Ka-Lo Yeh, Matthias C. Hoffmann, Balázs Bartal, and Keith A. Nelson. Generation of high-power terahertz pulses by tilted-pulse-front excitation and their application possibilities. *J. Opt. Soc. Am. B*, 25(7):B6–B19, Jul 2008.
- [202] P.-C. Lv, X. Zhang, J. Kolodzey, and A. Powell. Characteristics of terahertz-wave generation from gas crystals. *J. Phys. D: Appl. Phys.*, 37:155, 2004.
- [203] C. Weiss, G. Torosyan, Y. Avetisyan, and R. Beigang. Generation of tunable narrow-band surface-emitted terahertz radiation in periodically poled lithium niobate. *Opt. Lett.*, 26(8):563–565, Apr 2001.
- [204] János Hebling, Matthias C. Hoffmann, Harold Y. Hwang, Ka-Lo Yeh, and Keith A. Nelson. Observation of nonequilibrium carrier distribution in ge, si, and gaas by terahertz pump-terahertz probe measurements. *Phys. Rev. B*, 81:035201, Jan 2010.
- [205] Sharly Fleischer, Yan Zhou, Robert W. Field, and Keith A. Nelson. Molecular orientation and alignment by intense single-cycle thz pulses. *Phys. Rev. Lett.*, 107:163603, Oct 2011.
- [206] Harold Y. Hwang, Nathaniel C. Brandt, Hootan Farhat, Allen L. Hsu, Jing Kong, and Keith A. Nelson. Nonlinear thz conductivity dynamics in p-type cvd-grown graphene. *The Journal of Physical Chemistry B*, 117(49):15819–15824, 2013.